A Contact Force Sensor for Medical Jet Injection

by

Nickolas Peter Demas

B.S. Mechanical Engineering, Yale University (2013)

Submitted to the Department of Mechanical Engineering
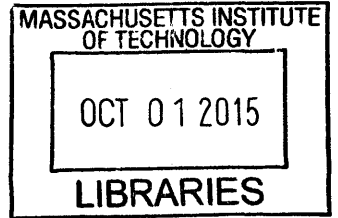in partial fulfillment of the requirements for the degree of

Master of Science in Mechanical Engineering

at the

MASSACHUSETTS INSTITUTE OF TECHNOLOGY

September 2015

Signature redacted

Author . . . .
Department of Mechanical Engineering
August 8, 2015

Signature redacted

Certified by. . . . .
Ian W. Hunter
Hatsopoulos Professor of Mechanical Engineering
Thesis Supervisor

Signature redacted

Accepted by . . . .
David E. Hardt
Chairman, Department Committee on Graduate Theses

A Contact Force Sensor for Medical Jet Injection

by

Nickolas Peter Demas

Submitted to the Department of Mechanical Engineering
on August 8, 2015, in partial fulfillment of the
requirements for the degree of
Master of Science in Mechanical Engineering

Abstract

Medical jet injection, in which a narrow fluid drug stream is propelled into the skin without a needle, was first conceived in the 1940s [1]. However, a major drawback of most injectors is the lack of controllability of jet parameters. Recent work at the BioInstrumentation Laboratory at MIT has resulted in a tunable, high-performance linear Lorentz-force jet injector which allows for careful control of many injection variables. The sensor presented in this thesis further improves the ability to quantify and control contact forces between the injection nozzle and tissue. This sensor uses a three-spoke flexure system with full-bridge strain gauge assemblies mounted on each flexural arm to measure both normal and lateral forces applied to the nozzle. The design, fabrication, calibration, and validation for the sensor are detailed along with results for preliminary tissue injections into *ex vivo* porcine tissue. These preliminary tests showed higher percent volume delivery to the tissue with an elevated normal force. Under normal forces of 4 to 8 N, the BioInstrumentation Lab's jet injector achieved percent volume delivery of 89.1 ± 5.1%, whereas with normal forces of 0 to 4 N, the percent volume delivery was 68.9 ± 12.7%.

Thesis Supervisor: Ian W. Hunter
Title: Hatsopoulos Professor of Mechanical Engineering

Acknowledgments

I would like to thank Professor Ian Hunter for the opportunity to work in his group. The resources available at the BioInstrumentation Laboratory have been absolutely outstanding. His encouragement and guidance have helped me mature as an engineer and I am sincerely grateful to be a member of the lab.

My colleagues and good friends in the BioInstrumentation Laboratory have been incredibly helpful in my pursuits at MIT. Dr. Brian Hemond and Mike Nawrot, co-inventors on the provisional patent filed for the force sensor developed in this thesis, both acted as great sounding boards for my ideas and helped many times with debugging and troubleshooting. Dr. Yi (Ellen) Chen, Dr. Jean Chang, and Dr. Eli Paster were always willing to take a pause in their own work to to discuss my research questions, for which I am extremely appreciative. Thanks to the current lab gang including Dr. Cathy Hogan, Ashley Brown, Craig Cheney, John Liu, Kate Melvin, Seyed Mirvakili, Ashin Modak, Geehoon Park, and Anshul Singhal who make work in the lab fun, fast-paced, and intellectually stimulating and are always willing to lend a helping hand or offer advice. A special thanks to Ian, Cathy, John, and Ashin for reviewing and providing feedback on this thesis.

I am grateful to my parents and brother for their never-ending encouragement and love. I do not know the words to express how lucky I am to have Dad, Mom and Christopher. I would also like to thank all of the members of my extended family. I am so fortunate to have their love and support as well. I love you all.

I would like to thank Jerry Wang, my roommate, co-conspirator, and best friend. Thanks to him, the time during our master's degrees has been filled with great memories, gut-hurting laughter, a pinch of ridiculousness (actually, make that eleven fully filled canisters), and a very needed dose of sanity every now and again. I am so lucky to have a best bud like him.

I finally would like to thank my girlfriend, Nozomi Nakajima. Her encouragement, kindness, and love help me to excel and I am eternally grateful to her for getting me through the tough times and putting up with my nonsense. I love you, Mimi.

Contents

List of Figures

11

List of Tables

Chapter 1

Introduction

"I have injected Wine and Ale in a living Dog into the Mass of Blood by a Veine, in good Quantities, till I have made him extremely drunk"

– Sir Christopher Wren, early pioneer of intravenous injection, in an undated letter to associate William Petty describing one of his first injections, 1656-8 [2]

1.1   Brief History of Medical Injection

Medical injection is a particularly attractive administration route for many treatments given some unique benefits. Injection offers a viable method of drug administration for drugs that are poorly absorbed or ineffective when given by other methods [3]. Additionally, both rapid and delayed responses can be achieved with injections to particular tissue structures [4].

Hypodermic needles are the oldest method for injecting substances into living creatures. One of the earliest injections on record was by a British scientist, mathematician, and architect by the name of Sir Christopher Wren [5]. With a needle, Wren set out to introduce liquid poison into an animal's bloodstream by mimicking the bite of a viper. Around 1655, in the presence of various physicians and virtuosi, Wren performed an intravenous injection of warm opium and white wine with a narrow pipe into the rump of a canine. Once released, the dog immediately began to

stagger around. With a comical disregard for the scientific and medical magnitude of the accomplishment, those in attendance began to offer bets as to whether the animal would perish. However, Robert Boyle (the dog's owner and colleague of Wren) was anxious to keep his dog for further observation and had him whipped around the lawn until he came out of his drunken stupor [2].

From its use by Wren in the 1600s, hypodermic injection by needle has unarguably advanced significantly and represents the current standard of care for nearly all injected medicines. It is not, however, without deficits. From the patient's perspective, pain is a common complaint [4]. Additionally, over 20% of individuals suffer from some degree of hypodermic needle fear [6]. Pain and the associated fear of needles can cause noncompliance with prescribed treatment or avoidance of medical care altogether [6]. When administering treatment via needle, caregivers also are exposed to risk of injury or infection from a needlestick (or a break in the skin caused by a needle). In the U.S. annually, estimates put the risk of needlestick at approximately one in seven healthcare workers [7]. This can lead to the transmission of HIV, hepatitis C and B, TB, syphilis, malaria, herpes, diphtheria, gonorrhea, typhus, and Rocky Mountain spotted fever [7].

1.2 Medical Jet Injection

Jet injection is the process by which a very narrow, high-velocity stream of fluid penetrates tissue without a hypodermic needle. The first patent to apply this principle to the injection of medicine was filed in 1943 [1] and since the inception of this injection paradigm, the varieties of commercially available jet injectors (JIs) have grown substantially. While mass-campaign JIs with multi-use nozzles were deployed successfully to eradicate diseases such as smallpox in the 1970s [8], cross-contamination issues [9] prevented widespread adoption and caused multi-use nozzle JIs to fall out of favor [10]. JIs with single-use nozzles do not suffer from cross-contamination issues and have emerged as viable methods for delivering insulin, anesthetics, and other transdermal treatments [11, 12, 13, 14, 15, 16]. A selection of these JIs are shown in

Figure 1-1, sorted by energy source.

Single-use nozzle JIs offer benefits over traditional hypodermics. As compared to needle injection, pain sensation with jet injection is likely be reduced due to the small liquid jet diameter [17]. Additionally, many of the issues associated with needle fear and needlestick injuries are eliminated with jet injection. But for JIs to compete with traditional needles, injection precision and accuracy with delivered depth and volume is critical. Treatments prescribed in a specific dose for a particular tissue layer must be administered properly. In needle injection, the delivery depth is determined by the depth to which the needle is inserted (d in Figure 1-2) and the delivery volume is determined by the volume of liquid drug dispensed by the syringe (V in Figure 1-2). However, the mechanism by which a liquid jet penetrates tissue is much more complicated and is highly dependent on the velocity of the fluid stream [18] .

The commercially available JIs shown in Figure 1-1 are powered by a range of energy sources including springs, compressed gasses, and explosive chemicals. The majority of these injectors have little control in the release of their stored energy. As such, particular velocity profiles are difficult to set before injection, achieve during injection, and confirm post injection even if the desired parameters are known for a specific fluid and injection site. While there has been development in academic research settings of piezoelectric stack actuated JIs, which have the capabilities to control for specific parameters of the injection, they are limited in the total volume that can be delivered; Piezoelectric stack actuated JIs have reported injection volumes of less than $10\,\mu L$ [20] whereas a single treatment of insulin can be as large as $1\,mL$ [21].

1.3   Lorentz-Force Actuated Jet Injector

The BioInstrumentation Lab has developed a novel jet injector which overcomes the limitations of available JIs to control the velocity of the fluid jet using a linear Lorentz-force actuator [22, 18, 23]. Linear Lorentz-force actuators (also known as voice-coil actuators given their prevalence in loudspeaker systems) pass electric current through

Figure 1-1: Selection of JIs, sorted by energy source. Spring actuated injectors include the (from left to right) Injex [11], Zoë [12], and ZetaJet® [19]; compressed gas actuated injectors include the Dosepro® [13] and J-Tip [14]; chemical explosive actuated injectors include the Crossject® [15]; electric actuated injectors include the MIT BioInstrumentation Lab's linear Lorentz-force injector [18]. Images reproduced from [11, 12, 13, 14, 15, 18, 19].
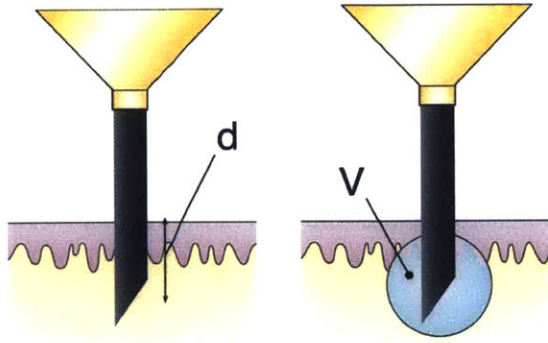
Figure 1-2: (*Left*) d represents the depth to which the needle is inserted, which determines the tissue layer to which the drug is delivered. (*Right*) V represents the volume dispensed by the syringe, which is the total volume delivered to the particular depth specified by d. Figure adapted from [8].

a conductive coil. This current interacts with a orthogonal, static magnetic field (produced by a permanent Neodymium Iron Boron magnet in the BioInstrumentation Lab's actuator) to exert a force. This force can be modulated by varying the electric current delivered to the coil. As such, a Lorentz-force actuator can attain high-bandwidth closed loop control on coil position with a long stroke of 30 mm [18]. With the BioInstrumentation Lab's injector, a particular velocity profile can be set before injection, achieved during injection, and confirmed after injection. Even more importantly, these parameters can be easily tuned for particular individuals, injection sites, or medications for personalized delivery of injected treatment.

The literature [18] reports four variables critical for drug delivery via jet injection during the breaching and filling phases of an injection. v_{jet} and t_{jet} represent the fluid stream velocity and associated duration (respectively) during the tissue breaching phase of the injection. These two "jet" variables control the depth to which the drug penetrates. Once the hole is formed, the jet speed decelerates to v_{follow} which is maintained until the total volume V is delivered during the filling phase. These two variables control the fill rate and volume (respectively) delivered to the tissue at the depth determined by v_{jet} and t_{jet}. Published work from the BioInstrumentation Lab on a linear Lorentz-force jet injector has demonstrated good control of v_{jet}, t_{jet}, v_{follow}, and V in real time [18]. v_{jet} is typically greater than v_{follow} [18] as shown in

21
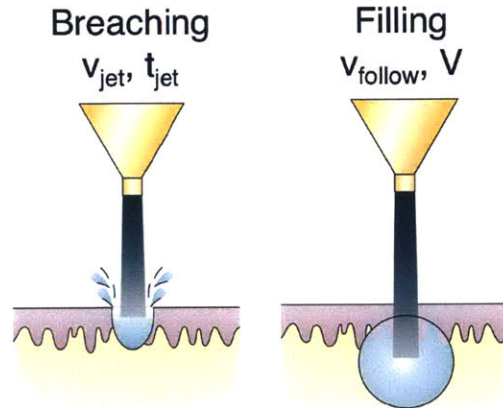
Figure 1-3: v_{jet} and t_{jet} represent the jet velocity and time (respectively) during the tissue breaching phase of the injection (shown on the *Left*) and determine depth to which the drug penetrates. Once the hole is formed, the jet speed decelerates to v_{follow} which is maintained until the total volume V is delivered during the filling phase [18] (shown on the *Right*). Figure adapted from [8].

Figure 1-4. Additionally, with the stroke of the current device and an Injex U-100 ampoule, fluid volumes up to 300 µL [18] can be delivered in a single injection, making it appropriate for a much wider range of treatments than volume-limited piezoelectric stack actuated JIs [20].

1.4   Effect of Contact Force Variation

While the parameters v_{jet}, t_{jet}, v_{follow}, and V have been well documented as key variables affecting the depth and volume delivered, an interest developed in how contact force influenced delivery. It was hypothesized that the direction and magnitude of contact force applied to the nozzle would impact the quality of the circumferential seal formed around the nozzle, affecting delivery volume. Additionally, it was hypothesized that these contact forces could also govern the penetrability of the tissue layers by changing the pretension and thickness of the tissue layers, affecting delivery depth. It was further hypothesized that the addition of a sensor to quantify and control contact forces between the nozzle and tissue would improve the precision and accuracy of the delivery so that a high percentage of the volume initially contained

22
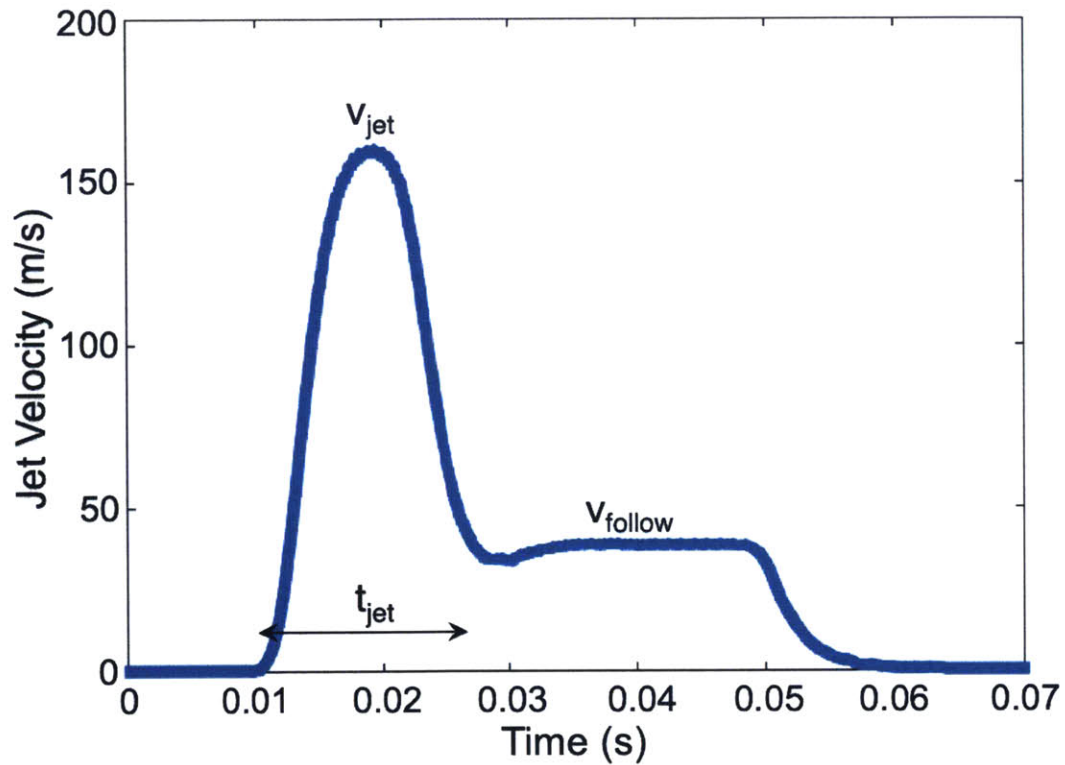
Figure 1-4: Velocity profile in time showing v_{jet} and t_{jet} during the breaching phase and v_{follow} during the filling phase. Note that the area under this curve represents the total distance the piston has traveled. The total volume V ejected is simply this area multiplied by the interior cross-sectional area of the nozzle.

in the ampoule could be delivered to the tissue at a more tightly controlled depth.

Wet injections are a common problem with JIs [24], whereby a portion of the fluid drug (mixed with, potentially, biological contaminant) remains on the skin surface after the injection. Instructions provided with commercial JIs typically instruct the user to wipe the area after injection. However, drugs are prescribed in particular doses and the prospect of a sizable and variable fraction of the prescribed dose failing to penetrate the tissue is deficient from a clinical perspective. Additionally, drugs can be extremely expensive. Prevnar 13, a drug delivered by needle injection to prevent pneumococcal bacterial infections in infants, costs upwards of \$152.01 for a single $500\,\mu L$ dose [25], making wet injection deficient from a cost perspective as well. Controlling the contact forces between the tip of the nozzle and the tissue could help improve percent volume delivery by making a repeatable circumferential seal between the nozzle and tissue allowing for the full dose to be delivered.

Furthermore from the clinical perspective, doses are prescribed for particular tissue layers typically based on the release rate desired and specific treatment being administered [26]. Therefore, reliably reaching a particular tissue layer is important for proper treatment. Controlling the contact force would also improve the delivery depth repeatability if the penetrability of the target during the breaching phase varied with contact force as well as v_{jet} and t_{jet}.

1.5 Contact Force Application Scenarios

Three orthogonal forces that could be applied to the nozzle were identified, as shown in Figure 1-5. These forces include the normal force F_{normal} and two lateral forces F_x and F_y.

The expected desirable loading condition was one where lateral forces F_x and F_y were minimized and normal force F_{normal} was applied in some ideal range as shown in (a) of Figure 1-6. It was hypothesized that a circumferential seal sufficient to prevent leaking would be made allowing for high volume delivery and/or minimal delivery depth variation could be achieved, making these loading conditions ideal. However,
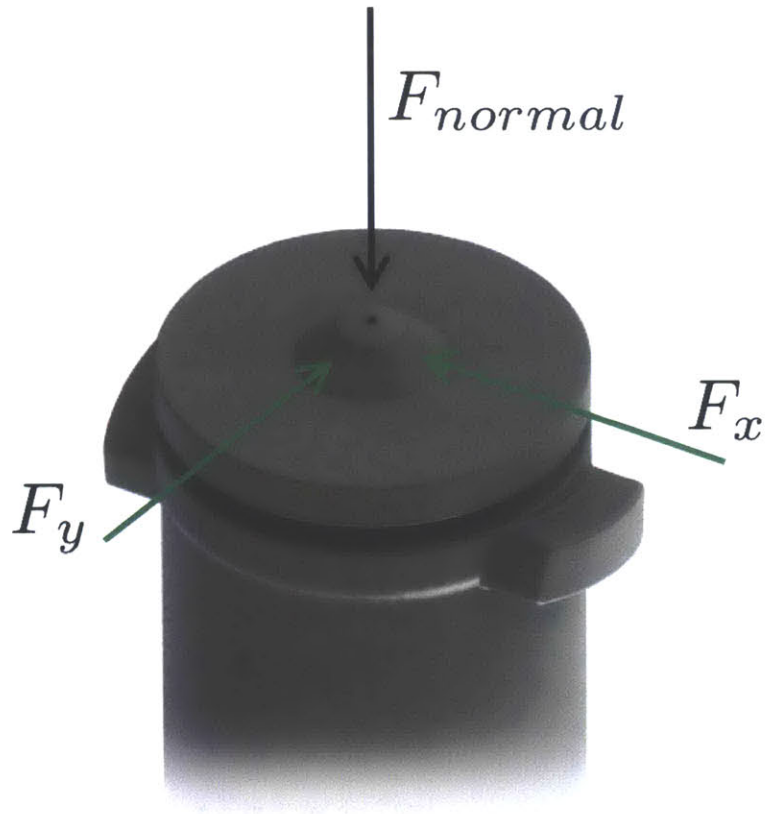
Figure 1-5: Normal force F_{normal} and two lateral forces F_x and F_y were identified as the orthogonal loads that could be exerted on the nozzle.

there existed many other loading conditions for which negative effects were hypothesized. Under load could occur when the normal force level is too low, potentially causing poor percent volume delivery and/or significant delivery depth variation, as shown in (b) of Figure 1-6. Over load could occur when the normal force level is too high, potentially causing pain for the patient, as shown in (c) of Figure 1-6. Non-zero lateral forces could also be applied to the nozzle as shown in (d) of Figure 1-6. These lateral forces could be applied in combination with normal forces as shown in (e) of Figure 1-6. However, neither of the cases (d) or (e) were desirable as it was hypothesized that lateral forces should be minimized to ensure a good quality circumferential seal between the nozzle and the tissue. Commercial devices such as the Injex [11] and J-tip [14] injectors seek to minimize lateral forces by specifying that the the injector should be held at a 90° angle to the skin when force is applied as shown in Figure 1-7.

1.6   Previous Methods of Measuring and Controlling Contact Force

Many commercially available JI devices, like those in Figure 1-7, simply rely on written instructions, using words like "firmly" [11] or "slight skin contact" [14] to indicate to the user the appropriate level of normal force [11, 14, 15, 19]. Further, commercial JI instructions also commonly request that the device be held at a 90° angle to the skin surface [11, 14] presumably to minimize lateral forces and ensure an adequate seal between the nozzle and tissue around the circumference of the nozzle as discussed in Section 1.5. One commercially available JI capable of measuring and controlling for normal force between the nozzle and tissue is the Dosepro® [27]. This JI utilizes a force sensitive mechanical trigger which fires the device when a preset normal force is achieved [13]. While the Dosepro® [27] is much more capable of quantitative control than other JIs relying on written instructions, the Dosepro® is non-adjustable and gives no indication of the lateral forces applied to the tip of

Key

$\rightarrow F_{applied}$ $M_{applied}$

$\rightarrow F_{normal}$ $\rightarrow F_{lateral}$

Tissue Structure

Epidermis
Dermis

Subcutaneous Fat

Muscle
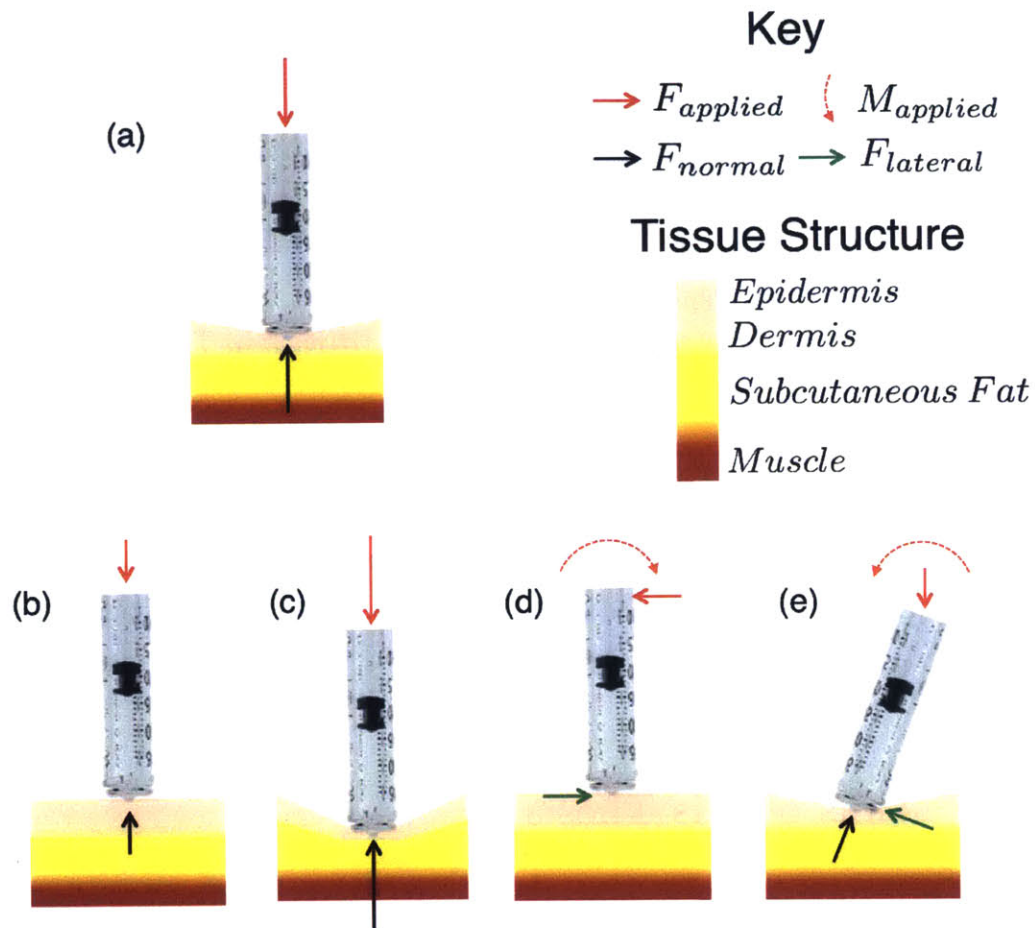
Figure 1-6: This diagram shows a variety of possible loading conditions. (a) indicates a desired loading condition where normal force is applied in a proper range and lateral forces are minimized. (b-e) indicate non-ideal loading conditions where inappropriate levels of normal or lateral force are applied to the nozzle. $F_{applied}$ (in solid red) represents an applied force on the rear of the ampoule by the user. $M_{applied}$ (in dashed red) represents an applied moment on the rear of the ampoule by the user. F_{normal} (in solid black) represents the normal force applied to the tip of the nozzle along the central axis of the ampoule. $F_{lateral}$ (in solid green) represents the lateral force (either F_x, F_y, or a combination of both) applied to the tip of the nozzle perpendicular to the central axis of the ampoule.

Figure 1-7: (*Left* [11]) The user of the Injex JI is instructed to "place the injector firmly and at a 90 degree angle on the skin" [11]. (*Right* [14]) The user of the J-Tip JI is instructed to hold the device "at a 90 degree angle to the skin, with slight skin contact" [14].

the nozzle. Critically in cases where an individual does not use a JI under direct supervision of a health care worker, the ability to measure, guide and record correct loading conditions on the nozzle would be helpful in achieving proper delivery and reducing noncompliance.

1.7   Aims of this Thesis

In this thesis, a new electronic sensor is presented for the measurement and monitoring of normal and lateral forces on the tip of the BioInstrumentation Lab's JI nozzle.

Chapter 2 presents how the device was designed to meet functional requirements identified from clinical, controls, usability, integration, and cost perspectives.

Chapter 3 discusses hardware and software found in both a bench-level prototype as well as a revised sensor version. The hardware was largely built in-house in the BioInstrumentation Lab's fabrication facilities. The software was built in LabVIEW® [28].

Chapter 4 details how the system was validated to meet all functional requirements.

Chapter 5 describes preliminary tissue injections into *ex-vivo* porcine tissue. These

tests indicated a positive correlation between normal force and percent volume delivered, which has important clinical and cost implications.

Chapter 6 explores future work.

Throughout this thesis, note that "±" indicates the standard deviation unless otherwise specified.

With this force sensor, the BioInstrumentation Lab's jet injector system was capable of guiding the user to properly apply contact force before injection.

Chapter 2

Design

"Keep it simple, stupid"

– Clarence Leonard (Kelly) Johnson, founder of Lockheed's Skunk Works [29]

2.1 Overview and FRDPARRC Table

While design is a process that requires chaotic, non-linear inspiration, it is beneficial to structure the process in a way that organizes the design approach, allowing for both creative insight and thoughtful engineering analysis to guide the journey. In this thesis, the *FRDPARRC* approach [30] is used, which encompasses *F*unctional *R*equirements, *D*esign *P*arameters, *A*nalysis, *R*esearch, *R*isk, and *C*ountermeasures, all of which are crucial components to a successful design. *F*unctional *R*equirements outline the fundamental constraints imposed by the designer, user, desired performance characteristics, the environment, and other factors. *D*esign *P*arameters are particular approaches and schemes to meet the functional requirements. *A*nalysis, including both qualitative design insight and quantitative engineering analysis, as well as *R*esearch, including literature and patent review and bench level experimentation, informs the designer on the benefits and drawbacks of particular design parameters. *R*isk identification requires that the designer contemplate all of the deficiencies of
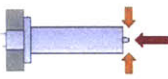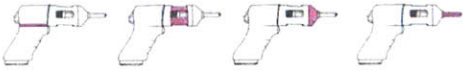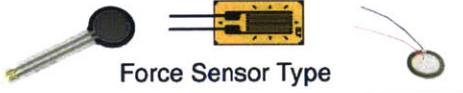
Functional Requirements	Design Parameters	Analysis	Research	Risks	Counter-measures
	Force Sensor Location			Volume Error Usability Connectivity	Analysis Small Size Flex Ribbons
	Force Sensor Type			Sensitivity Temperature Cost	Analysis Sensor Layout PCB
Performance Requirements & Constraints	Flexure Number	Gauge Configuration		Mounting Stability	Dual Gauge Technique & Materials
		Sensor Model		Idealized	Enhanced Model
		Flexure Design		2D vs. 3D	FEA Iteration

Table 2.1: Outline of critical design components organized in the *FRDPARRC* framework that are discussed in Chapter 2. Force sensing resistor, strain gauge, and piezo element images reproduced from [31, 32, 33] respectively.

the design parameters (and/or analysis, and/or research) which could impact a design's performance and *C*ountermeasures generation ensures that a plan is in place to overcome associated risks. The remainder of this chapter will discuss in detail each column of the *FRDPARRC* outline for the contact force sensor design approach shown in Table 2.1.

2.2 Functional Requirements

Obviously, the device needed to measure both normal and lateral forces on the tip of the nozzle to fully characterize the contact forces with the tissue. Beyond that, there were a number of functional requirements that were relevant to designing a successful sensor system.

First, the range and resolution needed to be specified. In terms of range, the BioInstrumentation Lab's JI could exert a maximum force of 200 N when fired [18]. It was therefore desired that the sensor would measure forces and exhibit repeatable elastic behavior under loads up to 300 N. In terms of resolution, it has been found
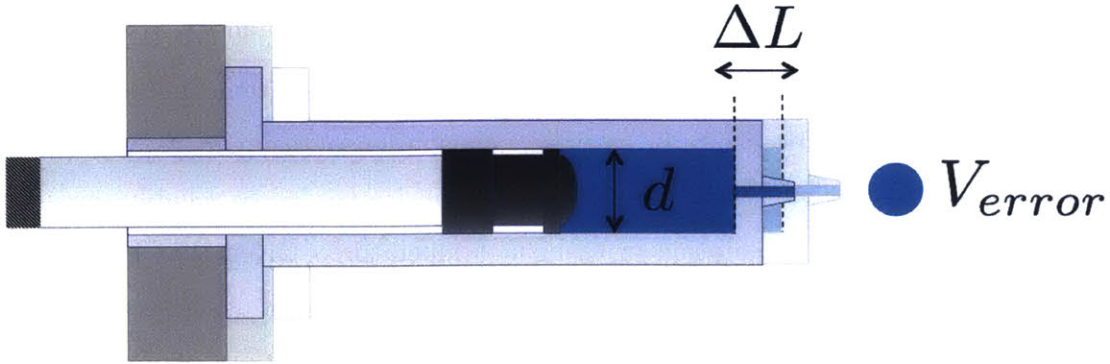
Figure 2-1: The volume error V_{error} is induced by a displacement from the force sensor. Assuming the piston is held stationary, this will result in a movement of the ampoule by length ΔL. The volume error is given by Equation 2.1 where d is the inside diameter of the ampoule. Minimizing ΔL caused by the force sensor to limit V_{error} while maintaining the desired resolution was the goal.

in the BioInstrumentation lab that an individual can sustain a force within a range of $\sim 10\,\text{N}$ at $\pm 0.5\,\text{N}$. Ideally the sensor would be able to resolve forces far below this variation.

Second, there needed to exist a maximum volume error, shown in Figure 2-1, that could be caused during the injection if the force sensor was located within the structural loop. All methods of measuring forces require displacement of an element. While this element can be made very stiff, some displacement is still required. Given results from previous ejections from the BioInstrumentation Lab's JI [18], $100\,\mu\text{L}$ ejections resulted in a standard deviation of $1.27\,\mu\text{L}$ on average. Any error due to implementing the force sensor needed to be far below that variability so as to not have a negative impact on performance. Therefore, it was determined that the sensor should induce a volume error of no more than $0.25\,\mu\text{L}$. Given the cross-sectional area of the current ampoule, the maximum allowable axial displacement was no more than $25\,\mu\text{m}$ with the ampoule inside diameter of $3.5\,\text{mm}$ and the Equation 2.1,

$$\frac{\pi d^2}{4}\Delta L = V_{error}.\tag{2.1}$$

Third, a bandwidth specification was needed. It was desired that any resonances induced or shifted by the addition of the sensor would be greater than $5\,\text{kHz}$. This

fell far above the fundamental mechanical resonance of the JI at 400 Hz [18].

Fourth, there existed a number of qualitative functional requirements that needed to be met. The sensor needed to be shielded from spurious measurements, noise, and electrical interference caused by the device. The device needed to reliably measure forces regardless of JI orientation or ambient temperature. Given that the BioInstrumentation Lab's device was pre-existing, the force sensing solution needed to be readily integrated with the device, which imposed design restrictions on size and geometry. The solution also needed to be actuator-agnostic, such that if the actuator was redesigned, the force sensor would not also require a complete redesign. Finally, it was desirable for the sensor to have a low manufacturing cost when produced in volume.

With these requirements and constraints set, it was appropriate to move to the design parameters where particular solutions would be laid out.

2.3 Design Parameters and Associated Analysis and Research

2.3.1 Sensor Location

The BioInstrumentation Lab's JI (before modifications were made to implement the force sensor) is shown on the left in Figure 2-2. The four sketches directly to the right show potential locations for the force sensor, highlighted in pink, including pre-actuator, in-actuator, post-actuator, and in-ampoule. Each location had its own benefits and drawbacks, which were explored in the Pugh chart shown in Table 2.2 and are detailed in the subsequent paragraphs.

For low induced volume error, the pre-actuator and in-ampoule locations could perform quite well given that the measurement point was outside the structural loop encompassing the actuator, housing, ampoule base, and piston. The in-actuator and post-actuator locations would induce a volume error given that the sensor was placed in the structural loop. However, this error could be limited with proper attention

paid to the design.

To achieve an appropriate flat-response bandwidth, it was expected that the fundamental oscillation frequency would decrease as the mass suspended from the sensor increased. Given the simplifying assumption that the system would behave like an undamped mechanical oscillator, $\sqrt{\frac{k}{m}} = \omega$, where k is the spring constant (in N/m), m is the mass (in kg), and ω is the resonant frequency (in rad/s). m increases when moving from right to left in Table 2.2 (from the in-ampoule to pre-actuator locations). Assuming this model is accurate for the sensor structure, increasing m decreases ω given a constant k. While theoretically k could also be increased, this would practically be difficult to implement after some point. Smaller displacements for a given load (caused by increased k) would result in poorer resolution and eventually, with a high enough k, the system would fall out of resolution specification for the chosen sensor type.

Shielding the sensor from measuring undesired loads was deemed easiest to implement in the post-actuator location since only forces applied to the ampoule would be measured. The in-actuator location would be less ideal, as measurement errors would be caused by the application of forces to the front of the actuator housing. The pre-actuator location would be very difficult to shield as the device would be prone to inaccurate measurements caused by the application of forces to any portion of the actuator housing. The in-ampoule location would also be very difficult to protect with a structural shroud while still allowing access to mount and remove the ampoule.

Building a robust and reliable device was also important. The post-actuator location appeared to be most ideal as the ampoule could be detached, removing the possibility for overload, and the sensitive force sensing elements could be shrouded in a protective structure, which would protect the sensor from a jostle or drop. The remaining locations would all be deficient. The pre-actuator and in-actuator would be continually exposed to external forces which would make them potentially prone to an overload condition. The in-ampoule location could easily sustain damage when the user mounted the ampoule before injection.

Readily integrating the sensor to the BioInstrumentation Lab's JI was critical.

BI Lab JI | **Pre-Actuator** | **In-Actuator** | **Post-Actuator** | **In-Ampoule**

50 mm
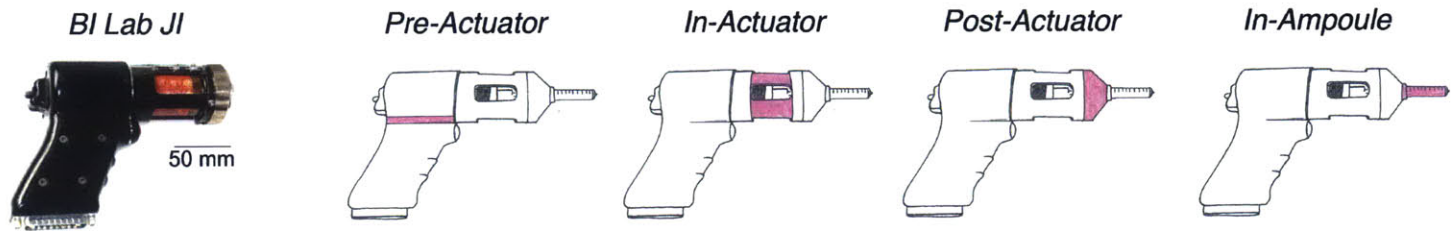
Figure 2-2: The BioInstrumentation Lab's JI is shown on the left, before modifications to implement the force sensor commenced. The four sketches directly to the right show potential locations for the force sensor, highlighted in pink, including pre-actuator, in-actuator, post-actuator, and in-ampoule.

Location: / Functional Requirement:	Pre-Actuator	In-Actuator	Post-Actuator	In-Ampoule
Low Induced Volume Error	+	-	-	+
Bandwidth	--	-	0	+
Shielded	--	-	0	--
Reliability	--	-	0	--
Readily Integrated	0	--	+	--
Cost	0	-	0	--
Agnostic	+	--	0	+
Total:	-4	-9	0	-5

Table 2.2: Pugh chart evaluating sensor locations presented in Figure 2-2 against relevant functional requirements identified in Section 2.2.

The post-actuator location would be best as it would give a significant amount of flexibility with the geometry allowing for relatively easy implementation. The pre-actuator would be second best, as integration at this location would only require a redesign of the handle ergonomics. The in-actuator location would be extremely deficient as the sensor would need to be integrated into the actuator housing. This would mean that not only would the sensor need to be designed and implemented but the structural mechanics, electromagnetic characteristics, and overall actuator performance of the actuator would need to be monitored and maintained as well. The in-ampoule location was also extremely deficient. While all other locations could be readily hard-wired to the data acquisition hardware, a repeatable but removable electrical interface would need to be created between the ampoule and the rest of the device. Given the limited real-estate on the current Injex [11] ampoules used in the device, this could prove difficult from an integration perspective. Additionally, the prospect of mounting the sensor on a disposable part of the device would be extremely problematic.

The associated costs with implementing the sensor at each of these locations would be closely related to integration challenges.

Finally, the pre-actuator and in-ampoule locations could be quite ideal from an actuator-agnostic perspective. Given that the force measurement would occur outside

the structural loop in both cases, the components of the actuator could all be modified without requiring significant redesign of the sensor. The post-actuator location would be moderately agnostic given that the interface between the force sensor and actuator housing would be the only part requiring modification in the event of a change in the actuation method. The in-actuator location would be very deficient. Since the force sensor and actuator would be one unit, changing the actuator would render the previous in-actuator force sensor implementation useless.

The Pugh chart in Table 2.2 outlines the the results from the analysis and research for the sensor location and indicated that the post-actuator location was most ideal for this device.

2.3.2 Sensor Type

A number of physical paradigms exist through which force could be measured and recorded including electrical, optical, and mechanical methods. These can be broken down into particular implementations. First, with electrical methods, sensing implementations include metal foil gauges, force sensitive resistors (FSRs), and piezoelectric transducers to measure strain on or within a substrate. This strain can be related to applied force. With optical methods, laser/photodiode or interferometry setups are potential options to very accurately quantify the movement of a reflector whose displacement can be related to applied force. Lastly, forces can also be measured using mechanical means. One method is through a fluid system using pneumatics or hydraulics to transfer an applied force to a pressure, which can be recorded elsewhere in the fluid. This selection of sensor types, while not exhaustive, represented a reasonable spread for determining an optimal candidate. Each type had its own benefits and drawbacks, which are explored in the Pugh chart shown in Table 2.3 and detailed in the subsequent paragraphs.

Strain gauges rely on a linear elastic behavior of a substrate to repeatably produce a measurable strain given some force. Foil strain gauges are the most widely used and consist of a metal foil (2 to 5 μm thick) on an insulating backing (10 to 30 μm thick) made of epoxy, polyamide, or glass-reinforced epoxy phenolic resin. This assembly is

Paradigm:	Electrical			Optical		Mechanical	
Functional Requirement:	Strain Gauge	FSR	Piezo-electric	Interferometry	Laser/ Photodiode	Hydraulic	Pneumatic
Low Induced Volume Error	+	--	+	++	+	+	-
Resolution	0	--	0	++	+	--	--
Bandwidth	+	+	--	++	++	--	--
Reliability	+	--	--	--	--	--	--
Readily Integrated	++	0	0	--	--	--	--
Cost	0	++	0	--	--	0	0
Total:	5	-3	-3	0	-2	-7	-9

Table 2.3: Pugh chart evaluating possible sensor types against relevant functional requirements identified in Section 2.2.

mounted on a structure to measure local strain. To achieve a very high sensitivity in a small package, the measurement grid pattern and terminal junctions are produced by photo-etching [34].

Given the high bit depth of readily available analog to digital converters (ADC) and particular strain gauge layouts, minute strains can be detected. This means that very small deflections and induced volume errors could be realized while maintaining relatively good resolution. The bandwidth would be dependent on the structural design but could be tuned for the desired performance. Foil strain gauges are very commonly used in the measurement of force and, as such, are commercially available and would be very reliable. Structures can easily be made to produce localized strains and very small foil strain gauge packages can be sourced, making this sensor type a very attractive option from an integration perspective. Foil strain gauges are mass manufactured by the printed circuit industry and therefore could be produced at relatively low unit cost [34].

FSRs are sensors which change resistance based on the applied force. In an FSR, two electrodes are separated by a conductive polymer. When the conductive polymer is compressed, the resistance between the electrodes decreases in a nonlinear fashion. While they are very thin (typically less than 0.5 mm), sensors which have the proper

force range (such as $0 - 440\,\mathrm{N}$ found in Sensitronics 1 Inch ShuntMode FSR [35]) have switch travels on the order of $120\,\mu\mathrm{m}$, far above the maximum specified in the functional requirements of $25\,\mu\mathrm{m}$. Typical FSRs also have force resolutions on the order of 1% of their full scale level, meaning an FSR designed for a $300\,\mathrm{N}$ max force could only resolve to $3\,\mathrm{N}$, which also does not meet the required specification [35]. FSRs have relatively fast rise times (typically below $100\,\mu\mathrm{s}$) [35]. However, the measurements from FSRs currently available are very unrepeatable ($\pm 5\%$ between measurements on the same sensor) causing poor reliability [35]. Size issues would be present with commercial available FSRs but would not be impossible to overcome. FSRs are very low cost (near \$5 in bulk) due to their ability to be screen printed in large volumes [35]. While currently available FSRs may have a place in toys and some industrial applications requiring a binary measure or very rough numeric force value, they should be avoided at all costs in precision measurement equipment.

Piezoelectric force sensors are active elements, meaning that no power supply to the sensor is needed (although amplification of the signal is common). They make use of the piezoelectric effect, which is a phenomenon in some materials where a voltage is generated in proportion to how much the material compressed. Quartz is a common material that exhibits piezoelectric behavior. Piezoelectric sensors are commercially available and very robust (they typically can withstand very high overload forces). However, they are brittle and proper loading conditions are critical to their longevity [34].

Piezoelectric force sensors are very rigid, meaning that the displacement they induce in the force measuring path is very small when loaded. Therefore the error volume induced can also be quite small. Resolution is related to the particular substrate's piezoelectric properties and the ADC. Bandwidth, however, is a particular problem with piezoelectric force sensors. While excellent for fast changing transient forces, a piezoelectric sensor is typically unable to measure static forces due to charge leakage [34]. This is a significant drawback given the force application that the instrument will measure is near steady. Given this fact, the reliability of force measurements for this application would be called into serious question. One issue with commercial

40

Figure 2-3: Electrical paradigms for measuring force including a representative strain gauge (*Left*) [32], FSR (*Center*) [31], and piezoelectric transducer (*Right*) [33].

devices is that they are typically quite large as compared to the real-estate afforded at the front of the BioInstrumentation Lab's JI. System cost is moderate. Images of a strain gauge, FSR, and piezo transducer are shown in Figure 2-3.

Laser interferometry is traditionally more of a displacement measurement method rather than a force measurement method. However, given knowledge of the relationship between applied force and resultant displacement, a laser interferometer is capable of measuring forces. A laser interferometer is an optical system that utilizes the interference intensity between two coherent light sources where one path is fixed and one path is variable. This method can be used to measure distances at resolutions smaller than the wavelength of the coherent light utilized. Hence, very small deformations can be detected and a high stiffness sensor could be realized, allowing for low induced volumetric errors. Rigid structures allow for higher bandwidth, making it easier to attain the specified requirement. However, laser interferometers are delicate optical instruments that can be damaged in a jostle or drop, hurting their reliability. Given the need for a laser source and desire for quality optical components in a small package, integration is a potential difficulty and cost may be high. A Michelson laser interferometer schematic is shown for reference in Figure 2-4.

Laser/photodiode systems are, like laser interferometers, more of a displacement measurement method rather than a force measurement method. However, given knowledge of the relationship between applied force and resultant displacement (or in this case, the rotation of the reflective element), a laser/photodiode system is also capable of measuring forces. A laser/photodiode system is a setup whereby a laser
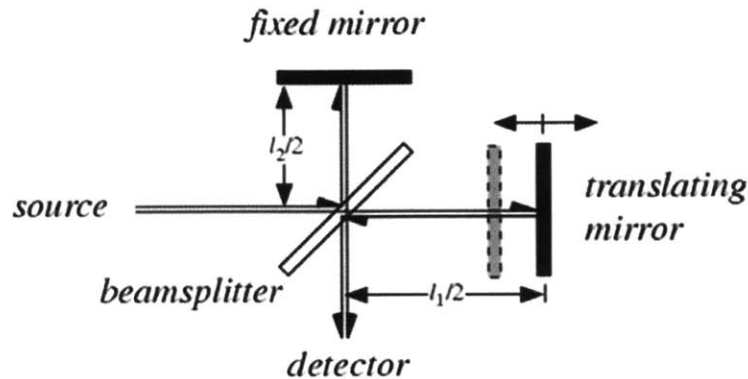
Figure 2-4: A simplified schematic for a Michelson laser interferometer where the translating mirror's movement modifies the light path length and allows for relative displacement to be detected. Given a structure where the elastic deformation properties are known, displacement can be related to applied force. Cycles in the intensity that are detected must be counted and interpolated in addition to the wavelength being known to measure the relative displacement from an initial position. Figure reproduced from [36].

spot is reflected off a surface onto an array of photodiodes. Based on rotation of the reflective surface, the laser spot will activate different photodiodes. This is a common method by which an atomic force microscope measures surface profiles. Resolution would be dependent on the distance of the photodiode from the point of reflection, so achieving extremely high resolution in a small device may prove difficult to achieve. However, laser/photodiode systems are still quite high resolution and would result in low induced volume error. Bandwidth performance would be very good due to the high structural stiffness that could be achieved. Laser/photodiode systems however also contain delicate optical elements that could be damaged in a jostle or drop, hurting their reliability. Due to similar challenges that the laser interferometer would face in requiring small, high quality optical components, integration could also be difficult and cost could be high.

Hydraulic and pneumatic systems utilize a fluid (in hydraulic systems a liquid and in pneumatic systems a gas) to transmit forces applied to a loading surface to a pressure transducer. While liquids (such as oil) are relatively incompressible resulting in very high stiffnesses [34], all other characteristics of these two systems

perform poorly across the relevant functional requirements. Pneumatic systems, due to compressibility of the gas, would result in high volume error. These systems are relatively inaccurate (uncertainties of 1% full scale are common [34]) and the bandwidth in systems with fluid-filled lines would be poor. Any leaks would cause reliability problems and the ability to implement this force measurement paradigm in a small package would prove difficult. While the final system manufacturing cost could be tenable, the calibration and monitoring of such a system could prove cumbersome.

Given the results from this analysis and research, the Pugh chart in Table 2.3 indicated that the foil strain gauge was most ideal for this device. With the decision to utilize this sensor type, it was necessary to create localized areas of strain that would vary linearly with the applied load. Flexural members were an excellent candidate to accomplish this.

2.3.3 Flexure Number

Given the decisions to pursue the use of strain gauge elements at the post-ampoule location, it was now necessary to formulate a design that generated localized areas of strain which could be measured by the sensing elements. Flexural elements formed in a metal substrate were identified as a good candidate to produce near-linear deflection for applied loads when loaded within the elastic limits of the geometry and material. These flexural elements could be analyzed with both 2D beam bending theory as well as finite element analysis (FEA) to optimize performance. Additionally, flexures could be manufactured in-house in the BioInstrumentation Lab's machine shop. As shown in Table 2.4, the number of arms to be utilized in the design was a design parameter that needed to be evaluated, as each had associated benefits and deficits.

In the two-arm design, both vertical bending (in and out of the page in Table 2.4) and torsion of the flexures (along the flexures' long axis) would need to be quantified to measure both normal and lateral forces applied to the tip of the nozzle. While it is relatively straightforward to mount strain gauges on the top and bottom surfaces, reliably mounting sensing elements on the sides of the flexures could prove very cumbersome from a manufacturing standpoint.

Arm Number:	2	3	4
Benefits	Normal load causes no ampoule deflection		
		Single measured bending paradigm	
			Orthogonal lateral sensing
Deficits	Difficult to instrument	Non-orthogonal lateral sensing	Redundant sensors ($)
	Multiple measured bending paradigms		

Table 2.4: Benefits and drawbacks for possible flexure systems including two, three, and four-arm configurations.

In the three-arm design, only vertical bending on each flexure would need to be quantified to measure both normal and lateral forces applied to the tip of the nozzle. A potential downside of this design would be that, because the flexures are not orthogonal to one another, sensing lateral forces could prove more difficult.

In the four-arm design, again only vertical bending on each flexure would need to be quantified to measure both normal and lateral forces applied to the tip of the nozzle. Additionally, the flexures are orthogonal, which would make it more straightforward to relate vertical bending to the applied lateral force. However, since three flexural arms potentially could resolve normal and lateral forces, the four flexural arm design could prove to be more costly from a materials and assembly standpoint.

With all of these designs, a normal load on the tip of the nozzle causes only a deflection in the normal direction and no lateral deflections. Given that lateral forces will be minimized, this means that the axis of the ampoule always will remain parallel to the axis of the piston, keeping friction and wear to a minimum.

Given further work on the sensor model presented in Section 2.4.5, it was determined that the lack of orthogonality could be overcome with a proper model. As
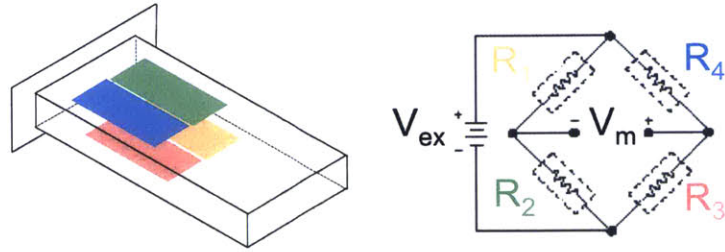
Figure 2-5: This Wheatstone full bridge configuration was identified as an excellent candidate for the strain gauge layout. It is insensitive to temperature variation and very sensitive to vertical bending. Adapted from [37].

such, the design with three flexural arms was determined to be optimal.

2.4 Further Analysis and Research

2.4.1 Gauge Configuration

A strain gauge configuration needed to be identified that was very sensitive to vertical bending and insensitive to all other loading paradigms as well as temperature fluctuations. A particular configuration of the Wheatstone full bridge was identified, as shown in Figure 2-5. As shown in Figure 2-6, the configuration is indeed very sensitive to vertical bending and rejects all other loading paradigms including horizontal bending, axial loading, and torsion. Additionally, as long as temperature variations affect all gauges in the same way, V_m (the measured voltage) will not change.

2.4.2 Flexure Design

Strain gauges integrate the total strain beneath them. This means that whether a strain gauge straddles a compressive and tensile zone equally or is exposed to constant, zero strain, the voltage measurement will be the same. However, a gauge fully in the tensile or compressive zone alone will output a nonzero strain. Therefore to maximize the measurement output, a strain gauge must be mounted in a purely tensile or compressive zone.

Given the two flexure constraint configurations shown in Figure 2-7 (Fixed/Guided
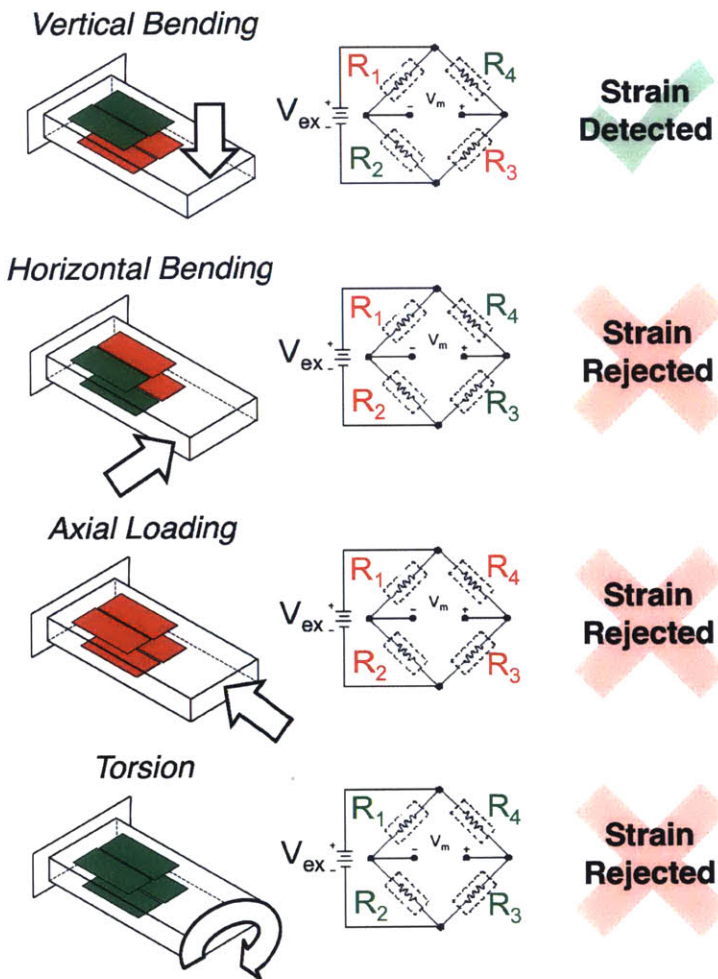
Figure 2-6: The Wheatstone full bridge configuration shown in Figure 2-5 is very sensitive to vertical bending and (ideally) completely rejects all other loads (adapted from [37]). Red indicates compression and a decrease in gauge resistance, green indicates tension and an increase in gauge resistance.

and Fixed/Free), red shading represents surface compression zones and green shading represents surface tensile zones. Given a particular strain gauge length λ, which occupies fully a purely compressive or tensile zone, the minimum flexure length L_{FG} possible in the Fixed/Guided flexure is 2λ whereas the minimum flexure length L_{FF} possible in the Fixed/Free flexure is λ. Therefore from a size perspective, instrumenting a Fixed/Free flexure configuration would result in a device nearly half the size of another employing Fixed/Guided flexures.

Additionally, given the appropriate equations for beam deflections in 2D and the same load W, Young's modulus E, and second moment of area I, as well as the strain gauge length λ, the maximum displacement at the moving end is half for the Fixed/Free than it is for the Fixed/Guided. This difference in displacement directly influences total induced volume error.

While the Fixed/Free is better from both a size and maximum displacement perspective, the obvious deficiency is that there is no connection point to a central hub, which is necessary to hold the ampoule.

A new configuration was devised that borrowed from both of the flexure configurations shown in Figure 2-7. This Fixed/Quasi-Free design, as shown in Figure 2-8, borrows from the Fixed/Free configuration to realize a smaller device size and induced volume error while allowing for a connection to the central hub as with the Fixed/Guided configuration.

To analyze this design initially, a simplified geometry was developed and two-dimensional (2D) beam bending analysis was employed. While this approach did have its limitations (detailed later in this subsection) it did provide interesting insight to the approximate behavior of a 2D flexure with a representative geometry for the Fixed/Quasi-Free design.

The maximum stress in a loaded 2D beam can be described given Equation 2.2,

$$\sigma_{max} = \frac{M c_{max}}{I}. \tag{2.2}$$

Here, M is the bending moment, c_{max} is the maximum distance from the neutral

Fixed/Guided

Fixed/Free

Key

λ - most sensitive strain gauge length

L_{FG} - length of Fixed/Guided

L_{FF} - length of Fixed/Free

δ_{FG} - deflection of Fixed/Guided

δ_{FF} - deflection of Fixed Free

W - load

E - elastic modulus

I - second moment of area

$$L_{FG} = 2\lambda$$

$$L_{FF} = \frac{1}{2}L_{FG} = \lambda$$

$$\delta_{FG} = \frac{WL_{FG}{}^3}{12EI}$$

$$\delta_{FF} = \frac{WL_{FF}{}^3}{3EI}$$

$$Given\ W, E, I$$

$$\delta_{FG} \sim \frac{2}{3}\lambda^3$$

$$\delta_{FF} = \delta_{FG} \sim \frac{1}{3}\lambda^3$$
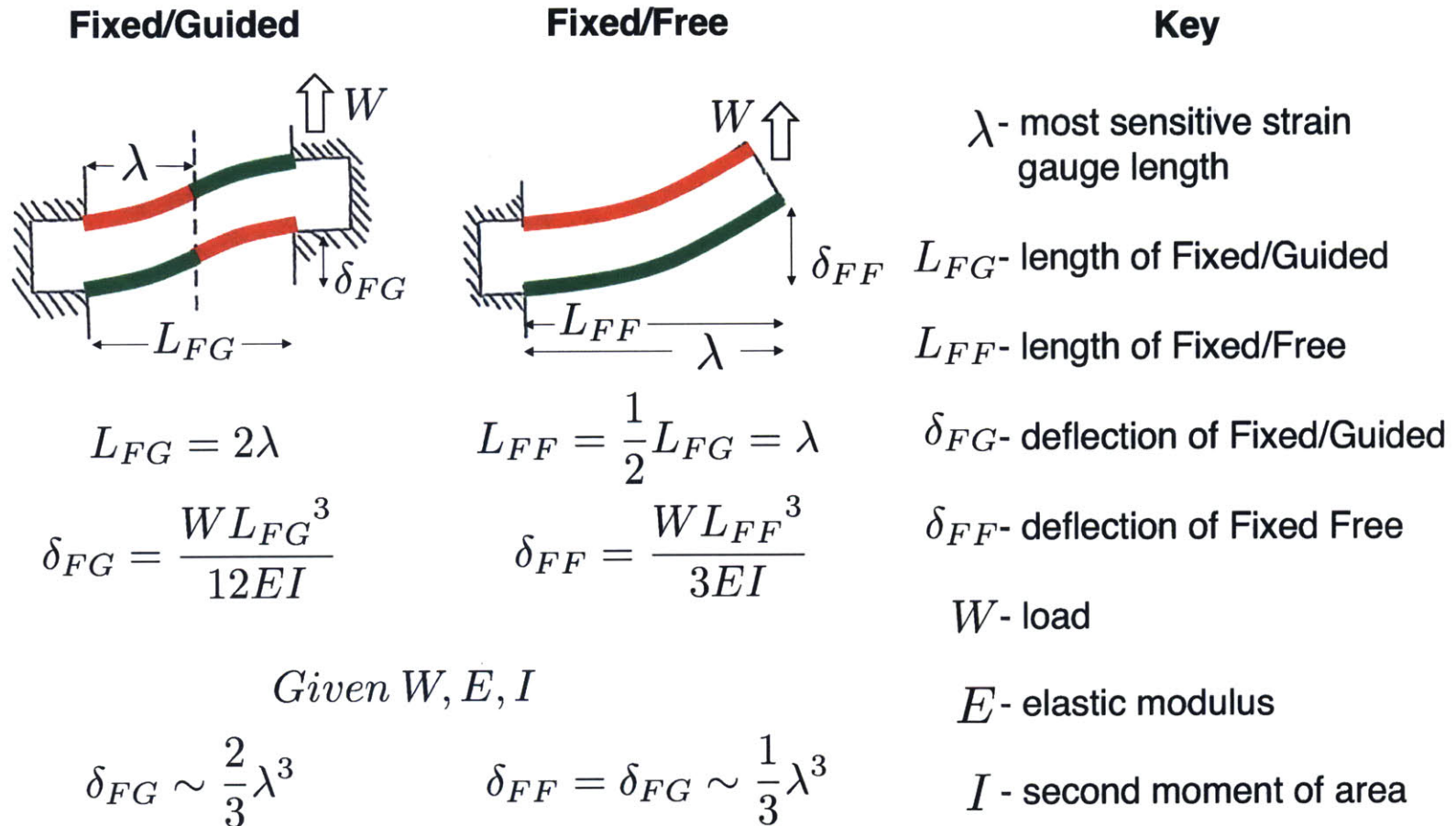
Figure 2-7: Shown here are two flexure constraint configurations. The first configuration on the left is the Fixed/Guided configuration where the left end of the flexure is rigidly mounted to ground and the right end is rigidly mounted to a guided support that can move up and down but resists rotation. The second configuration at the center is the Fixed/Free configuration where the left end of the flexure is rigidly mounted to ground and the right end is free. The associated equations show how the Fixed/Free outperforms the Fixed/Guided configuration in terms of flexure length (and therefore device size) as well as induced volume error given the same material, geometry, load and strain gauge length. The variables used in these equations are defined in the key on the right.
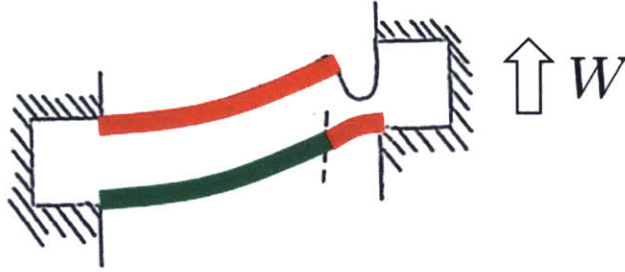
Figure 2-8: Shown here is a conceptual sketch of a Fixed/Quasi-Free configuration. Note the representative change in the surface compressive/tensile zones.

axis, and I is the second moment of area at some location in the beam. Typically, the surface of a flexure will be farthest from the neutral axis. Therefore, the outer surface will experience the greatest stress locally in a particular cross section. The cross section where M is greatest will contain the maximum stress at c_{max} for a rectangular cross-section beam.

Furthermore, the maximum strain can be described given Equation 2.3 where E is the Young's modulus,

$$\epsilon_{max} = \frac{\sigma_{max}}{E} = \frac{M c_{max}}{EI}. \tag{2.3}$$

To ensure that the flexures could resist a large number of loading cycles, it was determined that 0.1% strain should not be exceeded anywhere in the beam. Given the elastic modulus of 72 GPa for 7075-T6 aluminum [38] (the alloy selected for the flexure construction), the stress associated with 0.1% strain would be 72 MPa. This corresponds to a maximum strain of life of well over 10^7 cycles, as shown in the stress versus number of cycles to failure (S-N) curve in Figure 2-9.

It was therefore necessary to determine an estimate of the bending moment M at the ends of the beam where strain would be greatest to ensure ϵ_{max} would be less than 0.1% to meet the design criterion. As shown in Figure 2-10 on the top row, the Fixed/Quasi-Free loads could be broken into two parts including an applied

49

Figure 2-9: This plot shows cyclic stress-life curves for 7075-T6 aluminum alloy in air. This alloy was used for the flexure system. The x-axis represents cycles to failure. Reproduced from [39].

load W and an applied moment M_a. The bending moment along x in each of the individual loading conditions could then be plotted, as shown in the second row of Figure 2-10. W w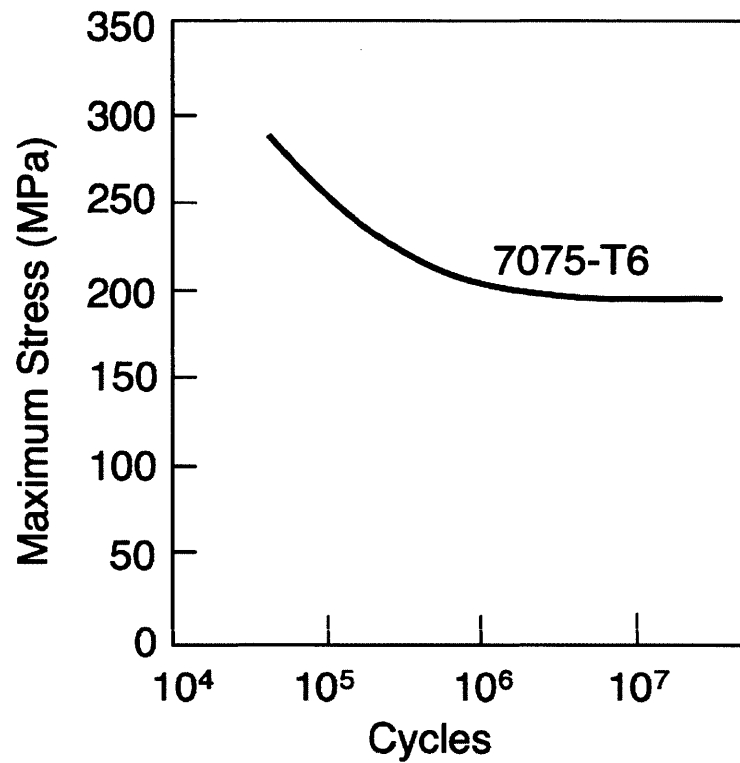as assumed to be 300 N, which is 50% more force than the BioInstrumentation Lab's actuator is capable of exerting [18] for a moderate factor of safety. Additionally, the flexure geometry and material could be prescribed for a particular configuration being scrutinized. The only unknown variable remaining was M_a. If M_a could be found, so could an estimate for M (and thereby ϵ_{max}) which would allow for comparison to the maximum strain design criterion for particular flexure geometries.

With the cutout in the representative geometry, assumptions were made regarding the second moment of area I. I_1, shown in Equation 2.4, was for the section with height h and width b. I_2 shown in Equation 2.5 was for the cutout with height $h - a$ and width b. For I_2, the parallel axis theorem was used. The parallel axis was assumed to be located at $h/2$ and the neutral axis of the rectangular profile was assumed to be located at $\frac{h-a}{2}$. Therefore,

$$I_1 = \frac{bh^3}{12},$$ (2.4)

and

$$I_2 = \frac{bh^3}{12} + b(h - a)(\frac{h}{2} - \frac{h-a}{2})^2.$$ (2.5)

These second moments of area were multiplied by the Young's modulus E and plotted in the third row of Figure 2-10. Note that the plot is the same for both the applied load and moment since these are superimposed on the same geometry.

The plots in row four of Figure 2-10 result from the plots of M being divided by the plot of EI along x. The two individual responses can be superimposed to achieve an approximation for M/EI in the actual loading condition with both load and moment applied, as shown in the bottom left in Figure 2-10.

According to Mohr's First Theorem, "the change in slope over any length of a member subjected to bending is equal to the area of the curvature diagram over that

length" [40]. Since it was assumed that the slope of the beam at either end was horizontal (due to the beam's similarity to the Fixed/Guided behavior), this meant that the area under the curve in the bottom left of Figure 2-10 was zero. As such, it was possible to find M_a and thereby ϵ_{max} given that W and the geometric and material parameters for a particular flexure were known.

With M_a set so that the area under the M/EI curve was zero, it was now possible to observe that a transition from a compression to tensile zone (or *vice versa*) occurred at the point where M/EI was zero (and, by Equation 2.3, surface strain was also zero). In examining the final plot of M/EI shown in the curve in the bottom left of of Figure 2-10, λ represents the most sensitive (and optimal) strain gauge length. It is neither too small to miss some of the measurable zone it occupies nor too large to span both compressive and tensile zones where measured strains could cancel each other. Prepared and modeled in Matlab® [41], Figure 2-11 shows the optimal ratio of total flexure length L to the strain gauge length λ with a flexure height of $5\,\text{mm}$ and width of $4.4\,\text{mm}$. Additionally, the flexures used in the final design described in Subsection 2.4.3 (after optimizing in FEA) utilized a normalized cutout height of 0.5, which is indicated by the vertical black dashed line.

With knowledge of M, predictions of ϵ_{max} as percent strain could be made for various cutout heights. Figure 2-12 shows the results, again modeled in Matlab® [41]. The green line at 0.1% maximum strain represents the design criterion. The red and blue lines represent maximum strain estimates at different parts of the geometry. The red line represents the maximum percent strain at the Fixed end. The blue line represents an estimate of the maximum percent strain at the Quasi-Free end. Again, the flexures used in the final design utilized a normalized cutout height of 0.5, which is indicated by the vertical black dashed line.

While this analytical exercise did indeed provide an interesting insight to the ideal behavior of a 2D flexure with a representative geometry and does indicate a benefit associated with the addition of the cutout, it was limited in a few areas. First, the position assumptions for the neutral axis and rectangular profile centroid for the Quasi-Free end of the flexure may not be realistic. Second, as the flexure

52
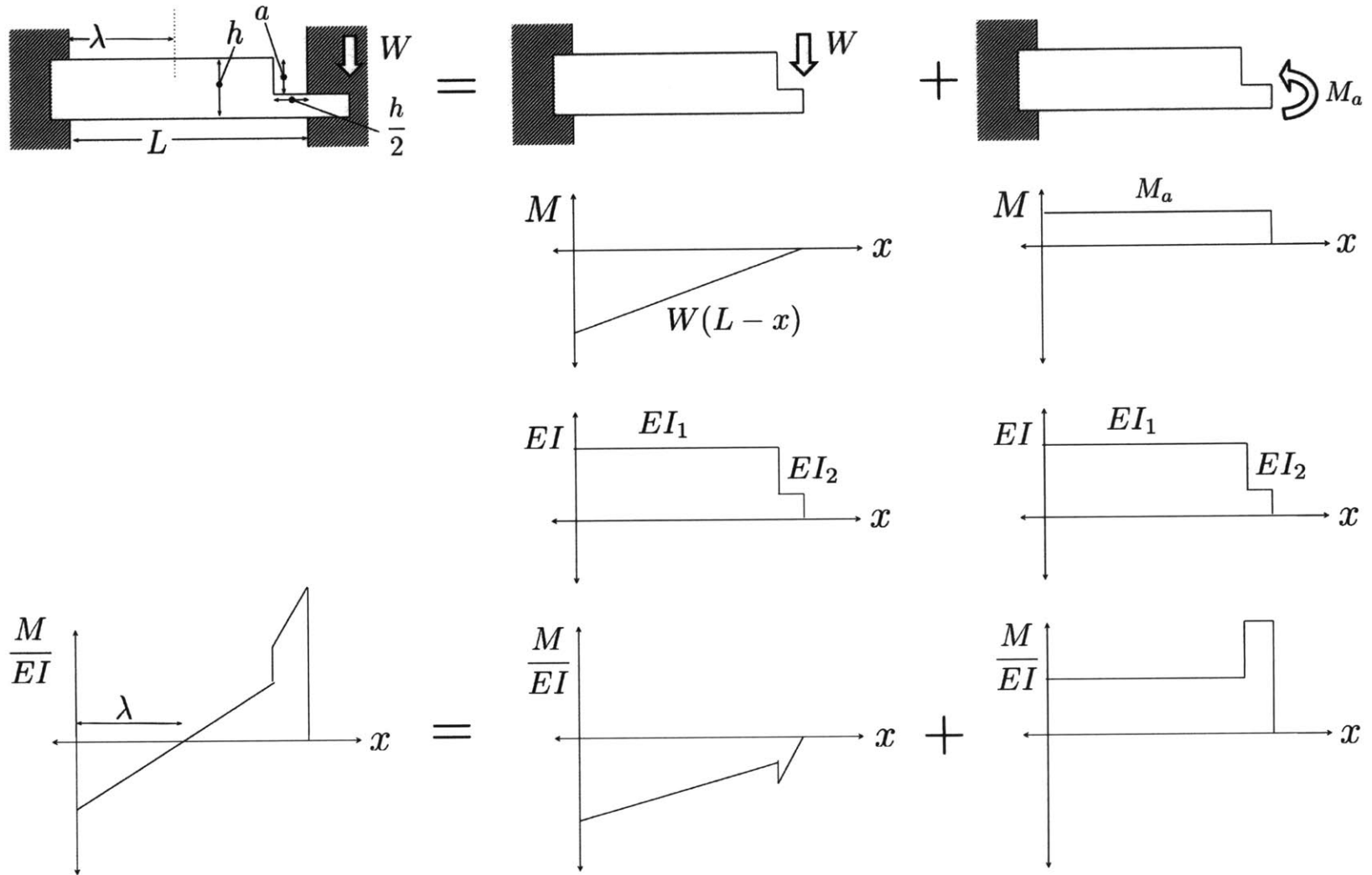
Figure 2-10: Bending in the Fixed/Quasi-Free flexure can be broken down into an applied force W and moment M_a applied to the Quasi-Free end, as shown in the first row. The associated moment versus x position plots are shown in the second row. The third row shows the second moment of area for the simplified beam geometry (specified by I_1 and I_2) multiplied by the Young's modulus E. Note that the plot is the same for both the applied load and moment since these are superimposed on the same geometry. The fourth row shows the results from the plots of M being divided by the plot of EI along x. The two individual responses can be superimposed to achieve an approximation for M/EI for the simplified geometry induced by the load and the Fixed/Quasi-Free guided constraint. h represents the flexure height, a represents the cutout height, L represents the total flexure length, and λ represents the most sensitive (and optimal) strain gauge length.

Flexure L/λ vs. a/h Design Space
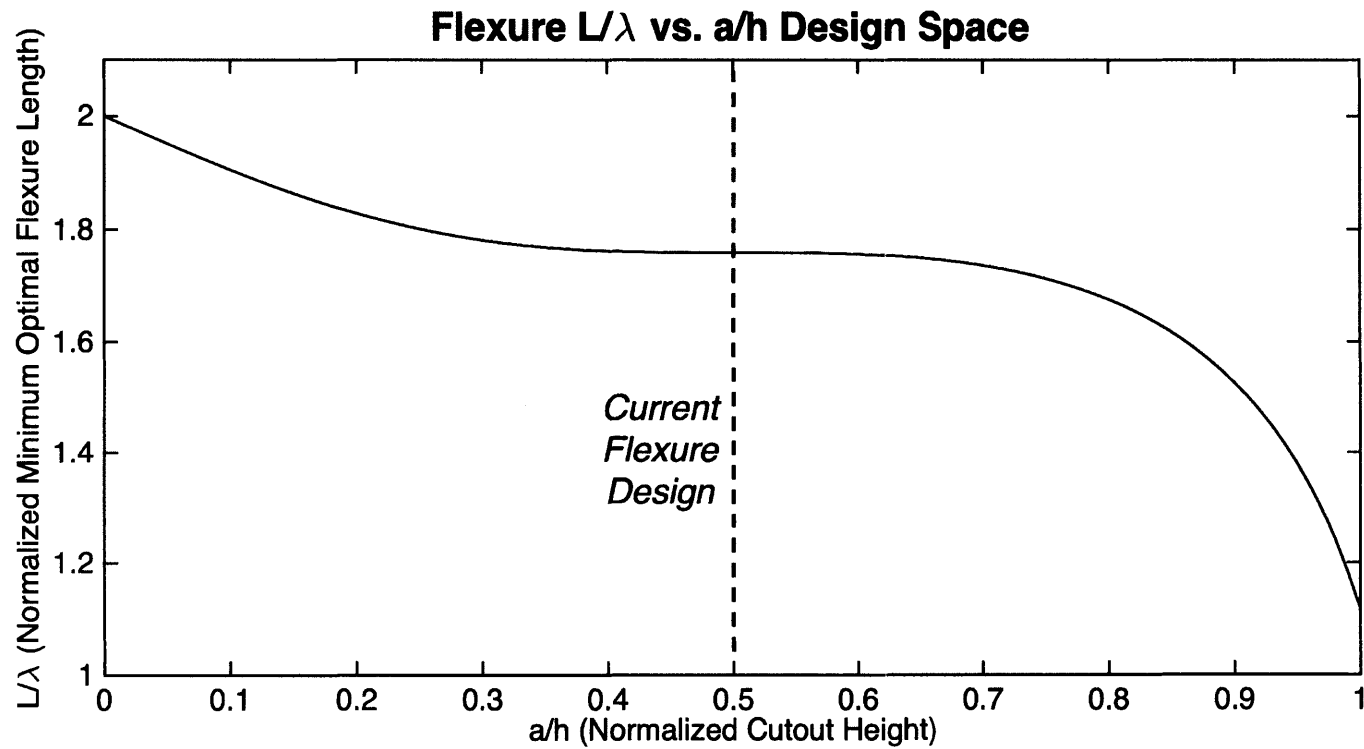
Figure 2-11: This figure shows the optimal ratio of the total flexure length L to the strain gauge length λ for various cutout heights a/h with a flexure height of 5 mm and width of 4.4 mm. Additionally, the flexures used in the final design investigated in Subsection 2.4.3 (after optimizing in FEA) utilized a normalized cutout height of 0.5, which is indicated by the vertical black dashed line. Note that the behavior approaches the expected limiting cases of Fixed/Guided (when $a/h = 0$) and Fixed/Free (when $a/h = 1$) presented in Figure 2-7.
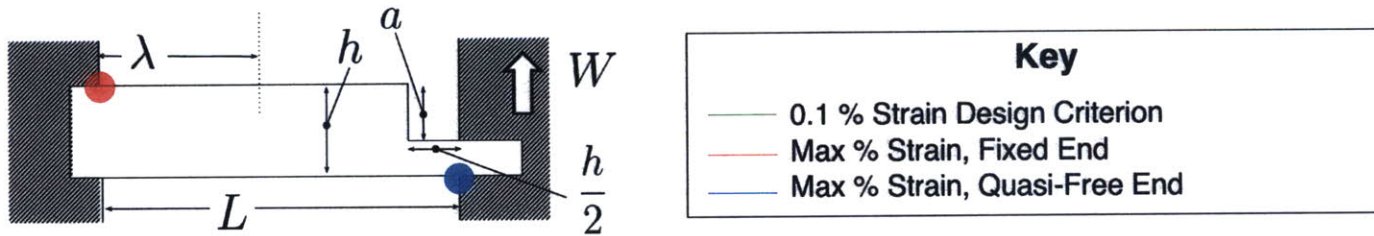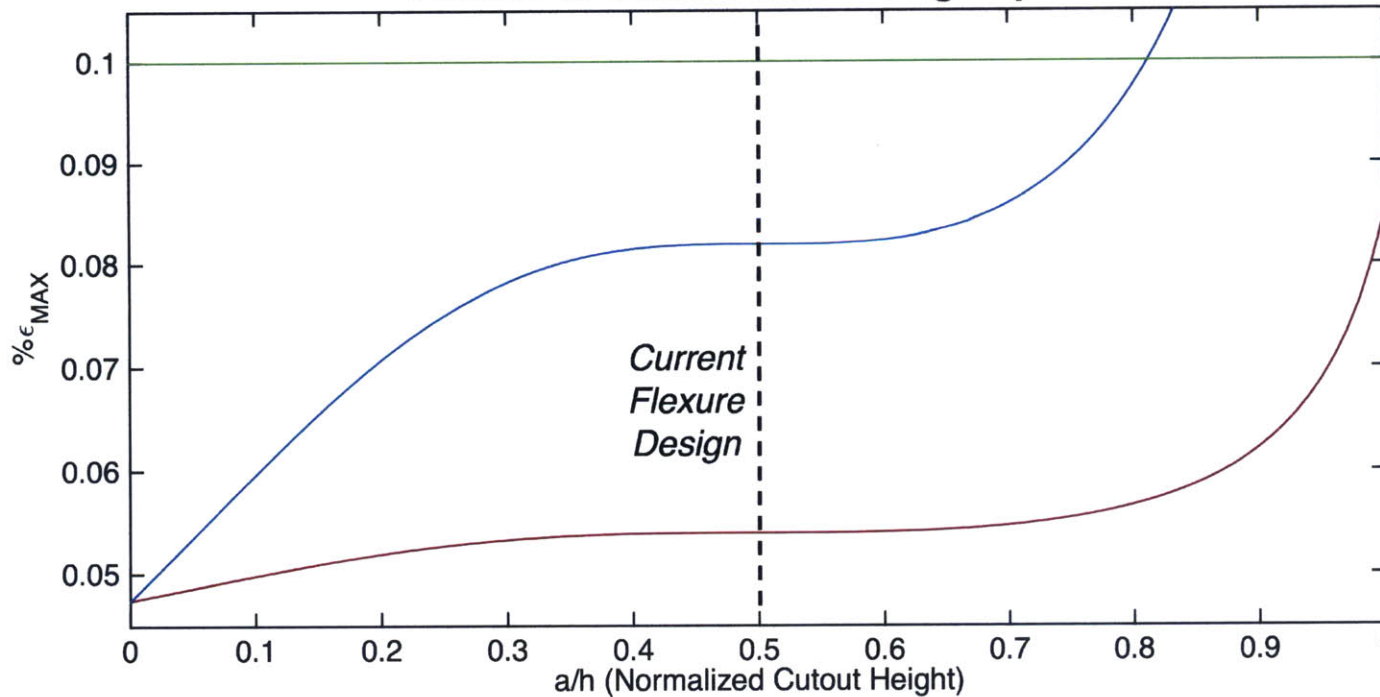
Figure 2-12: Plotted here are the results of the Matlab® [41] analysis for strain in the locations noted in the graphic in the upper left. The green line at 0.1% maximum strain represents the design criterion. The red line represents the maximum percent strain at the fixed end. The blue line represents an estimate of the maximum percent strain at the quasi-free end. The flexures used in the final design presented in Subsection 2.4.3 (after optimizing in FEA) utilized a normalized cutout height of 0.5, which is indicated by the vertical black dashed line. As expected, the strains in the locations specified are equal when $a/h = 0$. As a/h approaches 1, the strain experienced at the Quasi-Free end increases very rapidly (compared to the strain at the Fixed end) as the cross section decreases at the Quasi-Free end.

becomes more stubby (where the thickness approaches the total length), edge effects are likely and 2D flexure analysis gives an inaccurate measure of uniform bending along the width of the beam. Third and last, stress concentrations are important and will exist in this loaded geometry, although the magnitude was not calculated in this analysis. While displacement analysis could have been conducted with the 2D model, these deficiencies made a good case to transition to finite element analysis (FEA) for the remainder of the optimization. FEA would help characterize the structural performance of the flexure system and to ensure that the final design met specification in terms of resolution, maximum strain, and induced volume error.

2.4.3 Static FEA

Finite element analysis (FEA) is a method of predicting the behavior of a solid body under static or dynamic loading conditions. FEA is the practical application of the finite element model. This model takes nodes, which form the shape of the part geometry, and connects them with finite elements. The structural mesh which is formed is set to the appropriate material properties. Constraints and loads are placed on the mesh and an algorithm numerically solves a very large system of equations to produce an estimate of the behavior [42].

For this design optimization, the Solidworks® FEA package [43] was used to estimate both static and dynamic behavior. The geometry was analyzed and iterated upon so that the total displacement, elastic deformation, and expected resolution met performance requirements.

Figure 2-13 shows the resultant maximum displacement of 24.19 μm from a 300 N axial force which was exerted by the piston on the central hub, which is 50% more force than the BioInstrumentation Lab's actuator is capable of outputting [18] as in the 2D analysis. This met the functional requirement of 25 μm maximum axial displacement.

Figure 2-14 shows the resultant maximum stress of 227.0 MPa. A 300 N axial force was exerted on the flexure. Given 7075-T6 aluminum has a yield strength of 510 MPa, plastic failure could not occur when the device fired [38]. A high number of

Figure 2-13: A 24.19 µm maximum displacement results from a 300 N axial force exerted by the actuator on the flexure system in Solidworks® [43] static FEA. This met the functional requirement of 25 µm maximum axial displacement.

firings (upwards of 10^6) were also possible given the fatigue properties shown in the S-N curve in Figure 2-9 and the maximum stress results from FEA.

Figure 2-15 shows the resultant strain distribution due to a 300 N axial force exerted by the piston. To confirm that this distribution of strain resulted in a measurable voltage, a first-order estimate of the voltage output was necessary. To estimate this, first the the gauge factor (GF) was needed, which is a measure of the normalized resistance change ($\delta R/R$) for a given average strain under the gauge (ϵ) as given by the following equation:

$$GF = \frac{\delta R/R}{\epsilon}. \tag{2.6}$$

A more useful form of this equation is as follows, where if GF, ϵ, and R are known, δR can be predicted and and a determination of the voltage output (given the bridge layout specified in Figure 2-5) for a given force can be made as in Equation 2.7,

$$\delta R = (GF)(\epsilon)(R). \tag{2.7}$$

The OMEGA® dual-grid precision strain gauge SGD-3/350-DY41 (shown in Figure 2-16) was selected due to its small size and dual-grid configuration for ease of
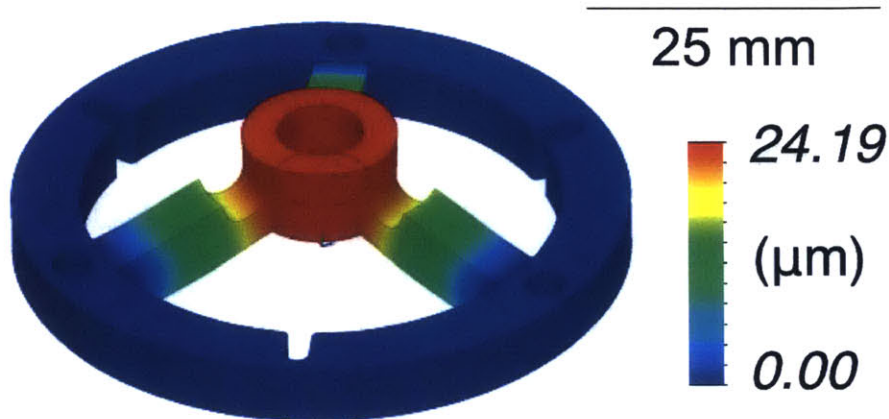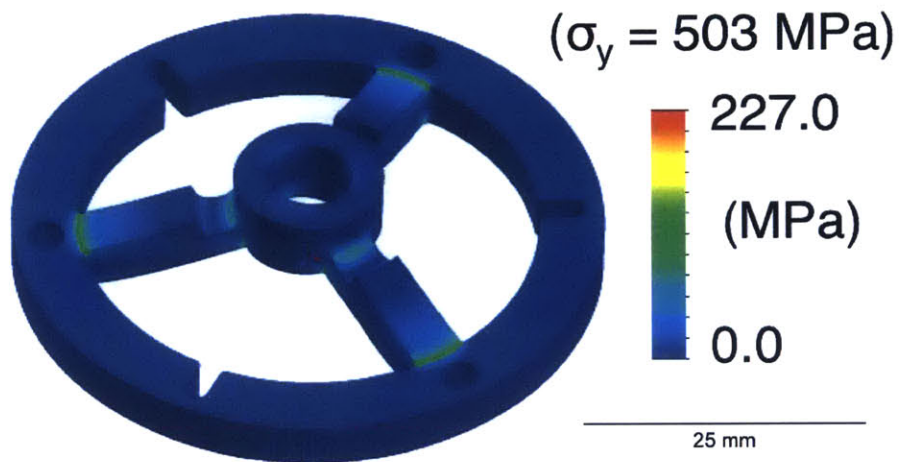
Figure 2-14: A 227.0 MPa maximum stress results from a 300 N axial force exerted by the actuator on the flexure system in Solidworks® [43] static FEA. Plastic deformation would not occur as the yield stress σ_y is 510 MPa for 7075-T6 aluminum alloy [38]. A high number of device firings (upwards of 10^6) were also possible given max stress experienced and the fatigue properties shown in the S-N curve in Figure 2-9.
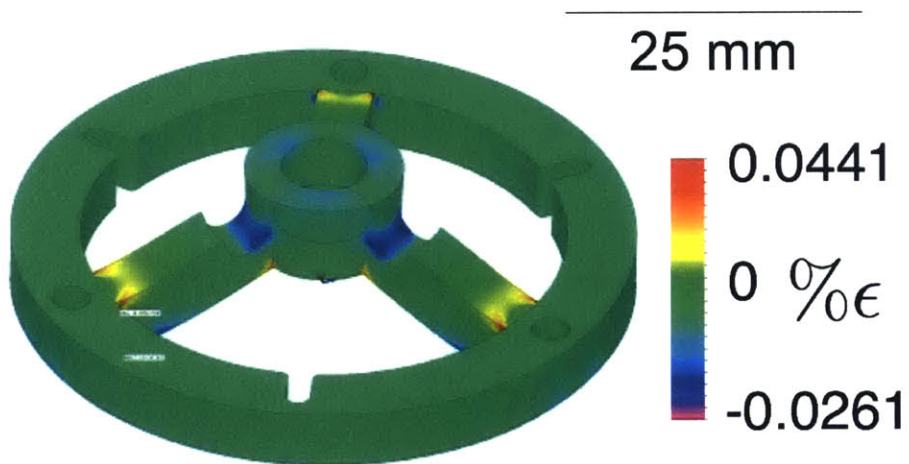

Figure 2-15: Resultant percent strain distribution due to a 300 N axial force exerted by the actuator on the flexure system in Solidworks® [43] static FEA.
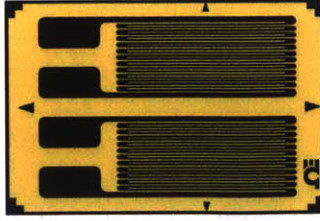
Figure 2-16: Shown here is an illustration of the OMEGA® dual grid strain gauge package SGD-3/350-DY41 [32] which was selected based on the small size and convenient dual-grid configuration for ease of assembly. The gauge carrier dimensions are 6.00 by 4.10 mm and the resistance of each individual grid is 350 Ω [32].

assembly. These gauges have a GF equal to approximately 2.14 and a resistance of 350 Ω [32].

Next, the average strain measured under the bridge was needed and a first-order estimate was formulated. The gauge would occupy a length as shown in Figure 2-17. The average strain measured by the gauge could be modeled by Equation 2.8. Given some average strain ϵ_{strain} which acts over a strained length l_{strain} and the total length that the gauge occupies l, this equation gives an approximation for average strain under the gauge ϵ. A conservative underestimate of l_{strain} ensured ϵ was conservative as well, given:

$$\epsilon \cong \frac{l_{strain}}{l}\epsilon_{strain}. \tag{2.8}$$

From Equation 2.8, ϵ could be determined using the results from FEA. ϵ could then be inputted to Equation 2.7 along with GF and R to find δR. When computed and the arrangement of the circuit (as shown in Figure 2-5) was accounted for, 2.64 μV/N was expected. An National Instruments™ (NI) 9237 simultaneous bridge module [28] was to be used and given the module's range and 24 bit ADC, a theoretical maximum resolution of 2.38 nV was possible. Of course in reality, one or two bits on any ADC are lost and can not be counted on. However, there still would be close to three orders of magnitude between the minimum required instrument resolution (0.5 N) and the minimum theoretical resolution (~0.9 mN), which indicated the system would achieve the required resolution specification.
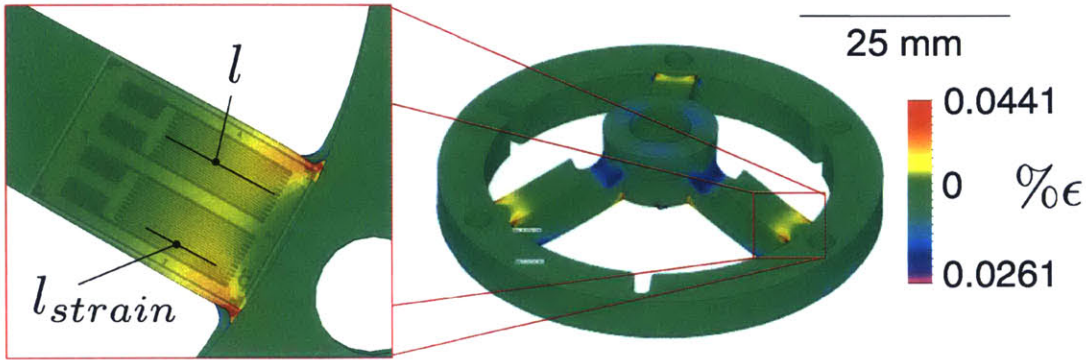
Figure 2-17: Detail showing location of gauge (overplayed on left image) with length l, with respect to the strain distribution originally shown in Figure 2-15 and reprinted on the right for reference, as calculated in the FEA studies resulting from a 300 N axial force. The strained length l_{strain} is also noted.

2.4.4 Dynamic FEA

In addition to static FEA, it was also important to characterize the resonant modes of the structure. For this, Solidworks® FEA [43] was also employed. Figure 2-18 shows the first five resonant modes of the structure. The first resonant mode at 12.17 kHz was of most potential concern. Again under the simplifying assumption that the system would behave as a one dimensional mechanical oscillator (where $\sqrt{\frac{k}{m}} = \omega$) and the mass of the flexure structure was comparable to the mass of the ampoule, doubling the supported mass could result in the first resonant frequency decreasing to $\sim 0.707\omega$. Therefore, the addition of the ampoule (and doubling of the effective mass) would likely decrease the first resonant frequency to $\sim$8.6 kHz. While this dynamic FEA analysis was heavily simplified, it did show that the design was in the correct order of magnitude to meet the functional requirement of a flat response to 5 kHz. More detailed dynamic FEA is presented in Section 4.3 where dynamic FEA on the final design of the supporting structure is presented.

2.4.5 Sensor Model

A sensor model was required which related measured voltages V_{m1}, V_{m2}, and V_{m3} from each flexure to output normal and lateral forces applied to the tip of the nozzle. The

Figure 2-18: This sequence of simulation results, performed in Solidworks® [43], shows the first five resonant modes of the isolated flexure system. The simulated resonant modes A, B, C, D, E fall at 12.17, 17.48, 17.48, 26.15, and 32.08 kHz respectively.

block diagram shown in Figure 2-19 outlines the process by which this is accomplished.

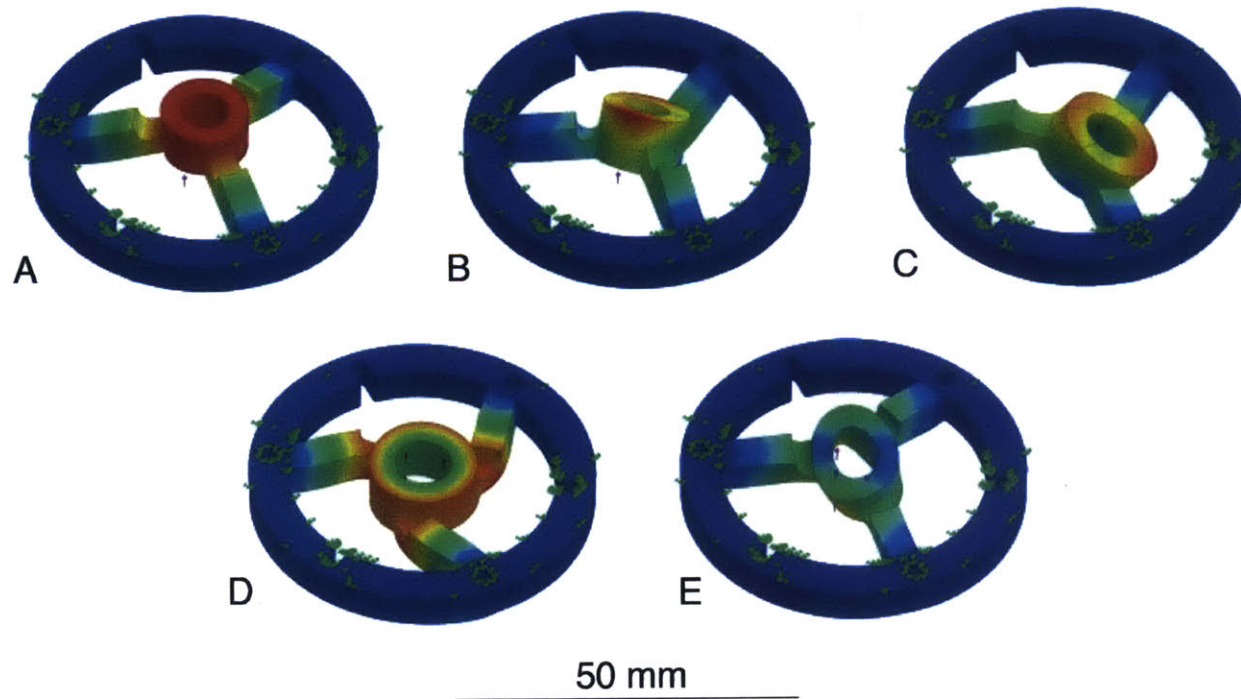First, a pure nonzero normal force can be applied to the tip of the nozzle. Vertical bending, equally distributed between the three flexures, is measured as three voltages V_{m1}, V_{m2}, and V_{m3}. It is assumed that the unloaded value of V_{m1}, V_{m2}, and V_{m3} has been zeroed. These voltages are multiplied by experimentally determined linear calibration coefficients, C_1, C_2, and C_3 respectively, to output the load supported by each flexure in newtons. The sum of the force supported by all three flexures is the total normal force applied to the nozzle. Equation 2.9 shows this relationship,

$$F_{normal} = C_1 V_{m1} + C_2 V_{m2} + C_3 V_{m3}. \qquad (2.9)$$

Second a pure nonzero lateral force can be applied to the tip of the nozzle in either the X or Y direction, as shown in Figure 2-19. The first block, "Resolve X and Y Lateral Values (Geometric)" takes the measured voltages V_{m1}, V_{m2}, and V_{m3}, normalized by the coefficients C_1, C_2, and C_3, and outputs an unscaled representation of the X and Y lateral forces applied to the tip of the nozzle. This process assumes the following:

- The instrument is only sensitive to vertical bending of the flexures.

- Vertical bending is linearly related to the magnitude of the applied lateral force on the nozzle.

- The degree of vertical bending (which is measured) versus torsion (which is rejected) is trigonometrically related to the angle of the applied lateral force on the nozzle.

Using these assumptions, a model was constructed to resolve lateral forces as shown in Table 2.5. This model, while it appears to double count the trigonometric factors, correctly resolves representations of the applied lateral and normal forces. At this point however, these representations are not yet skewed nor scaled.

Therefore, given a force in the lateral Y direction (shown as F_y in Figure 2-19), a prediction can be made (with the assumptions and model developed) to resolve the
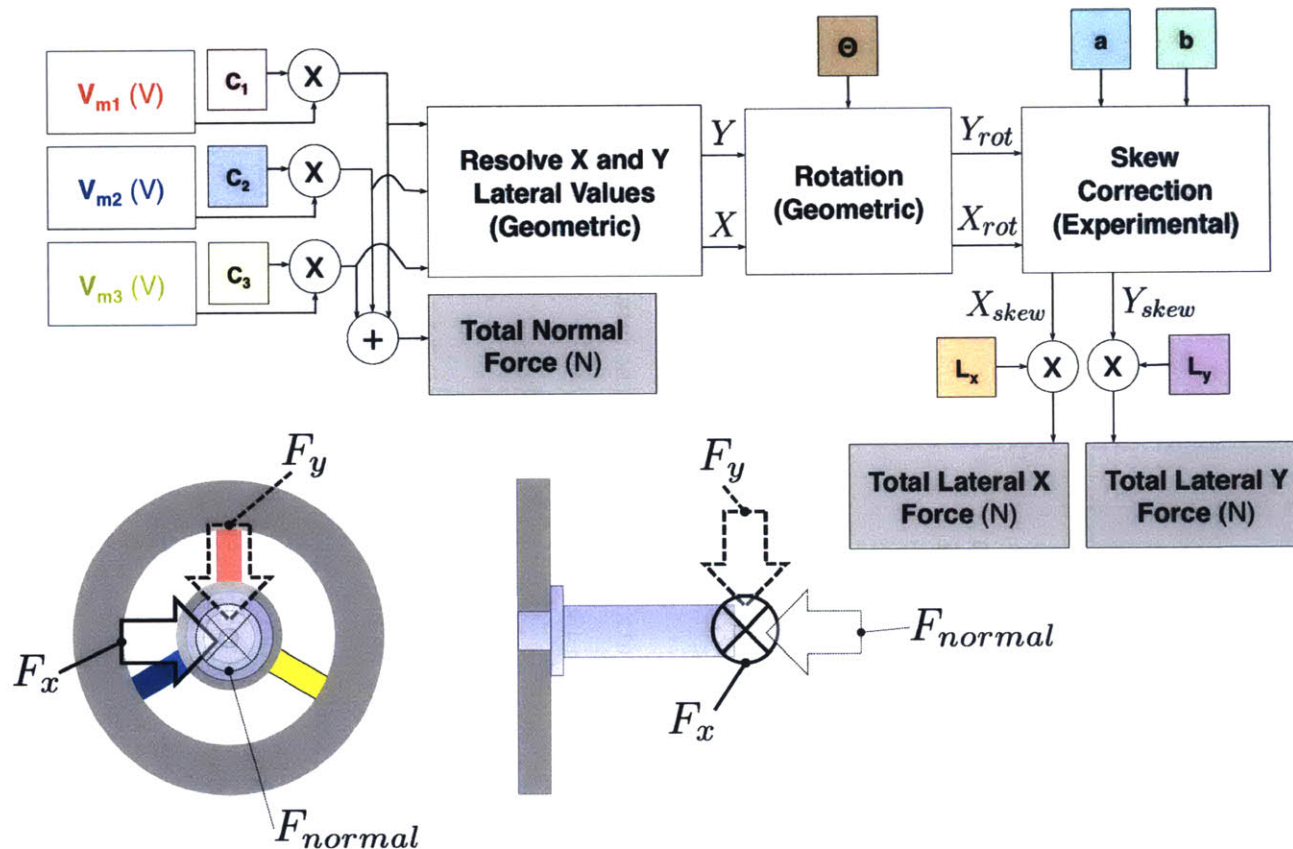
Figure 2-19: This block diagram illustrates the method by which input voltages V_{m1}, V_{m2}, and V_{m3}, induced by normal force F_{normal} and lateral X and Y forces F_x and F_y applied to the nozzle to produce measurements for the normal and lateral forces. C_1, C_2, and C_3 are experimentally determined calibration coefficients for V_{m1}, V_{m2}, and V_{m3} respectively. θ is a geometrical rotation angle between the sensor's axes and the user's axes. a is an experimentally determined skew angle between a resolved force from a pure lateral Y load and the Y axis. b is an experimentally determined skew angle between a resolved force from a pure X load and the X axis. L_x and L_y are experimentally determined calibration coefficients to scale the lateral forces properly. It is assumed that the unloaded value of V_{m1}, V_{m2}, and V_{m3} have been zeroed. The directions of applied normal force F_{normal} and lateral X and Y forces F_x, F_y which result in nonzero V_{m1}, V_{m2}, and V_{m3} are displayed at the bottom. These forces resolved by this scheme are the orthogonal F_{normal} (Total Normal Force), F_x (Total Lateral X Force) , and F_y (Total Lateral Y Force) are shown with respect to the flexure system and ampoule in a top view at the bottom left and left side view at the bottom center.

		Applied Force Direction		
		F_{normal}	F_x	F_y
$V_{m1} =$		1	0	-1
$V_{m2} =$		1	-√(3)/2	(1/2)
$V_{m3} =$		1	√(3)/2	(1/2)
Resolved Lateral Force Representations	Model	Resolved Force Representations		
	X = -√(3)/2*V_{m2}+√(3)/2*V_{m3}	0	3/2	0
	Y = -V_{m1}+(1/2)*V_{m2}+(1/2)*V_{m3}	0	0	3/2

Table 2.5: Shown are the resolved lateral force representations (neither skewed nor scaled) using the model developed. Applied forces follow the assumptions specified. The model correctly resolves the applied lateral and normal forces. It is presumed that C_1, C_2, and C_3 equal 1 for this example.

representation of the force as shown in Equation 2.10,

$$Y = -C_1 V_{m1} + \frac{C_2 V_{m2}}{2} + \frac{C_3 V_{m3}}{2}. \qquad (2.10)$$

A similar equation resolves a representation of the force in the lateral X direction (shown as F_x in Figure 2-19) and is shown in Equation 2.11,

$$X = -C_2 V_{m2} \frac{\sqrt{3}}{2} + C_3 V_{m3} \frac{\sqrt{3}}{2}. \qquad (2.11)$$

Once lateral force representations have been resolved, a number of blocks have been indicated in Figure 2-19 to transform the lateral force representations (X and Y) into accurate measures of the forces applied to the tip of the nozzle (Total Lateral X and Y Forces). The first of these transformations occurs in the "Rotation (Geometric)" block, which rotates the measured coordinate system by angle parameter θ (determined by the angle at which the sensor is mounted) to align the instrument's axes with the user's axes. This transformation is shown in Figure 2-20 and can be represented as the rotational matrix equation below in Equation 2.12:

$$\begin{bmatrix} X_{rot} \\ Y_{rot} \end{bmatrix} = \begin{bmatrix} cos(\theta) & sin(\theta) \\ -sin(\theta) & cos(\theta) \end{bmatrix} \begin{bmatrix} X \\ Y \end{bmatrix}. \qquad (2.12)$$

Next, the "Skew Correction (Experimental)" block skews the lateral forces to ensure that the measurements in the lateral plane are orthogonal. It utilizes angle parameters a and b, which are determined experimentally, to correct the Y_{rot} and X_{rot} to Y_{skew} and X_{skew} respectively. This is shown in Figure 2-20 and represented in the matrix equation below in Equation 2.13:

$$\begin{bmatrix} X_{skew} \\ Y_{skew} \end{bmatrix} = \begin{bmatrix} 1 & -tan(a) \\ -tan(b) & 1 + tan(a)tan(b) \end{bmatrix} \begin{bmatrix} X_{rot} \\ Y_{rot} \end{bmatrix}. \qquad (2.13)$$

Finally, linear calibration coefficients L_y and L_x multiply Y_{skew} and X_{skew} respectively to produce the total lateral Y and X forces (F_y and F_x). L_y and L_x are found experimentally during the calibration procedure.

2.5 Risks and Countermeasures

The identification of potential risks as well as countermeasures to combat these pitfalls is a critical part of the *FRDPARRC* approach that helps identify issues before designs are implemented. In the following subsections, various risks and associated countermeasures are presented for various parts of the design. Risks that were mentioned in Section 2.3 are presented along with other risks that were identified, as well as the associated countermeasures.

2.5.1 Sensor Location

While the post-actuator location was identified as the most ideal choice out of the options presented in Table 2.2, it was not without its own deficits and associated risks that needed to be addressed. Table 2.6 outlines the risks and associated countermeasures, which are discussed in detail below.

Since the sensor, at the post-actuator location, is part of the structural loop through which forces will be transmitted when the device is fired, volume error may be induced. The countermeasure is that the flexure design can be tuned to achieve the appropriate displacement and strain distribution, as was done in the FEA iteration

65
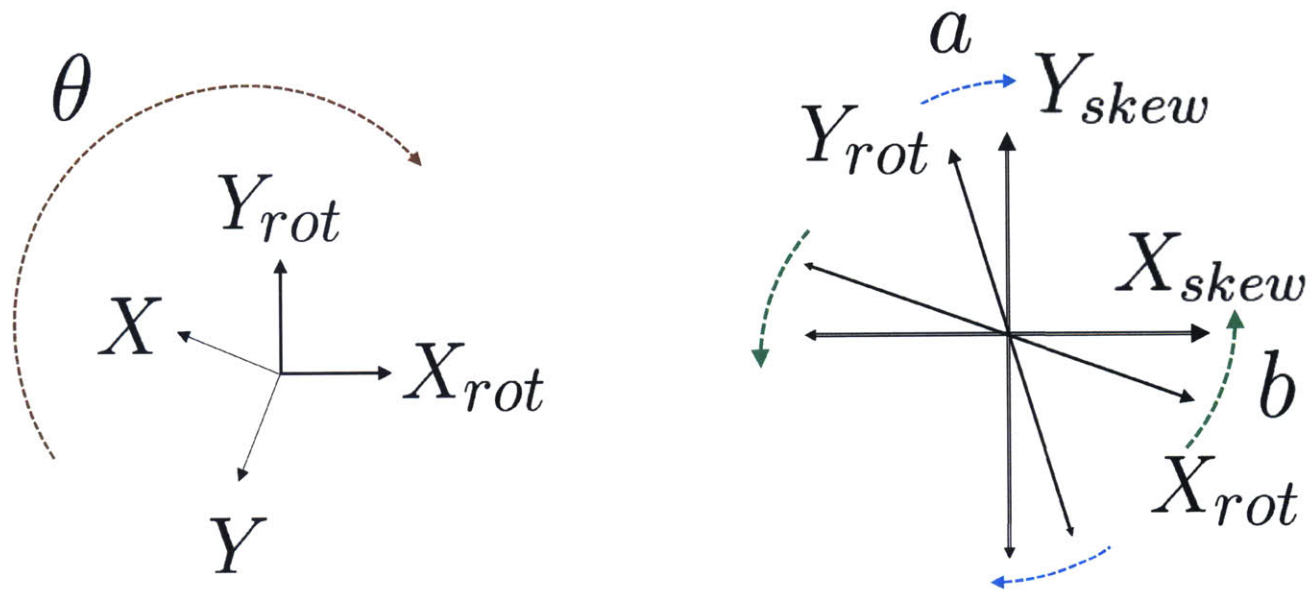
Figure 2-20: (*Left*) Shown here is a simple schematic showing how the sensor's axes are aligned with the user's axes. Presuming the user's axes are oriented like a traditional cartesian coordinate system for the reader, the sensor is mounted at a rotation of $-\theta$ due to geometric requirements of the JI. A rotation about the origin of angle θ is required to properly align the sensor's output. This is what occurs in the "Rotation (Geometric)" block in Figure 2-19. (*Right*) Shown here is a simple schematic indicating how the sensor's lateral axes are orthogonalized. The input axis system is skewed by angle parameters a and b, which relate the original and desired Y and X axes directions respectively. This is what occurs in the "Skew Correction (Experimental)" block in Figure 2-19.

Risks	Counters
Volume error due to location within structural loop	Careful design of flexures
Sensor may impede use of JI	Protect with cover
	Keep size manageable
Difficult to get signals out	Utilize flexible ribbon cables
	Wireless connectivity

Table 2.6: Risks and countermeasures with installation of sensor at post-actuator location.

presented in Subsection 2.4.3. Additionally, the presence of the sensor in the structural loop may actually prove to be a benefit, as it can measure forces exerted through the structure when the device fires and potentially give an indication of pressure in the ampoule.

With the close proximity between the sensor and the injection site, another potential risk is that the sensor may impede use of the JI. This includes issues associated with the size of the sensor blocking a view of the injection site from the user, as well as issues associated with having a delicate instrument exposed at the front of a device. The countermeasures to these risks are relatively straightforward and obvious. Protecting the sensor with a cover or shield will resolve the latter. Keeping the device compact to allow the user to keep the injection site in view will resolve the former.

Last but not least, the post-actuator location does pose a challenge in extracting the signals from the device. A flexible ribbon cable could be utilized to route the signals along the side of the actuator and into the handle. Given that the device is already tethered, it is reasonable to extract signals through a cable that extends along the pre-existing cords. Additionally, wireless connectivity may prove to be beneficial if such a system is not bandwidth limited.

Risks	Counters
Lack of force sensitivity	Careful design of flexures
Sensitive to temperature	Full bridge layout
High cost	Single PCB construction

Table 2.7: Risks and countermeasures with foil strain gauge sensor type.

2.5.2 Sensor Type

While foil strain gauges were identified as the most ideal choice out of the options presented in Table 2.3, they were not without their own deficits and associated risks that needed to be addressed. Table 2.7 outlines the risks and associated countermeasures, which are discussed in detail below.

Given that the optimization of displacement, maximum stress, and instrument sensitivity is occurring simultaneously, it was possible that it would not be possible to meet the requisite specifications on all three with some geometries. However, given the FEA iteration presented in Subsection 2.4.3., it does appear that the specifications can be met thanks to careful iteration on the design. More work may be completed to further optimize the performance.

This instrument will be mounted on the front of a portable device and, as such, the ambient temperature in which the device functions can not be presumed constant. Variations in temperature will be compensated for by the full bridge circuit layout presented in Figure 2-5.

While certainly not the most expensive force measurement implementation of those presented in Table 2.3, the prospect of custom machined flexures (as presented in Subsection 2.4.3) with manually mounted strain gauges is potentially a costly proposition. As such, steps could be taken to reduce the cost associated with raw materials and direct labor. One such step would be to form the strain gauges in a single flex printed circuit board (PCB) to be mounted onto a metal flexure system. Another option would be to form the strain elements directly onto a PCB substrate,

68

Risks	Counters
Mounting Difficulties	Dual-bridge strain gauges
Thermal/Mechanical Stability	Thermally stable cyanoacrylate adhesive
	Proper surface preparation

Table 2.8: Risks and countermeasures with gauge configuration.

doing away completely with the custom aluminum flexure. However, as production would be low-volume during the development phase, these improvements may only realize their cost saving benefits in future iterations if the device is mass manufactured. Additionally, the two-dimensional and FEA beam bending analysis metal structures is well understood, so proven analysis tools could be employed to optimize the design, as described in this chapter. Analysis may not have been as straightforward with composite beams made of PCB substrate material.

2.5.3 Gauge Configuration

While the full bridge circuit was identified as an ideal candidate for the foil gauge layout given its sensitivity to forces as detailed in Figure 2-6, it was not without its own deficits and associated risks that needed to be addressed. Table 2.8 outlines the risks and associated countermeasures, which are discussed in detail below.

Given the small size of the flexures and associated gauges, precise alignment of the gauges could prove difficult, especially if each had to be mounted individually. As such, dual-grid strain gauges as shown in Figure 2-16 were identified as an ideal commercial candidate as opposed to single-grid gauges, which would help reduce installation time.

Thermal and mechanical stability were important factors for a robust device. If the gauge adhesion to the flexure failed, the device would give erroneous readings. Loctite® 498 Super Bonder® ethyl cyanoacrylate was identified as an appropriate adhesive given its wide range of stable operating temperatures from $-54\,°C$ to $82\,°C$

69

and compatibility with metals and plastics [44]. Additionally, proper surface preparation was researched and a procedure by which the gauges could be reliably fixed to the flexure was developed [45]. This procedure is detailed in Subsection 3.1.3.

2.5.4 Sensor Model

Originally, the sensor model did not contain the "Skew Correction (Experimental)" block. This block was added to counter the risk that the assumptions made in Section 2.4.5 were inaccurate. This block would provide a first-order correction for non-orthogonal resolved measurements.

2.5.5 Flexure Design

Extensive FEA iteration had shown in software that the design had a high probability of success. However, it was unknown whether the FEA simulations were, in fact, accurate. It was determined that an appropriate method by which the FEA could be confirmed was through the construction of a bench level prototype, which will be detailed in Section 3.1.

2.6 Summary

This chapter has reviewed the approach to developing a robust design that meets the performance characteristics specified. The *FRDPARRC* approach utilized uncovered many potential issues before any physical implementations were realized, helping to expedite development and reduce costs. With a design in place, a bench-level prototype was built to test the design decisions that were made. From here, further improvements were made and a revised sensor was built.

Chapter 3

Prototype and Revised Sensor

"Mens et Manus"

– MIT's motto meaning "Mind and Hand"

The design of any physical product starts with a prototype. Prototype, from the Greek πρότος meaning "first" and τύπος meaning "form", is quite literally the first (or at least early) form of a device. Prototypes allow devices to be evaluated without simplifying models or assumptions and provide the first tangible insight to the benefits and drawbacks of a design. The design can then be iterated upon. This chapter will focus on fabrication of the bench-level prototype, redesign of the device given insight gained from the prototype, and finally fabrication of the revised force sensor design.

3.1 Bench-Level Prototype

The bench level prototype allowed for the design decisions detailed in Chapter 2 to be experimentally tested. Positive characteristics would be retained whereas suboptimal characteristics would be revised for the next version.
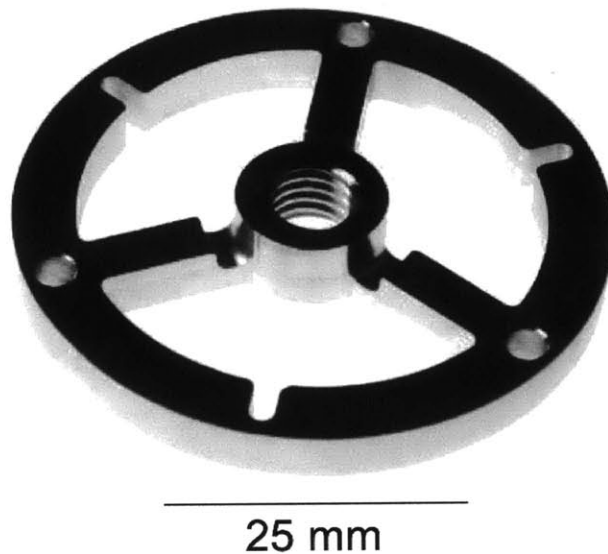
71

25 mm

Figure 3-1: This image shows the fully manufactured 7075-T6 aluminum prototype flexure system.

3.1.1 Flexure

The flexure geometry that met specifications in FEA needed to be realized in the specified material, 7075-T6 aluminum alloy. A HAAS VF-0E machining center [46] was used to create the part out of precision ground plate. Figure 3-1 shows the final part. Slots, which interfaced with pins in the adapter, were cut in the outer ring to ensure alignment.

3.1.2 Adapter

The adapter which connected the force sensor to the actuator housing and was also machined on a HAAS VF-0E [46] from 6061-T6 aluminum alloy. Because not all features could be machined in one setup, the features accessible from the top were machined first to achieve good surface finish and dimensional accuracy to interface with the force sensor. The stock was then flipped and the geometry for interfacing with the actuator housing was machined. The mounting holes around the actuator housing interface geometry were manually machined with an indexable fixture. Figure

25 mm

Figure 3-2: This image shows the prototype adapter. This part connected the flexure system to the actuator housing.

3-2 shows the final part.

3.1.3 Surface Preparation and Gauge Mounting

Surface preparation prior to mounting strain gauges was critical for proper adhesion. The following procedure was adapted from [45] and proved to be appropriate for this application. The preparation steps included:

1. Clean area with degreaser (in this case, citrus degreaser was used) and wipe with an absorbent towelette.

2. Rinse with distilled water, let air dry.

3. Lightly sand with 400 grit sandpaper in small circular motions.

4. Rinse with distilled water, let air dry.

Once the surface received this preparation, gauge mounting could commence. This included:
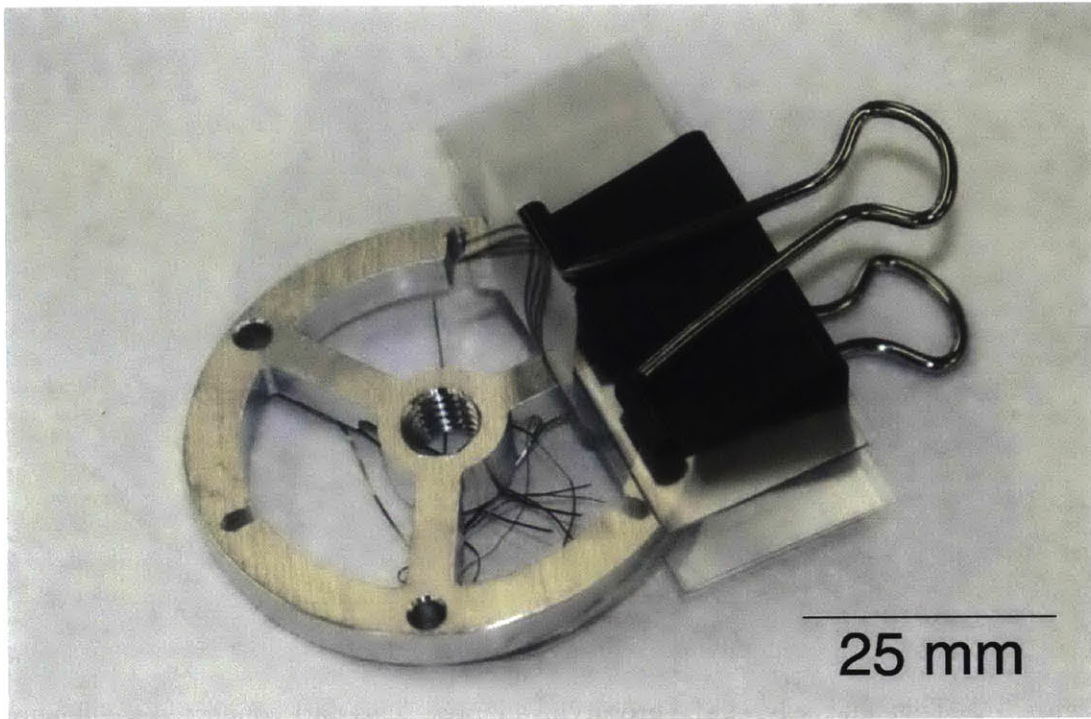
Figure 3-3: This image shows step five of the gauge mounting procedure, where pressure is applied for 10 minutes using a binder clip over a plastic shim.

1. Lay gauge at desired location.

2. Cover with transparent tape to set location.

3. Reposition as needed.

4. Peel back tape and place 1 small drop of cyanoacrylate (Loctite® 498) on gauge back.

5. Apply distributed pressure for 10 minutes (in this case, using medium binder clip and plastic shim for force distribution, as shown in Figure 3-3).

6. Peel back tape on itself, remove any residual cyanoacrylate

This procedure (both surface preparation and gauge mounting) resulted in a very reliable installation of the gauges on the aluminum flexure. Figure 3-4 shows an attached gauge as well as strain relief pad (for which the same procedure was used).
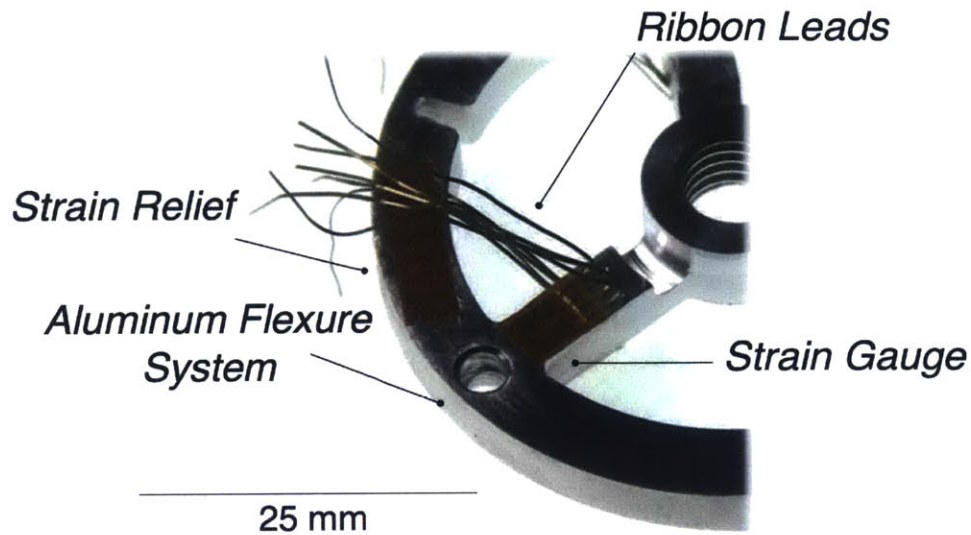
Figure 3-4: This image shows a dual-grid strain gauge and strain relief pad mounted on the top surface for one flexure. The ribbon leads, which were pre-soldered on this strain gauge package, extend up away from the gauge awaiting insulation and final soldering.

3.1.4 Strain Relief

As shown in Figure 3-4, a strain relief pad was integrated to limit spurious strains (induced by movement of the instrument cables) from being measured by the strain gauges. OMEGA® BPT-2 strain relief pads [32], 8 terminals long, were fixed using the procedure described in Subsection 3.1.3. The electrical connections from the gauges could be anchored to these terminals, allowing for a stable mechanical connection through which the signals would be passed to the data acquisition (DAQ) system.

3.1.5 Assembly

With all the gauges and strain relief pads mounted, the ribbon wires from the gauges were fitted with polyamide insulation tubing and soldered to the strain relief terminals, along with the appropriate wires leading to the DAQ system. The strain relief pads were then encapsulated with UV cure epoxy to prohibit accidental shorts and ensure maximum mechanical stability. The fully instrumented flexure system is shown in Figure 3-5.

OMEGA® BPT-2
(w/ Epoxy
Encapsulation)

OMEGA® SGD-3/350-DY11

Polyamide
Insulation

25 mm
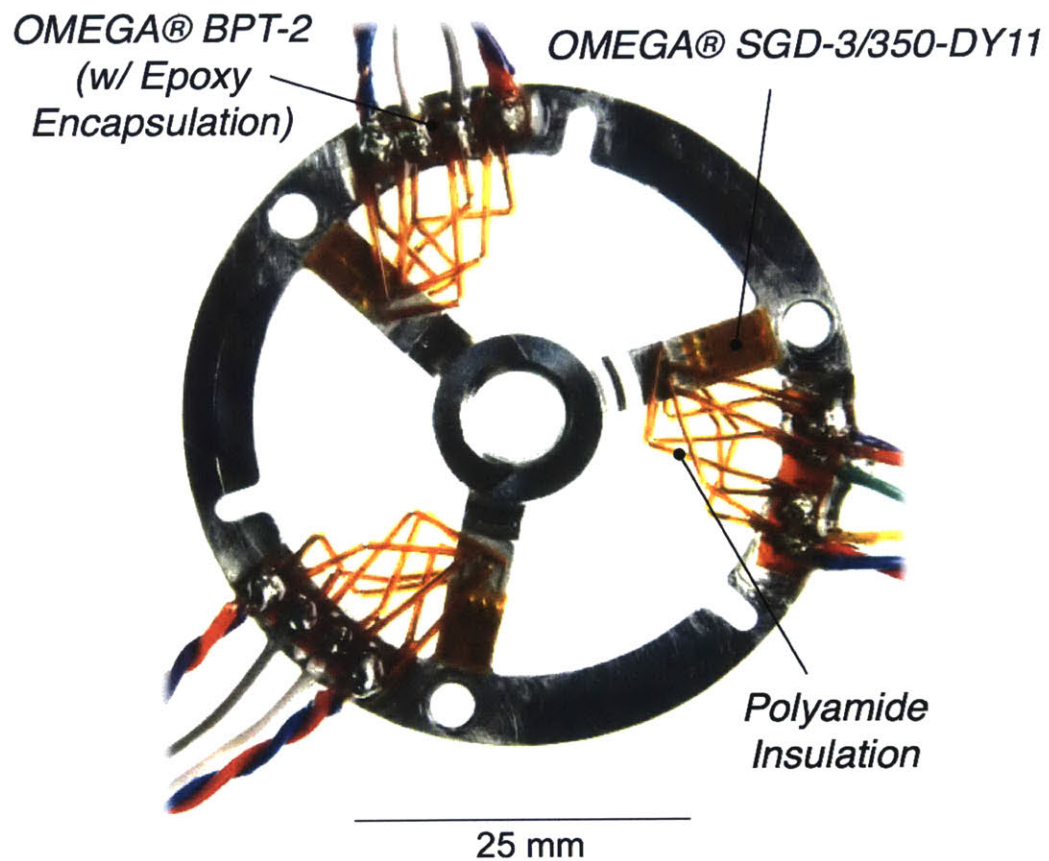
Figure 3-5: This top view shows the fully instrumented prototype sensor, complete with mounted gauges (OMEGA® SGD-3/350-DY11 [32]) and electrical connections. The ribbon leads extending from the gauges are shrouded in polyamide tubing insulation to eliminate the risk of a short circuit. OMEGA® BPT-2 [32] with UV-cure epoxy encapsulation act as the strain relief points should any undue strain be placed on the instrument through movement of the cables.

When the flexure system was fully assembled, constraint pins mounted in the adapter (shown in Figure 3-2) reliably aligned these two parts, ensuring the ampoule central axis and actuator central axis were coincident. The M2.5 screws were then tightened to mate the flexure system to the adapter. The full assembly is shown in Figure 3-6.

3.1.6 DAQ System

For preliminary testing, an NI Compact DAQ 9188 with a simultaneous bridge module 9237 [28] was used and could interface with custom LabVIEW® software [28]. The software could be developed with the cDAQ 9188 and then easily integrated on the BioInstrumentation Lab's JI for human injections (Human JI) which utilized an NI Compact RIO (Reconfigurable I/O) 9024 [28]. This Human JI was where the sensor needed to be integrated.

The strain gauge module 9237 has four simultaneous 24-bit analog to digital converters as well as integrated power supply and sensing circuitry with compatibility on both the cDAQ 9188 and cRIO 9024 systems [28]. It could therefore measure four bridges simultaneously (this application only needed three) and had a maximum sample rate of 50 kS/s/ch making it possible to perform dynamic as well as static testing on the instrument to confirm performance characteristics.

3.1.7 Software

Custom LabVIEW® software [28] was written and allowed for monitoring of all three full bridge circuits, normal and lateral force visualization and measurement, DC offset zeroing, averaging routines for calibration, frequency analysis for real-time noise characterization, and recording capabilities. The front panel is shown in Figure 3-7.

3.1.8 Preliminary Qualitative Testing

Preliminary testing with the hardware and software indicated a number of positive performance characteristics. First, normal sensitivity was qualitatively probed and
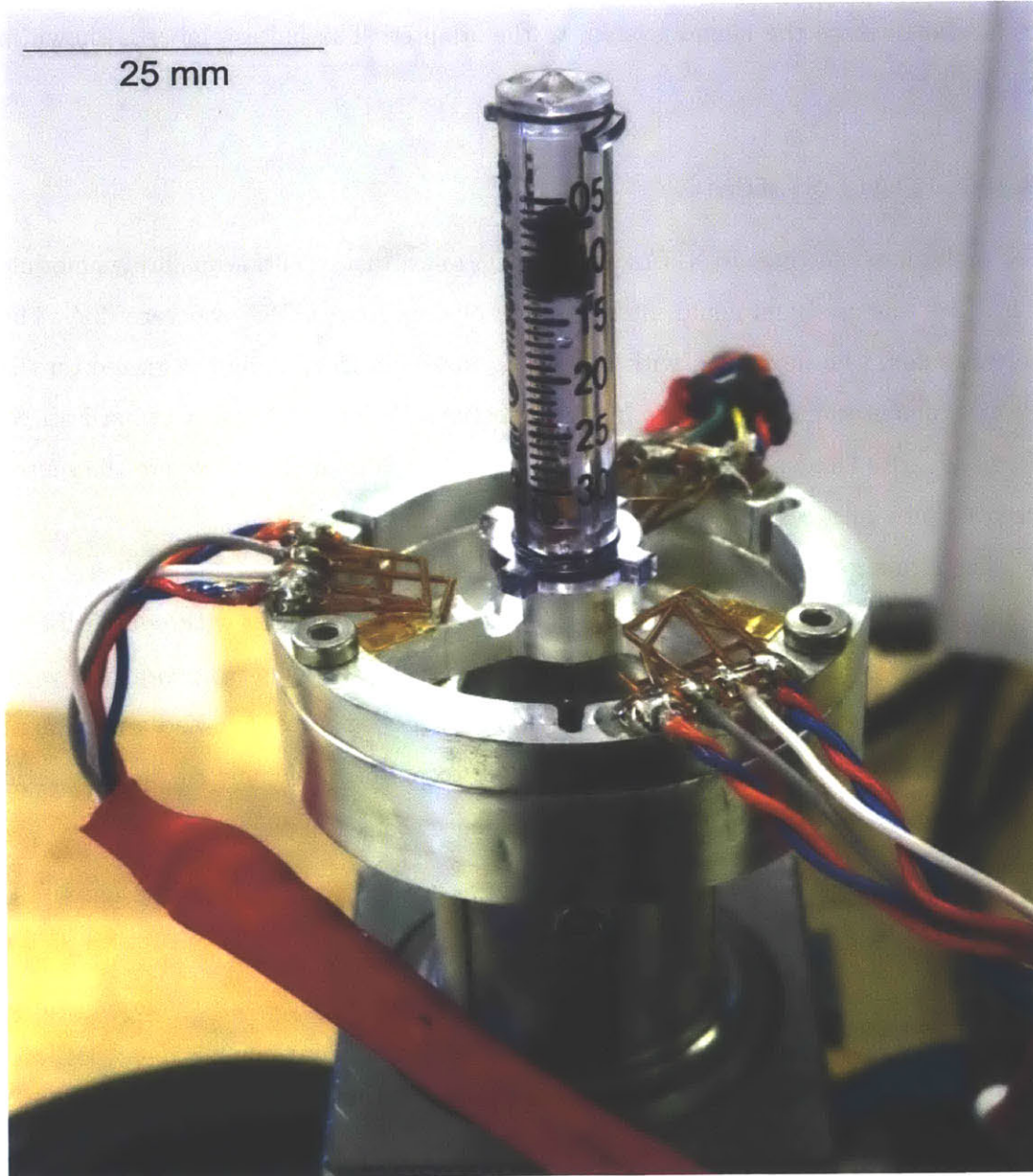
Figure 3-6: This view shows the fully instrumented prototype sensor mounted on the adapter with ampoule installed.
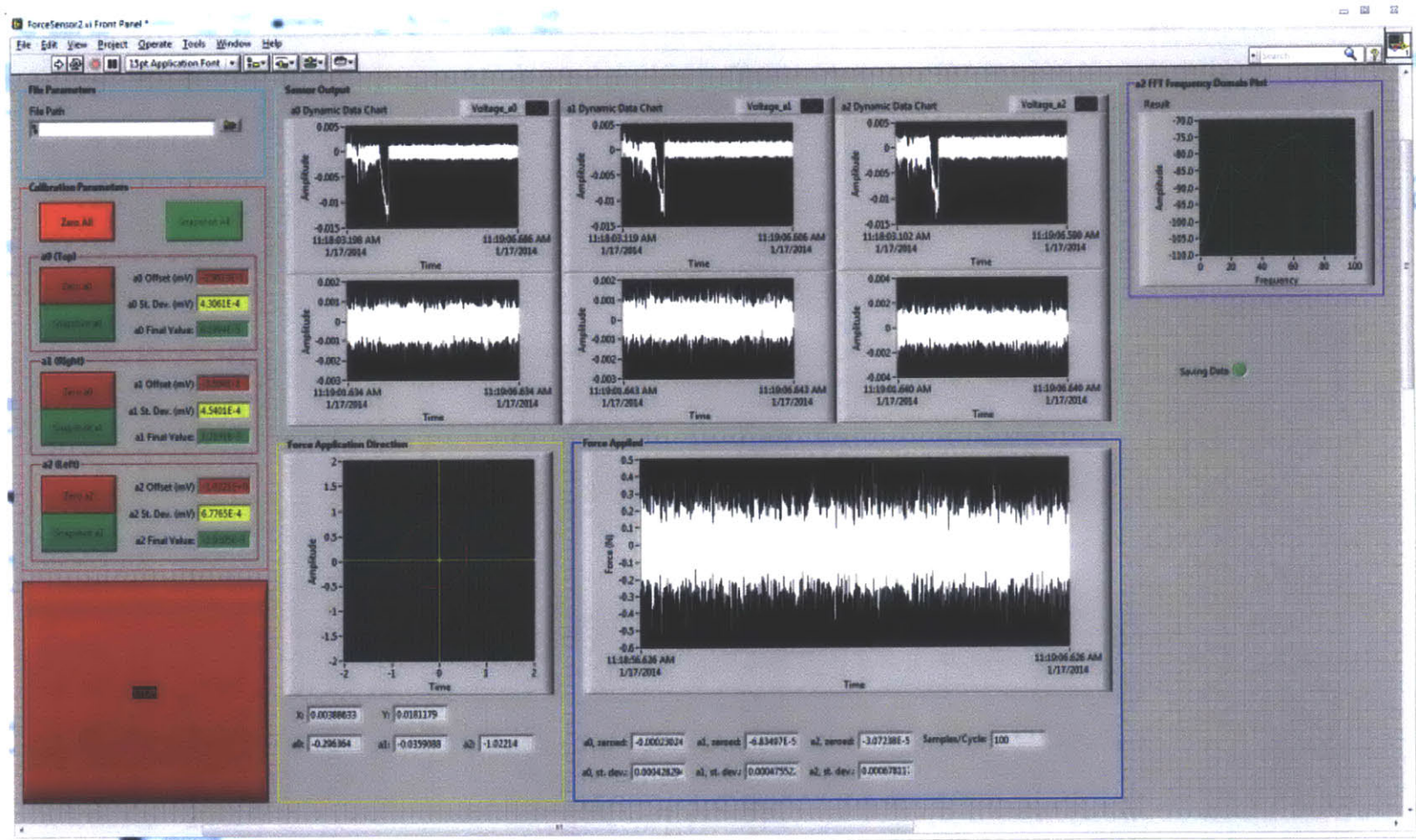
Figure 3-7: This LabVIEW® [28] front panel allowed for monitoring and measurement with the force sensor. Voltage monitoring on all three full bridge circuits is outlined in green. Normal and lateral force visualization and measurement fall within the blue and yellow outlines respectively. DC offset zeroing and averaging routines for calibration are outlined in red and frequency analysis for real-time noise characterization is outlined in purple. Turquoise outlines the path to which data files would be saved.

indicated that the instrument would be able attain far better than 0.5 N resolution once calibrated. Second, lateral sensitivity was also qualitatively probed and appeared to resolve forces quite well. These scenarios are shown in Figure 3-8.

3.2   Revised Force Sensor

While the prototype served its purpose in evaluating key design decisions, it was not ready for use on the Human JI due to a number of shortcomings. These shortcomings were identified, as were the design improvements, to make the next revision (the revised force sensor) ready for use on the Human JI.

3.2.1   Prototype Shortcomings and Additional Requirements

After experimentation with the prototype setup, a number of shortcomings were apparent. First, bulky cables currently utilized on the prototype as indicated in Figure 3-9, would prove problematic from a usability perspective if directly implemented on the Human JI. Therefore, cable management between the sensor and connector locations (as shown in Figure 3-10) was critical in the redesign. Second, the strain relief features proved inadequate in blocking measurement errors caused by cable movement. A more rigid, robust solution was necessary so that measurements were accurate once calibration was completed. Third, a piston interfacing mechanism designed by Michael Nawrot [47] and shown in Figure 3-11 had been implemented on the Human JI and was mounted at the location where the adapter would be mounted. Since this mechanism was critical to maintaining sterility and was required for any human injections, integration of this mechanism with the force sensor needed to be completed in the redesign. Last, the bench-level prototype's circuit elements were completely exposed. A cover and splashguard were required to protect the instrument from damage as well as contamination by biological fluids.
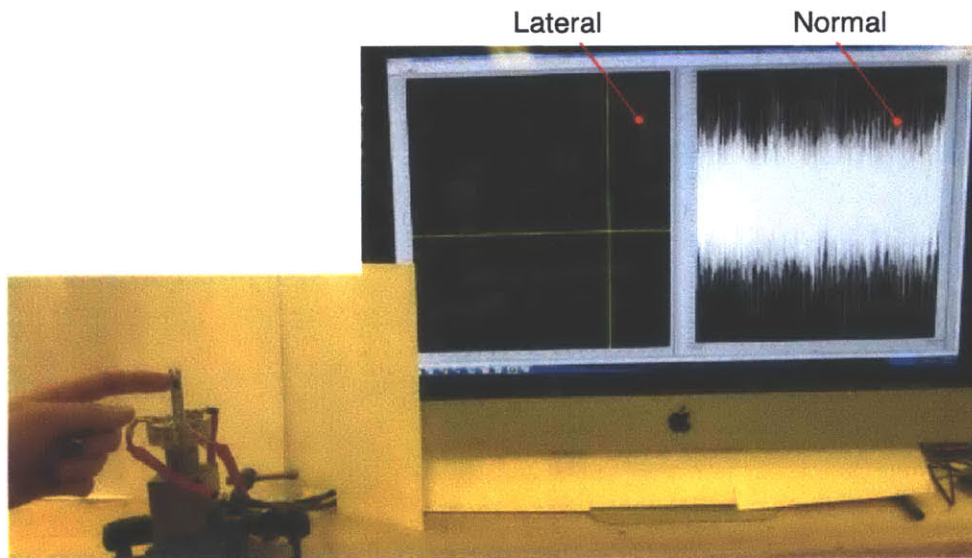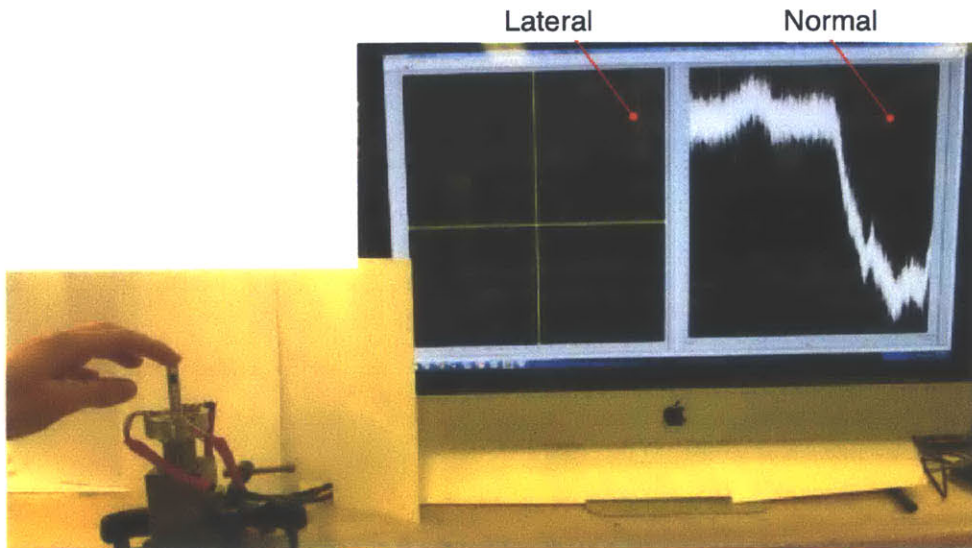
Figure 3-8: These photos show the prototype device in the left and lateral and normal force displays on the monitor to the right. (*Top*) Normal force is applied to the nozzle. Minimal lateral forces are measured, as expected. (*Bottom*) Lateral force is applied to the nozzle. Minimal normal forces are measured, as expected.
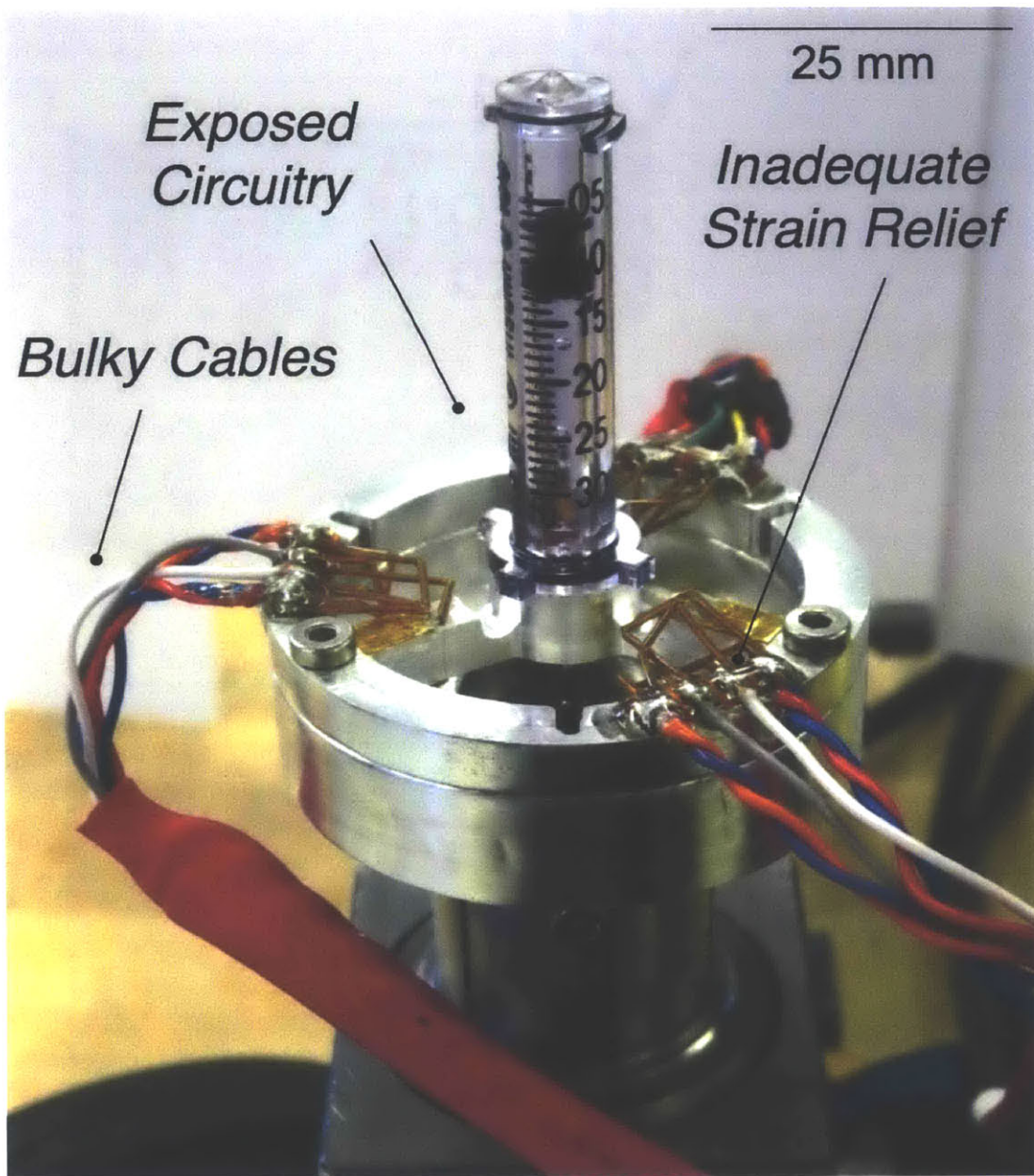
Figure 3-9: This annotated version of Figure 3-6 indicates key issues with the proto-type, along with the required improvements detailed in Figure 3-11 and Figure 3-10. The bulky cables shown here were not appropriate for the Human JI. Additionally, the strain relief features utilized on the prototype were not adequate in shielding the instrument from spurious measurements caused by cable movement. Lastly, the delicate exposed circuit elements needed to be protected.
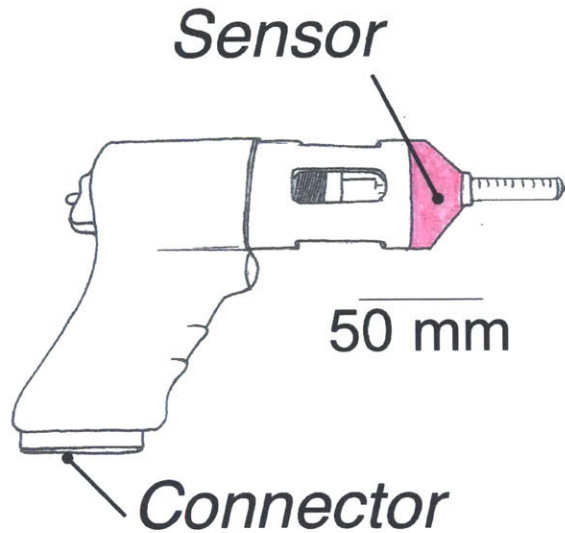
Figure 3-10: This illustration shows where the instrument signals originate on the Human JI (at the Sensor) and where the electrical connections are currently made (at the Connector). Proper management of the signal cables between these two sites was critical in redesigning the sensor to be robust for the Human JI.
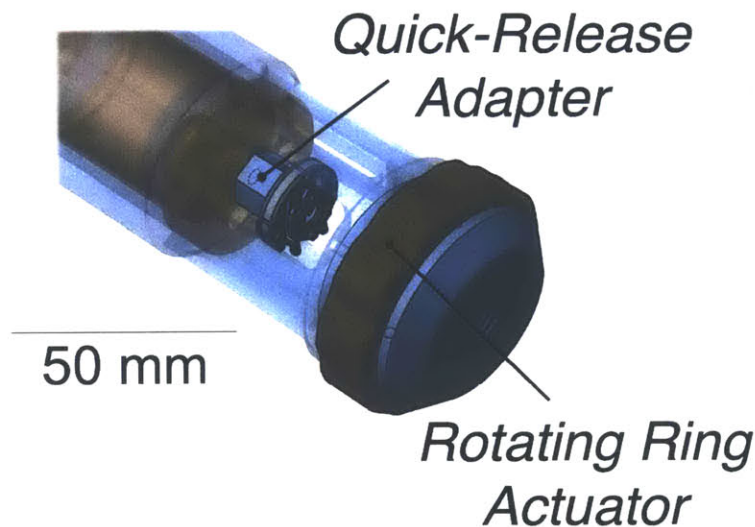
Figure 3-11: This CAD model shows the quick-release adapter and rotating ring actuator, developed by Michael Nawrot and presented in his Master's Thesis [47]. A successful redesign of the force sensor would incorporate provisions for the rotating ring actuator (shown here) in the adapter. Additionally, the redesign needed to maintain geometric offsets achieved in Nawrot's design to ensure that the piston would bottom out in the ampoule and expel all drug if desired. Reproduced from [47].

3.2.2 New Design

The shortcomings, identified in the bench-level prototype, led to the generation of important new functional requirements. These new requirements were used to guide the redesign of the sensor. The final design of the revised force sensor, shown in CAD in Figure 3-12, provides design features to improve upon all of the shortcomings identified. Provisions for routing slender ribbon cables avoided the need for mounting bulky signal cables directly to the sensor, making the assembly more compact and robust. A strain relief PCB gave a much more substantial anchor (as compared to the strain relief terminal pads and epoxy encapsulation on the bench-level prototype) to which the electrical connections from the strain gauges could be connected to the signal cables. The rotating ring actuator mechanism for opening and locking the quick-release adapter was integrated with the adapter and clearance for the quick-release adapter within the adapter was provided. A cover was added to protect the instrument from damage. Last, a splashguard was designed which mounted on the ampoule to protect the device from biological contamination.

Improved Cable Management

Ribbon cables (as those shown in Figure 3-13 and originally introduced in Subsection 2.5.1) were an excellent option that allowed for low-profile routing of the signal lines on the device from the sensor location to the connection location (shown in Figure 3-10). These ribbon cables could easily be folded and routed through the adapter and along the actuator, facilitating easy installation. Commercially available surface mount connectors allowed for removable connections to be made which could be easily disassembled if required during debugging and final assembly.

A conversion board was used to transfer the signals from the ribbon cables to mini HDMI in the handle of the device. The handle cover was modified to accept a custom PCB over a number of iterations and is shown in Figure 3-14.

Cover

Routing for Ribbon Cables

Strain Relief PCB

Force Sensor
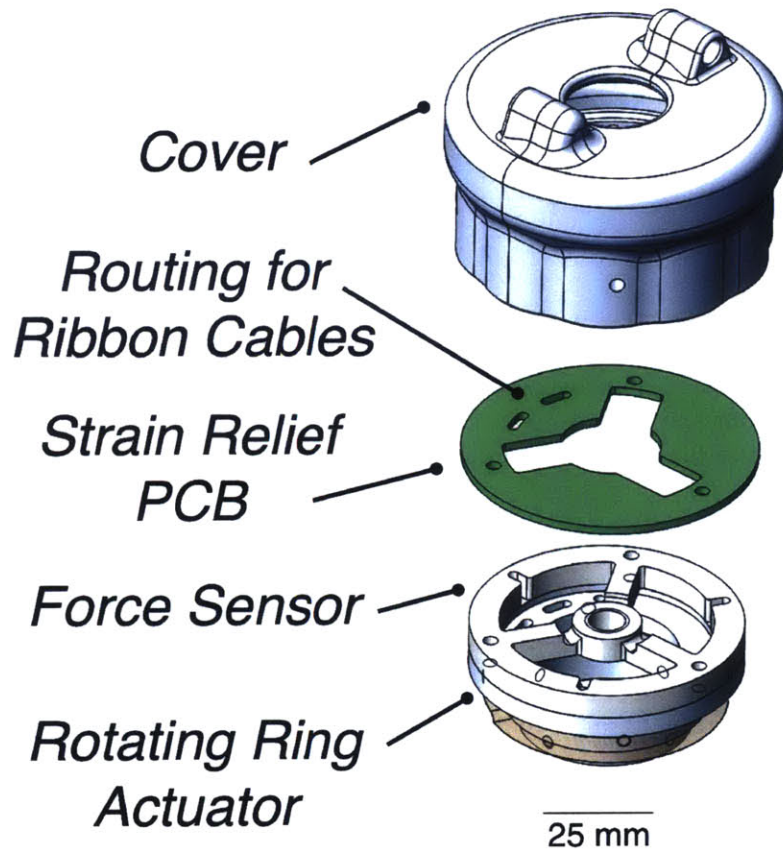
Rotating Ring Actuator

25 mm

Figure 3-12: This CAD model shows the design of the revised force sensor with provisions to meet the new functional requirements specified in Subsection 3.2.1. Routing paths for slender ribbon cables through the sensor and HDMI cables to the DAQ (not shown) allowed this iteration to avoid bulky cables. A strain relief PCB provided a substantial anchor to which the electrical connections could be mounted. The rotating ring actuator mechanism for opening and locking the quick-release adapter was integrated into the adapter, and clearance for the quick-release adapter within the adapter was provided. Last, a cover was added which protected the instrument from damage. Not shown in this figure (but shown in Figure 3-20) is the splashguard, which was mounted on the ampoule and helped protect the instrument from biological contamination.
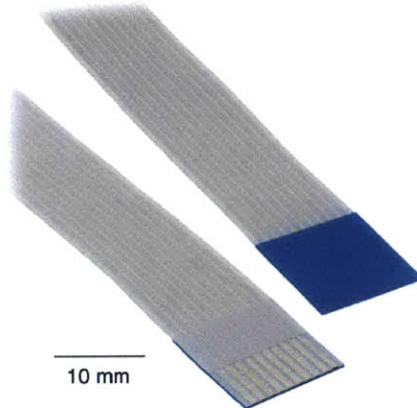
Figure 3-13: This image shows ribbon cables used in place of the bulky cables found on the prototype. These ribbon cables could be folded and routed through the adapter and along the actuator housing, allowing for a very low-profile installation. Commercially available surface mount connectors allowed for non-permanent signal connections to be made. This greatly aided in assembly and debugging. Reproduced from [48].

Improved Strain Relief

Another custom PCB, mounted on the front of the flexure system, served as a robust and mechanically stable strain relief mechanism. This design outperformed the strain relief terminal pads with epoxy encapsulation used in the prototype and was very immune to measurement inaccuracies induced by cable motion. The strain relief PCB is shown in various steps of assembly in Figure 3-15. In this redesign, the pre-wired gauges were exchanged for unwired gauges with terminals (OMEGA® SGD-3/350-DY41 [32]). 28 AWG Soderon® copper magnet wire MW0064 [49] was soldered to the gauge terminals. This wire was then carefully routed to the appropriate pads on the PCB. On the PCB, the electrical connections from the strain gauges to the signal cables were made.

The Soderon® magnet wire [49] was particularly convenient for this application. Instead of requiring that the ends be stripped with sandpaper (as with typical magnet wire), the insulation on this wire melts above 155 °C, which was easily attained by short contact with a soldering iron [49].

Figure 3-16 shows the assembly for a bridge located on the upper surface of the

Rev 0

Rev 1

Rev 2

50 mm

50 mm

Handle PCB

Strain Relief
Feature

Rev 3
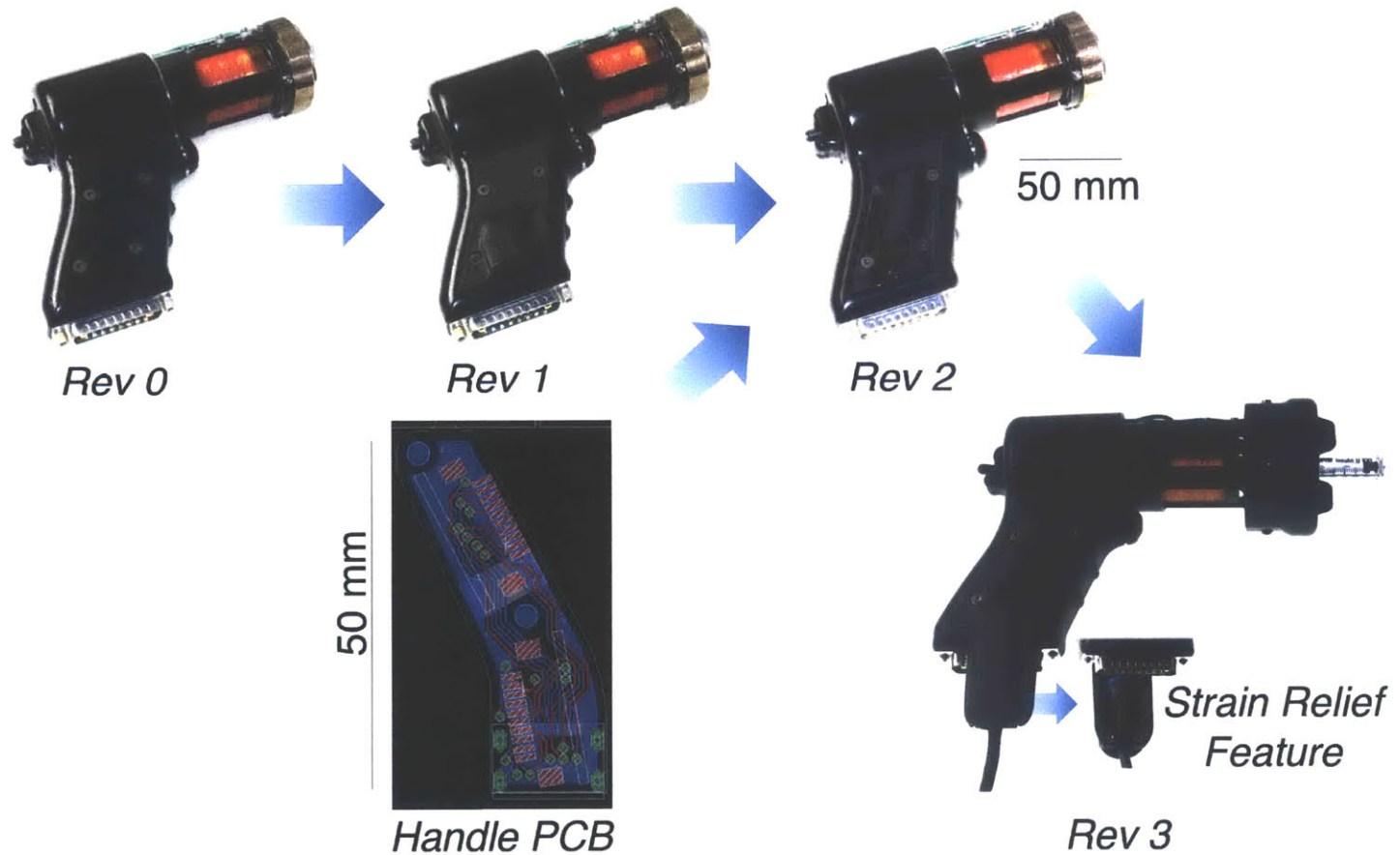
Figure 3-14: This sequence of images shows the evolution of the handle connector, where signals were transferred from ribbon cables to a more robust HDMI cable that could withstand repeated movements and bending. Rev 0 is the unaltered handle with no provisions to connect the force sensor. Rev 1 shows a preliminary 3D printed mockup with port for connection. Once the handle PCB was designed, the cover was modified to house it, as shown in Rev 2. Finally, Rev 3 included a bending relief feature for the HDMI cable to ensure proper connectivity under moderate cable load.

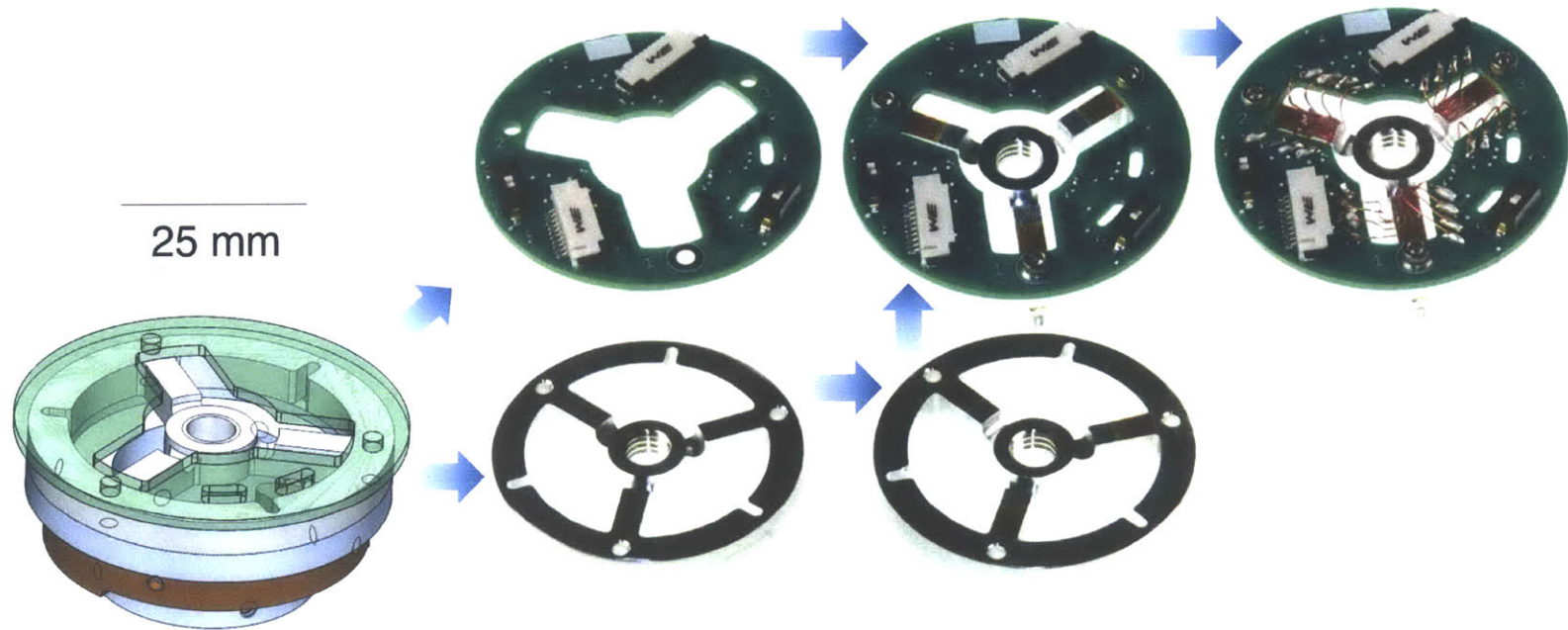Figure 3-15: This image shows the components and steps required to build the revised sensor. The sensor included the strain relief PCB and flexure system. Once the PCB was populated and the gauges mounted on the flexure system, the two components could be connected electrically and mechanically.
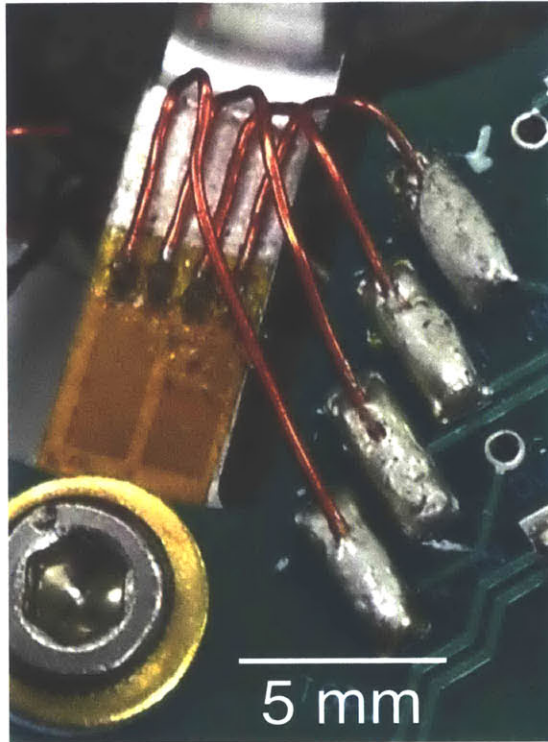
Figure 3-16: This image shows a closeup of the electrical connections to one bridge. 28 AWG Soderon® copper magnet wire MW0064 [49] connects the gauge pads to the strain relief PCB. Signals are then transferred to the ribbon cables elsewhere on the PCB.

flexure system. Similar wiring connected the bridges at the bottom of each flexure to the strain relief PCB.

Quick-Release and Rotating Ring Actuator Integration

The rotating ring actuator mechanism for opening and locking the quick-release adapter was integrated with the force sensor adapter. The same underlying mechanism and geometry for actuation and return as the original design [47] were employed. Clearance and offset for the quick-release adapter within the adapter were provided which matched clearances and offsets found in the original rotating ring actuator assembly [47]. Provisions originally in the prototype to align and fix the flexure system to the front of the adapter were added to the new adapter. The modified rotating ring actuator mounted on the new force sensor adapter is shown in Figure 3-17.
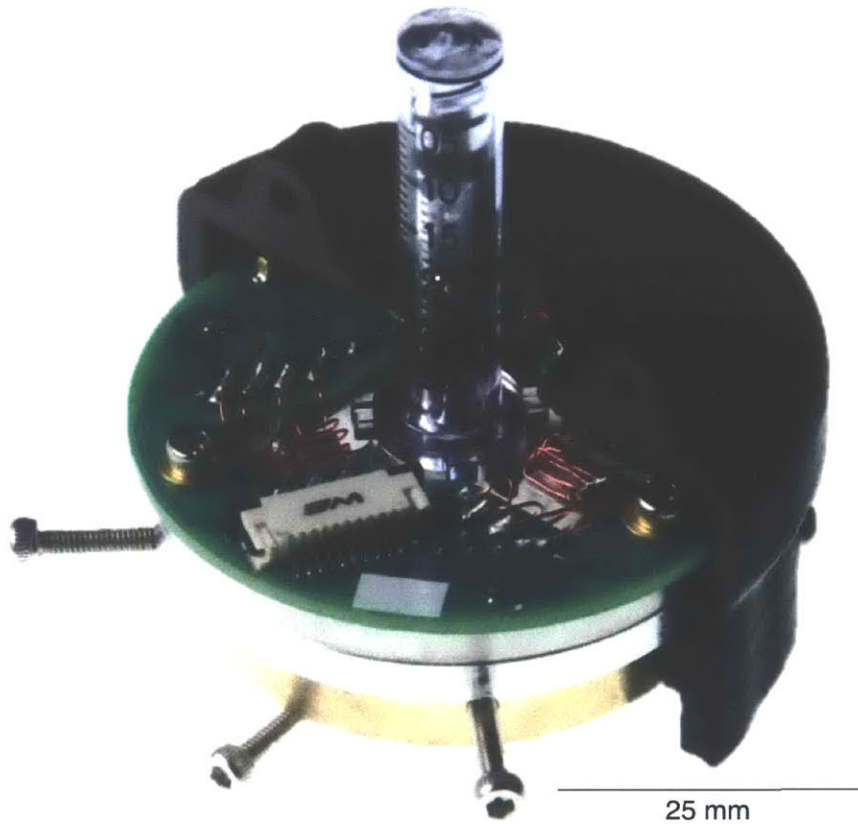
Figure 3-17: This image shows the partially assembled force sensor, complete with a fully functional modified rotating ring actuator. The rotating ring actuator made up all the parts underneath and including the brass ring. The actuation surface through which the user opened and locked the quick-release adapter is the black 3D printed plastic component, which rotated with the brass ring.
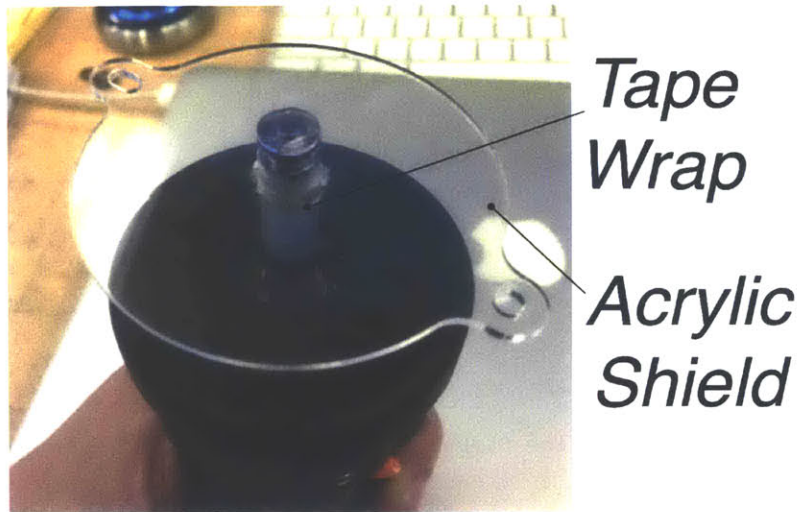
Figure 3-18: This image shows a preliminary concept for the splashguard. A laser machined piece of 3 mm thick acrylic was pushed onto the ampoule over a section wrapped with tape to hold it in place. While not practical to use on human subjects, this was the basic idea used in the final design.

Cover and Splashguard

Due to space constraints, the cover acted as the actuation surface through which the user opened and locked the quick-release adapter. This cover is shown in white in Figure 3-12 and black in Figure 3-17. The part, as shown in Figure 3-17, was manufactured with a fused deposition modeling (FDM) MakerBot® Replicator 2 [50] 3D printer in polylactic acid (PLA).

While this cover was effective at preventing damage to the instrument, it required a relatively large opening at the front to allow for the ampoule's rear flange to be inserted. This opening could allow biological fluids to contaminate the force sensor and, as such, a splashguard was needed to protect the instrument.

A very preliminary splashguard concept is shown in Figure 3-18 and consisted of a laser machined piece of 3 mm thick acrylic pushed onto the ampoule. Flexures were added to the central hole which grabbed the ampoule to hold the splashguard in place. The material was changed to 0.79 mm thick acetal. Acetal can maintain its structural integrity at autoclave temperatures of 130 °C, given its maximum intermittent service temperature of 148.8 °C [51], and is very easy to laser machine.
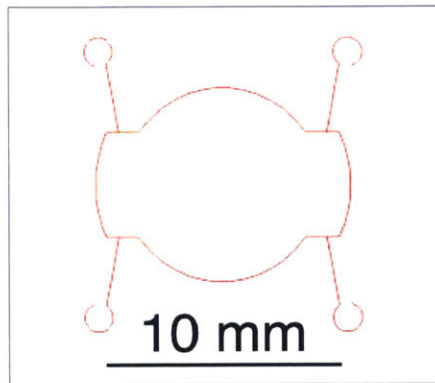
91

Figure 3-19: This figure shows the ninth and final revision on the flexure design. The red lines would be cut through the acetal sheet with a laser cutter to create the flexures. The cutouts on either side accept the male luer lock features formed in the sides of the ampoule near the nozzle.

The flexure geometry was modified several times to achieve an appropriate stiffness while maximizing the area covered by the splashguard. The final flexure geometry is shown in CAD in Figure 3-19 and on the final part in Figure 3-20 on the right. Several were made like the one shown in Figure 3-20 on the left. This allowed many to be autoclaved at once. These could be then used once on a human subject before needing autoclaving again. Autoclave cycles did not appear to degrade structural performance of the splashguard.

Software

The LabVIEW® code [28] used on the prototype was improved and merged with the pre-existing Human JI LabVIEW® software on the cRIO 9024 [28]. The code was modified so that readings from the force sensor could be recorded starting 10 ms before an injection and during its duration in conjunction with voltage and position data already being recorded. Real-time lateral and normal force application data were presented to the user graphically to help achieve a particular contact force before injection. An offset compensator was included to allow the user to remove any DC offset from the readings prior to firing the device.
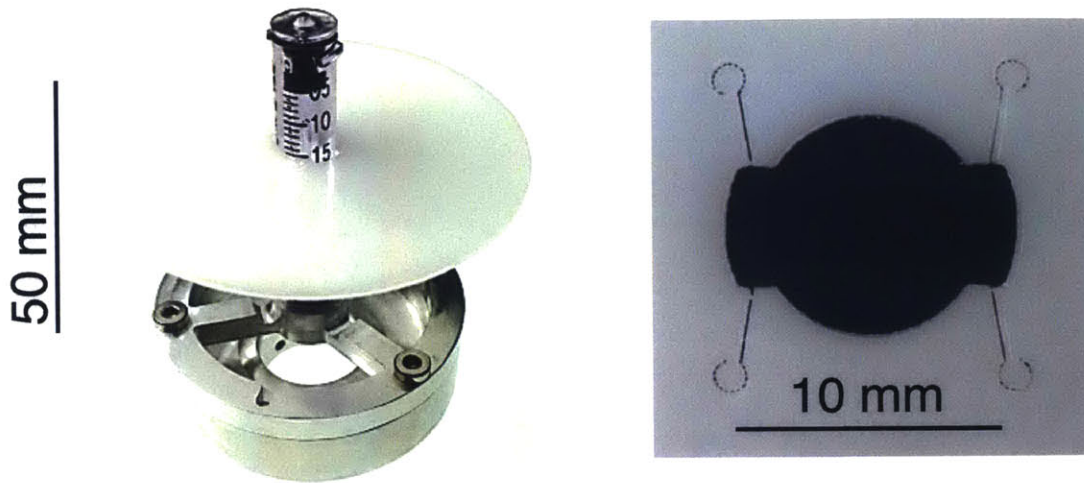
Figure 3-20: This figure shows the final flexure. (*Left*) The splashguard, mounted on an ampoule atop an unfinished force sensor. (*Right*) The final flexure geometry machined with a laser.

3.3 Summary

With all that was learned in construction and experimentation of the prototype, as well as with design improvements made to the revised version, a robust instrument had been brought into reality from the designs and analysis presented in Chapter 2. With fully formed instrument hardware and software, calibration and validation could now commence.

Human JI Software Interface

New Force Sensor Interface
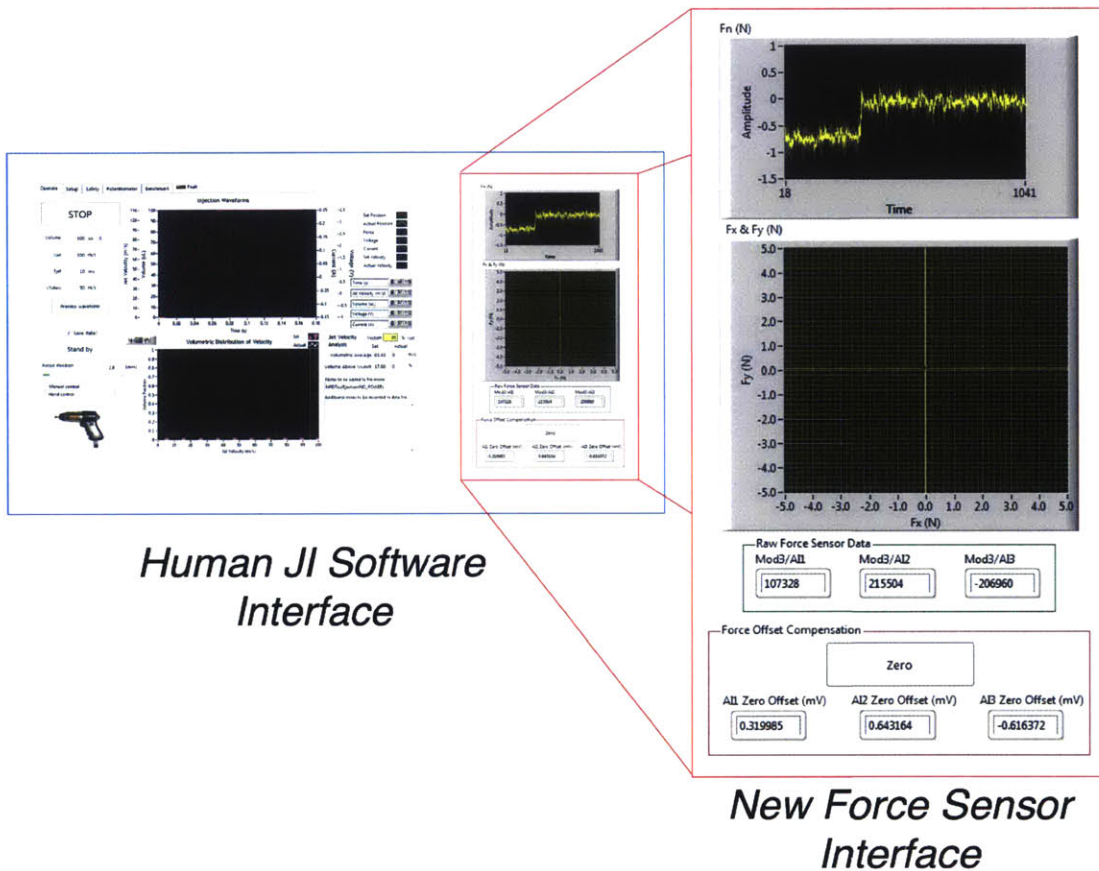
Figure 3-21: This figure shows the new force sensor interface implemented within the pre-existing Human JI LabVIEW® code [28]. Provisions to allow force sensor measurements before and during injection were built. Real time lateral and normal force application data were presented to the user graphically. An offset compensator was included to allow the user to remove any DC offset from the readings prior to making contact with the tissue in the orientation the device would be fired.

94

Chapter 4

Calibration and Validation

"Trust, but verify"

– Russian Proverb

The next step was to experimentally discover the linear and angular calibration coefficients and input them into the sensor model so that resolved force magnitudes and directions matched applied forces. Additionally, performance validation was required to confirm the device met the specified functional requirements in terms of bandwidth and induced volume error. Custom jigs were designed and fabricated to accomplish these tests.

4.1   Normal Force Calibration

First, parameters C_1, C_2, and C_3 (which together calibrated the system to output correct normal forces applied to the nozzle) needed to be experimentally determined. A calibration jig was required which could apply various normal forces to the tip of the nozzle so that a relationship between the supported load on each flexure and the resultant voltage could be found.

Figure 4-1 shows an illustration of the normal calibration jig interface with the nozzle. A vertically-mounted ampoule interfaced with the jig top via a small hole that
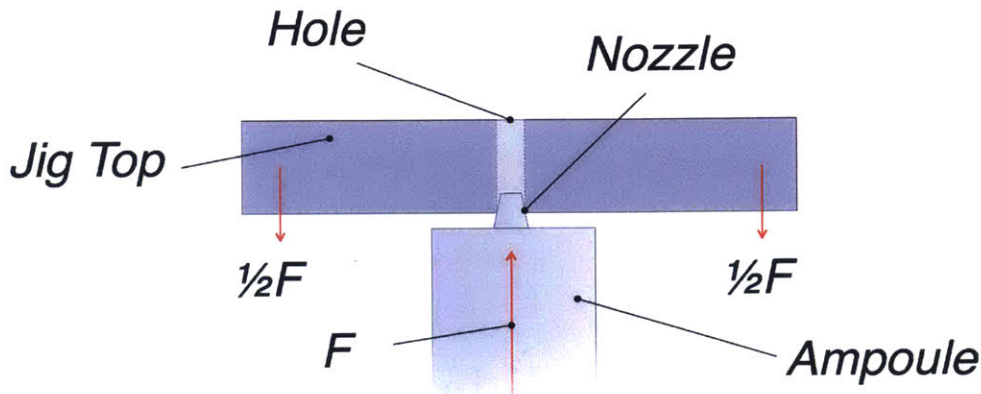
Figure 4-1: This graphic shows the method by which the normal calibration jig imparted a pure normal force to the nozzle. The ampoule, vertically mounted, interfaced with the jig top via a small hole that would sit partway up the nozzle. As such, no lateral forces were applied during normal force calibration. Various calibration weights F were suspended and a relationship was determined between the applied load and measured voltage on each of three flexures.

would sit on the nozzle. As such, no lateral forces were applied during normal force calibration. Various calibration weights F were suspended and a relationship was determined between the applied load and measured voltage on each of three flexures. Figure 4-2 shows the normal force calibration jig being used on the prototype sensor. Monofilament line allowed for the calibration weight to be connected to the jig top and suspended from below for stability.

A relationship, like the one shown in Figure 4-3 for one flexure, was found and a linear regression was fit using least squares. Similar relationships were found for the other flexures. The slopes were parameters C_1, C_2, and C_3 for the respective flexures.

Once these parameters had been inputted into the model, normal force was measured between 0 to 8 N. The average normal force error was ± 0.15 N, within the functional requirement of ± 0.25 N.
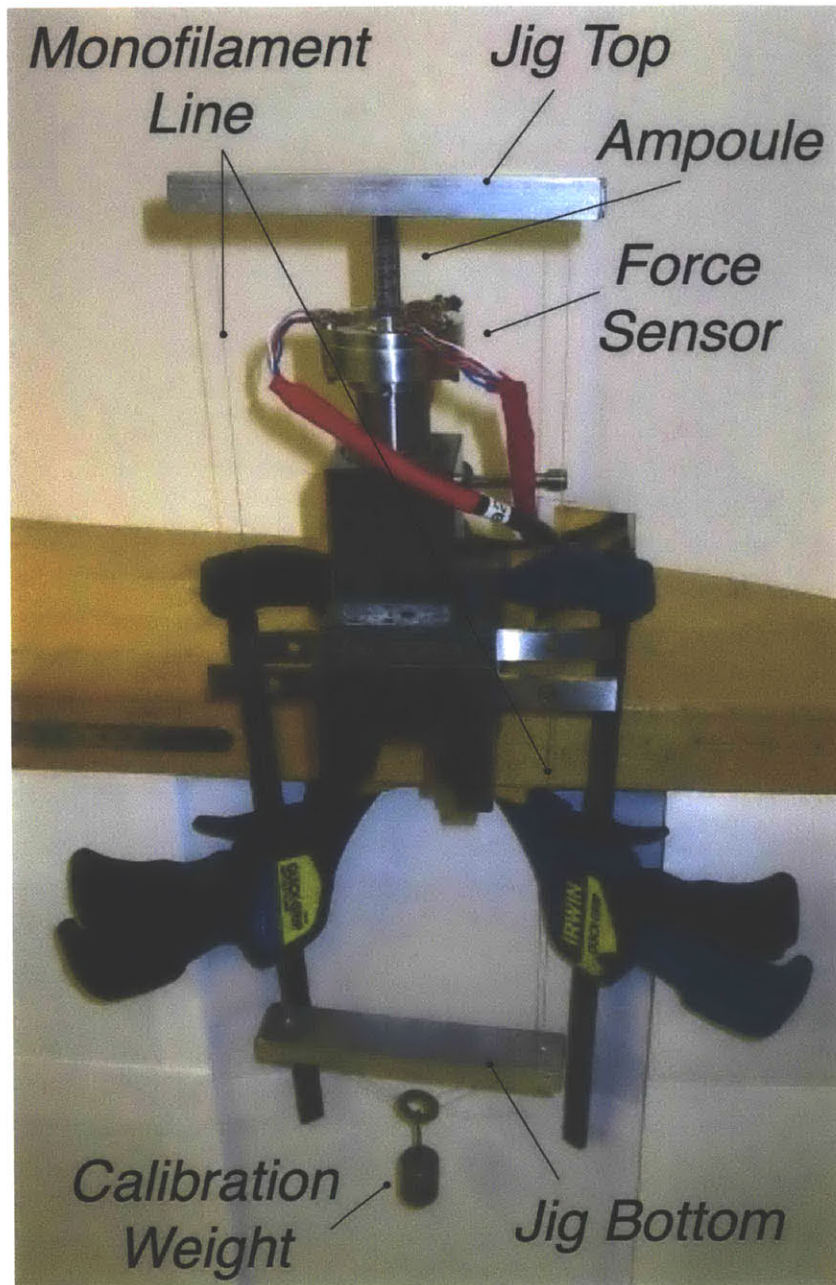
Figure 4-2: This image shows the normal calibration jig being used on the prototype sensor. Monofilament line allowed for the calibration weight to be connected to the jig top and suspended from below for stability.
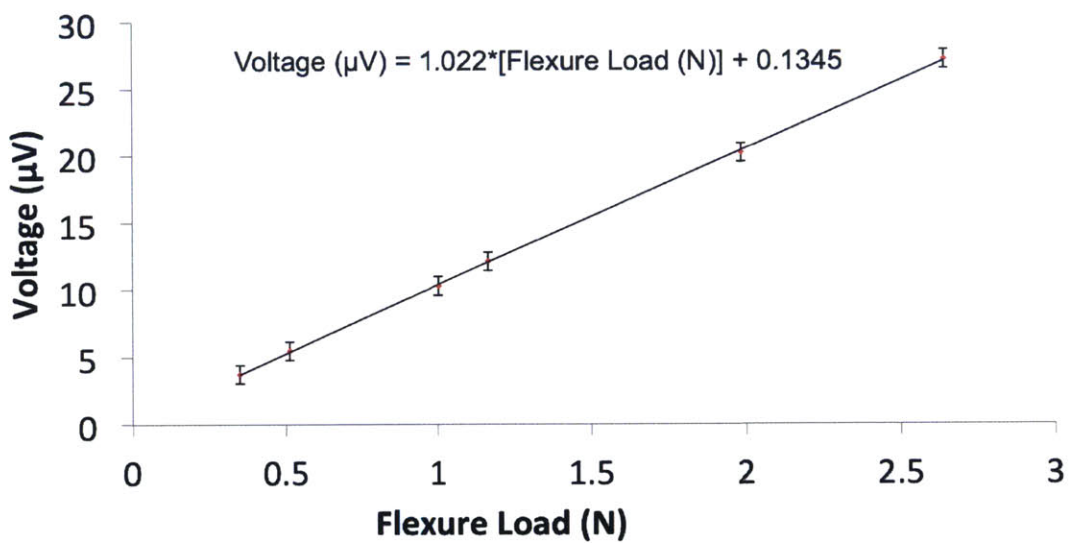
Figure 4-3: This graph shows the relationship between measured bridge voltage and load applied to the respective flexure. A linear regression was fit using least squares to the measured data. Similar plots for the other two flexure voltage versus load relationships were made. From the linear models fit to the data, parameters C_1, C_2, and C_3 were experimentally determined. Standard deviation for each measurement is shown by the error bars.

4.2 Lateral Force Calibration

Another jig was constructed to precisely impose lateral forces on the nozzle and is shown in Figure 4-4. A lateral calibrator plate consisted of an aluminum plate with pins mounted in CNC drilled holes. Monofilament line, which was anchored to the nozzle, was guided by these pins to precisely impart a particular lateral force direction. A chemistry ring stand was fitted with a pulley and was located so that the monofilament line was routed in a way that the line would lightly rest against the appropriate pin, as shown in Figure 4-4. This allowed for repeatable lateral force magnitudes and directions to be imparted on the nozzle.

The lateral force calibration jig allowed for angle parameters a and b to be experimentally found. This was accomplished by applying various pure lateral X and Y forces and measuring the resolved lateral forces. Lines were fit using least squares to the resolved force points and the angle between this line and the respective axis were measured. Parameters a and b were then inputted into the sensor model. This same data was used to find linear scaling coefficients L_x and L_y. X_{skew} and Y_{skew} were plotted against the applied load in the pure X or Y direction and a line was fit using least squares. The slopes indicated the scaling coefficient. These parameters fully characterized the lateral calibration. As shown in Figure 4-5, after skew and calibration were implemented, the experimentally measured green points fall very close to their expected location at the intersection between the radial lines, representing applied angles, and circles, representing applied magnitudes. The average lateral force magnitude error was $\pm$ 0.14 N (again within requirements of $\pm$0.25 N) and the angle error was $\pm$ 0.68°.

4.3 Bandwidth Validation

While dynamic FEA had been conducted (as discussed in Subsection 2.4.4) on the isolated flexure system with the bench-level prototype, it had not been conducted with a more complete model of the revised sensor.

99
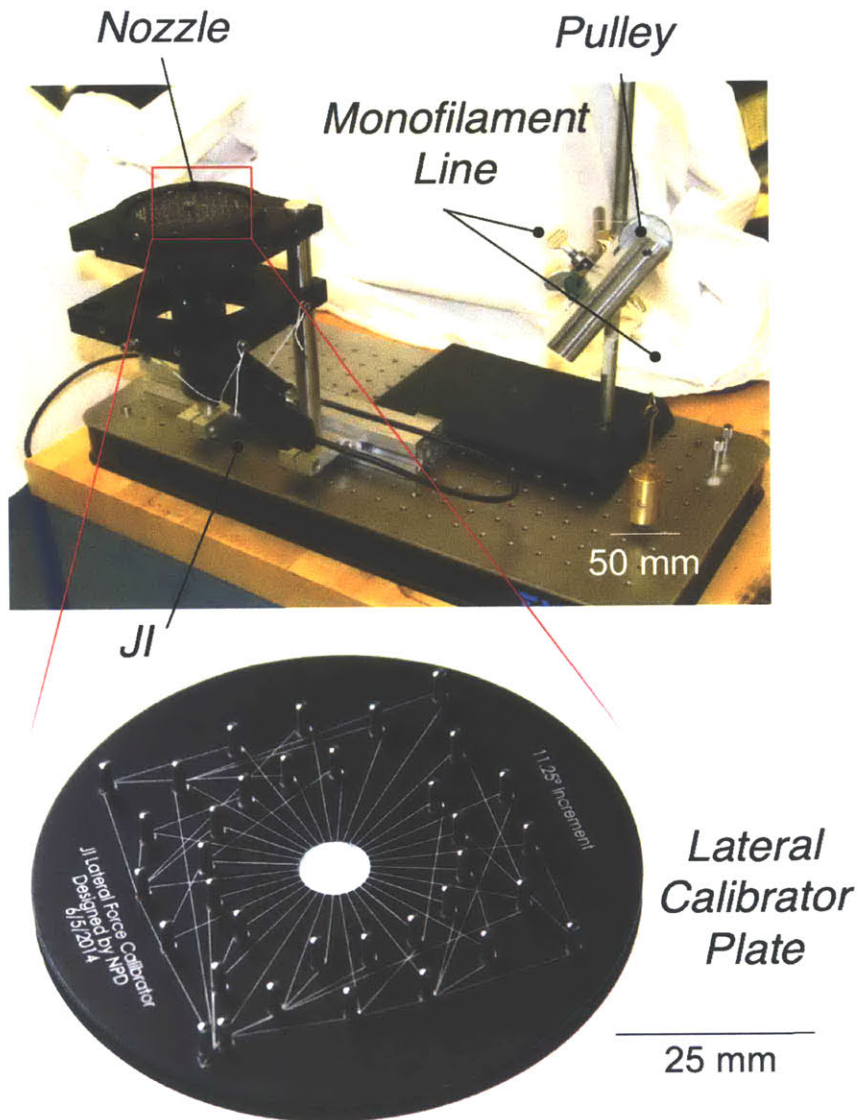
Figure 4-4: This image shows the lateral force calibration jig at the top. A lateral calibrator plate, shown at the bottom, consisted of an aluminum plate with pins mounted in CNC drilled holes. Originally, it was presumed that the monofilament line could be routed around many pins to a common location where a calibration weight could be dangled to apply a load. These paths were designated by the etched lines on the surface of the lateral calibrator plate. However, the capstan effect around many pins was too large and resulted in great difficulty in applying repeatable lateral force magnitudes. As such, a chemistry ring stand was fitted with a pulley and was located so that the monofilament line would lightly rest against the appropriate pin. This allowed for a a particular lateral force direction to be precisely imparted while also minimizing the error in magnitude application.

Figure 4-5: This plot was a validation of the lateral force calibration. The experimentally measured green points fall very close to their e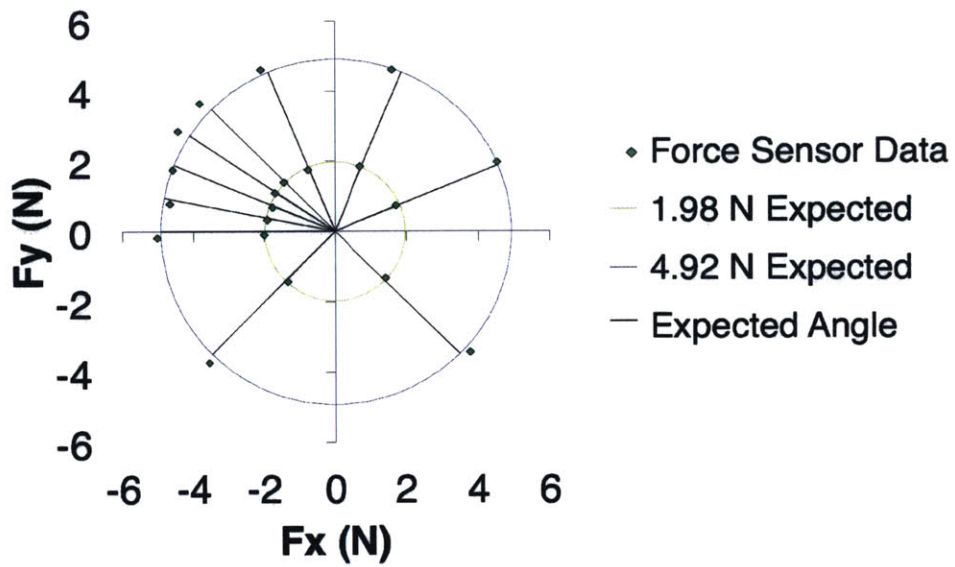xpected location at the intersection between the radial lines, representing applied angles, and circles, representing applied magnitudes.

As such, additional dynamic FEA was conducted in Solidworks® [43] with a simplified CAD model of the revised sensor and adapter, shown in Figure 4-6. The results of the dynamic FEA are shown in Table 4.1 along with the representative images of the resonant modes. The same geometry of the FEA model was constructed, also shown in Figure 4-6, and was actuated with a Thorlabs® piezostack actuator [52]. An illustration of the setup for exciting resonant modes is shown in Figure 4-7. The preload screw, present in both the FEA model and the experimental setup and shown in Figure 4-7, simulated the presence of the ampoule's mass. A sinusoid sweep was used to investigate the sensitivity at a range of frequencies. The bode plot in Figure 4-8 and coherence squared plot in Figure 4-9 show the frequency response of the structure. The resonances measured in the magnitude plot match the dynamic FEA modes moderately well. Of particular note is that the minimum resonance found experimentally was 8 kHz, which was very close to the estimate made in Subsection 2.4.4 ($\sim$8.6 kHz) and above the 5 kHz specified for a flat response.

4.4 Ejected Volume

Validating the precision and accuracy of the volume ejected from the modified device was extremely critical from a clinical perspective. The experimental setup and procedure were similar to previous methods employed [18, 47] and would determine the ejected volume variability with the addition of the force sensor and quick release mechanism. Three different ampoules (a, b, c) were tested, and each was exchanged after every ejection sequentially (a,b,c,a,b,c...) to control for ampoule and piston variability and wear [47]. Plastic tubes were filled with absorbent cotton and their initial mass was measured. Distilled water was ejected into each at different volumes and jet velocities. The final mass of the tubes after ejection was compared to the initial mass to find the total volume ejected. The results of these experiments are shown in Figure 4-10. Figure 4-10 also compares the results of the volume validation conducted with the force sensor/quick-release adapter equipped device with previous volume validations completed without the force sensor but with the quick-release

102
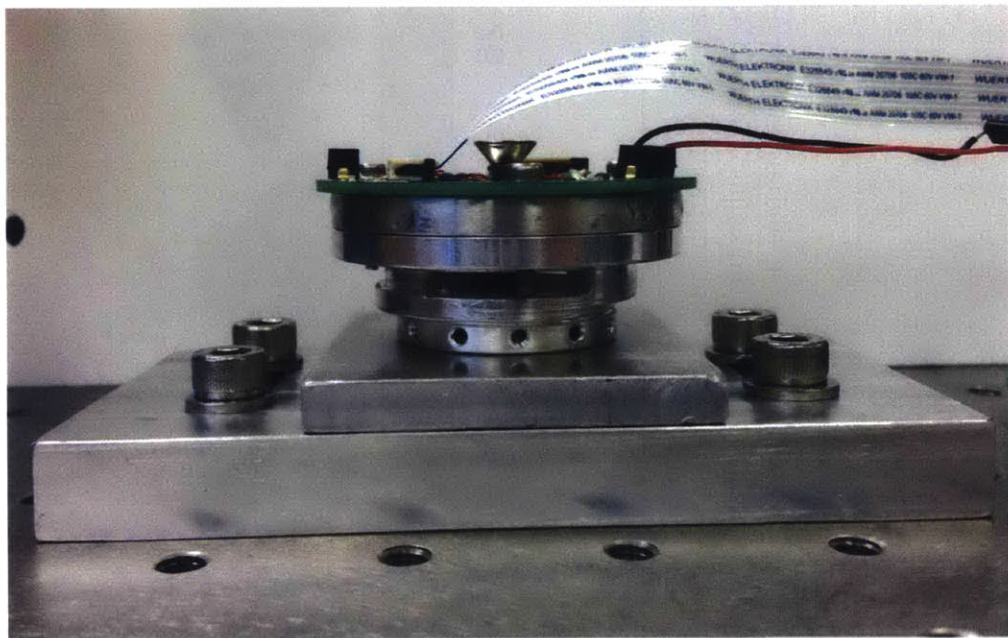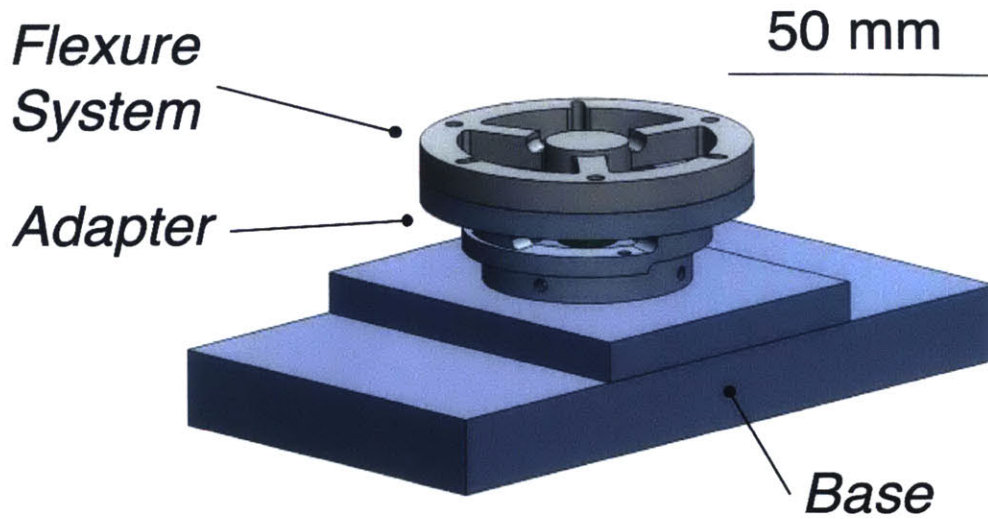
Figure 4-6: (*Top*) This CAD rendering shows the simplified geometry of the revised sensor and adapter used in dynamic FEA for final bandwidth validation. (*Bottom*) This image shows the experimental setup constructed for validating the bandwidth of the sensor.
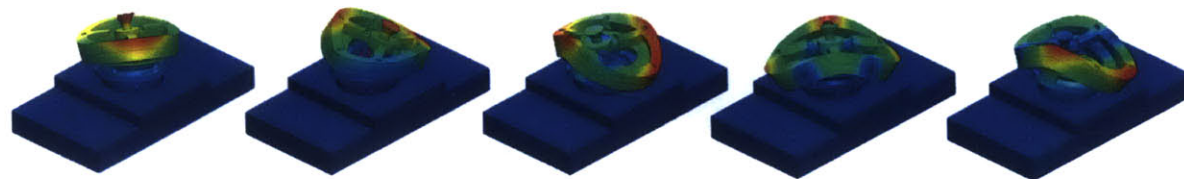
Mode:	1	2	3	4	5
FEA Peaks (Hz):	7368	7426	11274	11583	12876
Experimental Peaks (Hz):	8008		9892		12530

Table 4.1: This table shows both the results from dynamic FEA (including images representative of each resonant mode at the top) conducted in Solidworks® FEA [43] as well as experimental results obtained from the bandwidth validation jig. Resonant peaks measured via experiment are matched with their likely counterpart in simulation.
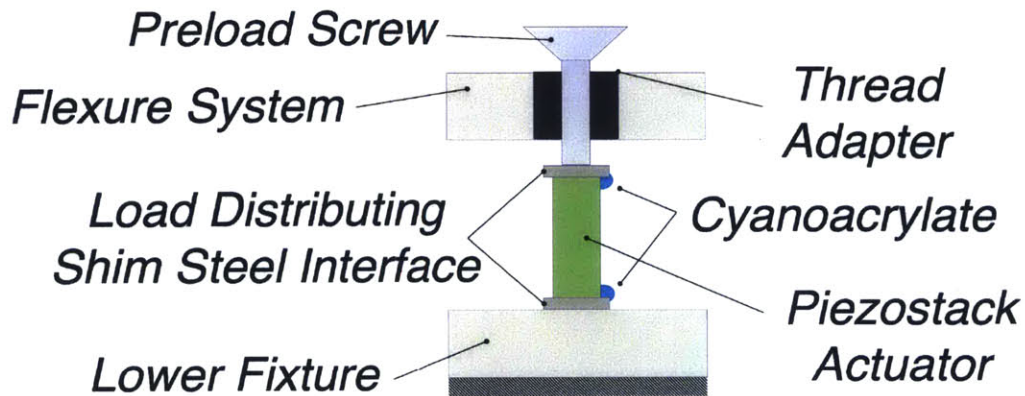
Figure 4-7: This graphic illustrates the key parts of the experimental setup for validating the bandwidth of the sensor. The actuator was a Thorlabs® piezostack actuator [52].

adapter [47], and without the force sensor or quick-release mechanism [adapted from data collected by Dr. Cathy Hogan]. The addition of the force sensor did not add any additional variation in the ejected volume. In fact, the variation decreased from the original device, likely thanks to the quick release adapter's improved mechanisms to constrain the piston [47].

4.5 Summary

With the device fully calibrated and performance validated on the relevant functional requirements, the device was ready to test on tissue to investigate the effect of contact force on injection quality. This work is presented in the next chapter.

Figure 4-8: These plots show the magnitude and phase for the swept sine analysis with the piezostack driving voltage as the input and a single bridge voltage measurement as the output. The upward slope of the magnitude plot is likely due to the resonance of the piezo stack actuator, which occurs at 69 kHz when the actuator is unloaded [52]. The phase indicates pure delay in the measurement, obscuring any useful insight.

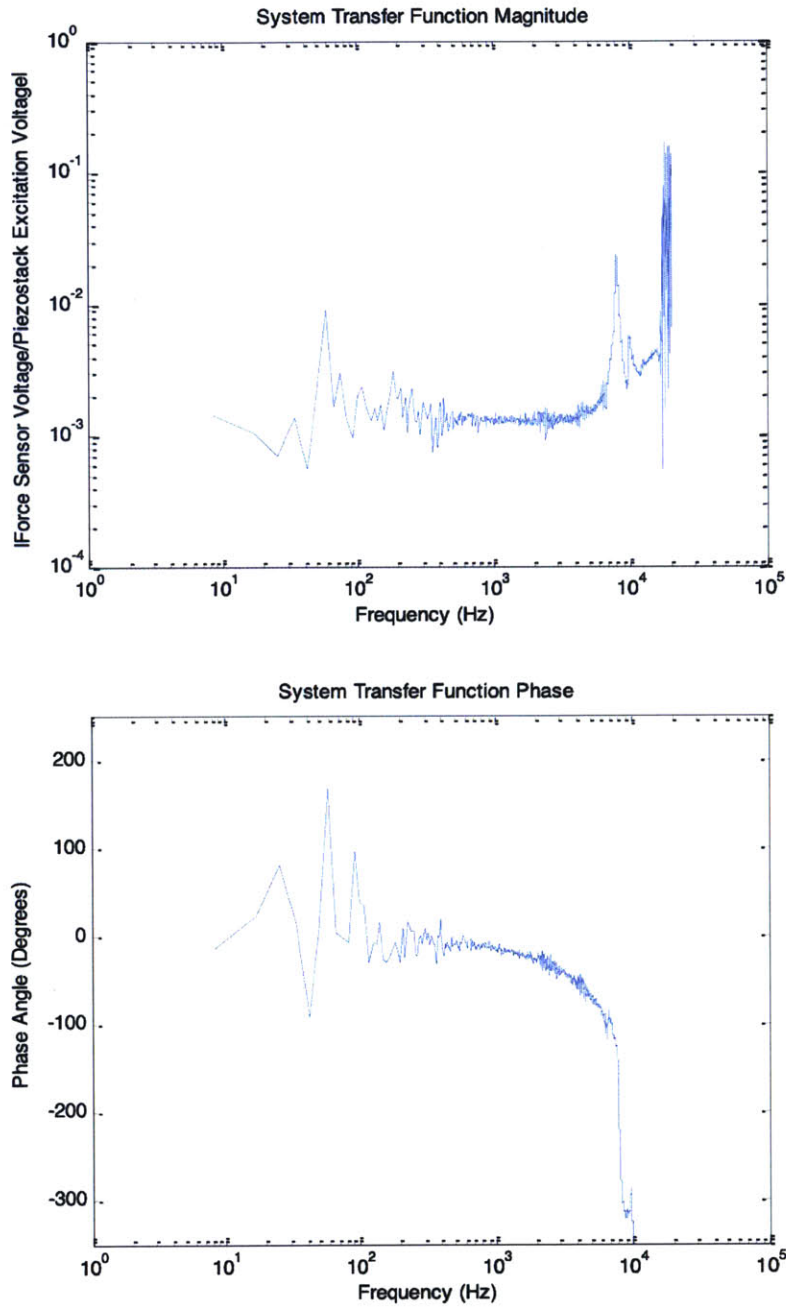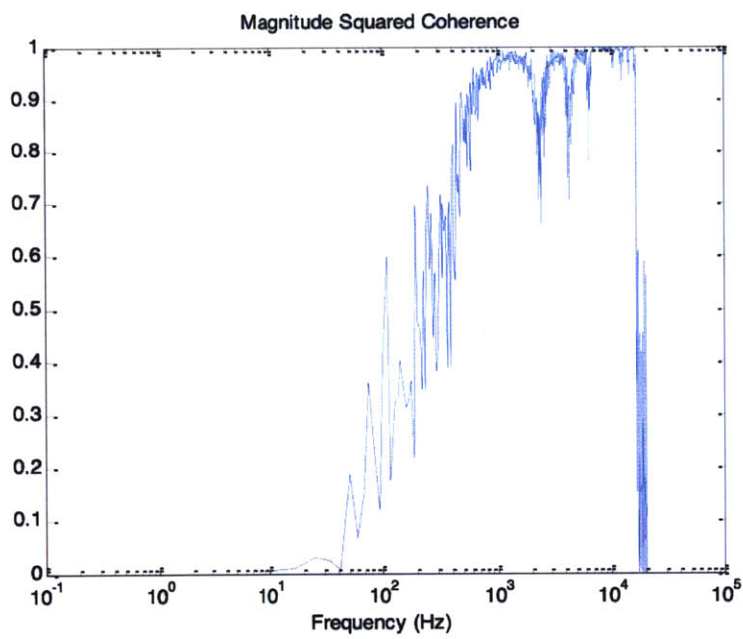Figure 4-9: This plot shows the coherence squared for the swept sine analysis with the piezostack driving voltage as the input and a single bridge voltage measurement as the output.

50 µL Ejection Validation

100 µL Ejection Validation

Key

- .... Desired Volume
- ▇ Original JI
- ▇ Modified JI with Quick-Release Adapter
- ▇ Modified JI with Quick-Release Adapter and Force Sensor
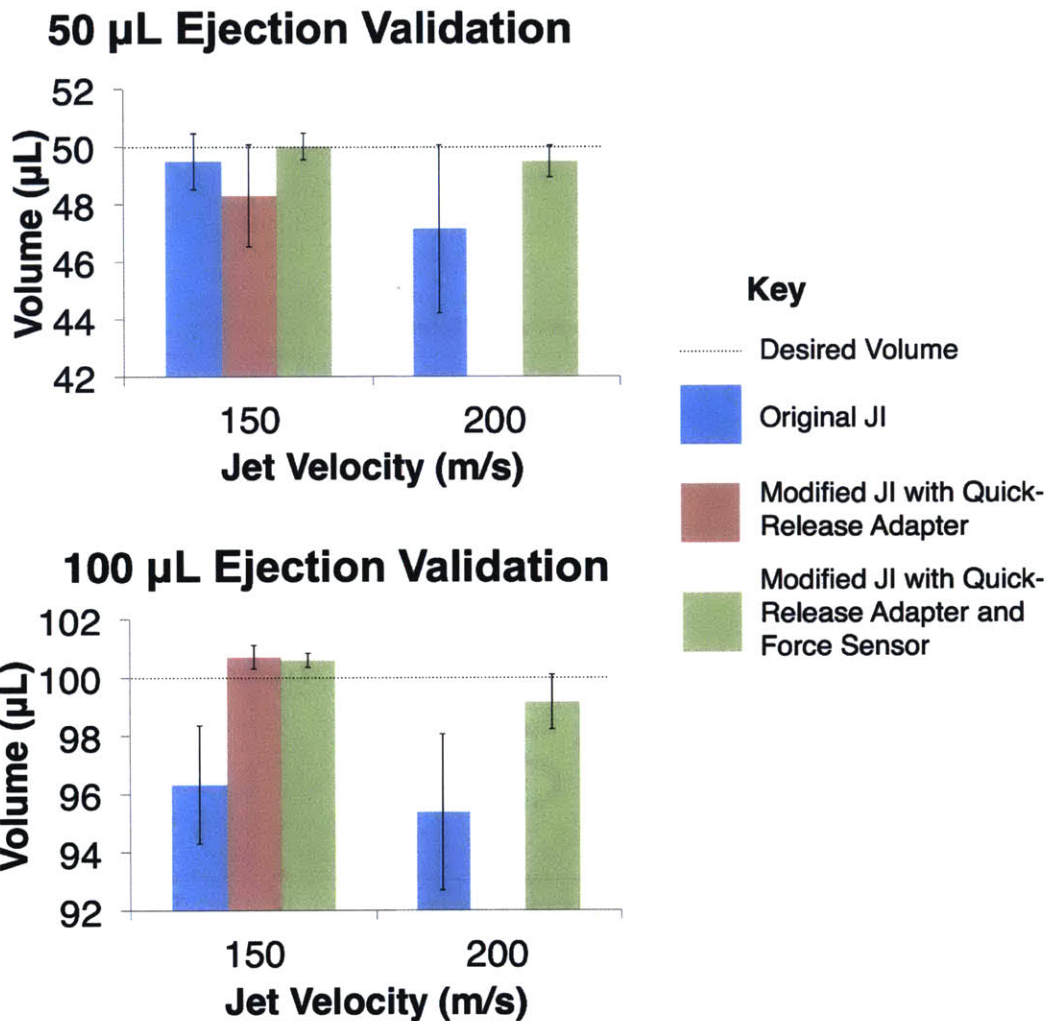
Figure 4-10: These plots compare the results from the ejection validation experiments conducted with the BioInstrumentation Lab's JI for various volumes and jet velocities. The black dashed line shows the target volume. Shown in blue are ejection results with the original JI, adapted from data collected by Dr. Cathy Hogan. Shown in red are results with quick-release adapter integrated [47]. The green shows the volume ejection performance with the quick release adapter and force sensor. The addition of the force sensor did not add any additional variation in the ejected volume. For the original JI tests, n = 10. For all other tests, n = 30. Note that data was not available for the Modified JI with Quick-Release Adapter at 200 m/s. Standard deviation is shown by the error bars.

Chapter 5

Tissue Testing

"Now be careful." *(McCoy)*

"Sound medical advice." *(Kirk)*

– After McCoy administers drug via hypospray, *Amok Time* 1967 [53]

With the device constructed, calibrated, and validated, injections could commence to investigate the effect of normal force on injection quality. First, injections into a skin analog gel were conducted. Next, injections were performed on intact *ex-vivo* porcine abdominal tissue. The following sections describe the experimental procedures and results.

5.1   Preliminary Skin Analog Injections

Preliminary tests were conducted with a 10% polyacrylamide gel by injecting a solution of 0.25% bromophenol blue and water with $v_{jet} = 200\,\text{m/s}$, $t_{jet} = 10\,\text{ms}$, $v_{follow} = 50\,\text{m/s}$, and $V = 100\,\mu\text{L}$. The contact force was varied through these injections. These gels are commonly used as skin analogs due to their transparency and skin-like stiffness and damping properties [54, 18]. It was found, as shown in Figure 5-1, that the injection dispersion patterns were qualitatively different when conducted at low (near 0 N) and high (approaching 4 N) normal forces. This may have been due to a number

Low Normal Force Indentation

High Normal Force Indentation

Low Normal Force Injection Dispersion

High Normal Force Injection Dispersion
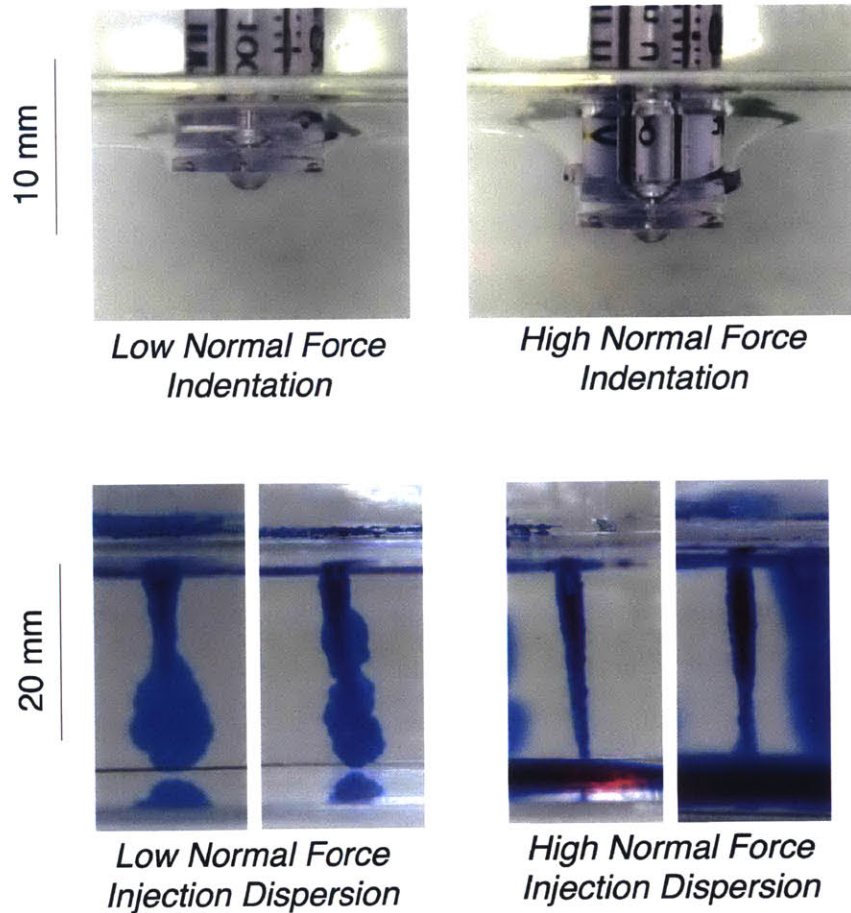
Figure 5-1: The top left and right images show how the nozzle and ampoule interacts with the skin analog at low (near $0\,\mathrm{N}$) and high (approaching $4\,\mathrm{N}$) normal forces respectively. The bottom two left and two right images show the resultant injection dispersion patterns, which were qualitatively different when conducted at these two force levels. Injection parameters were set to $v_{jet} = 200\,\mathrm{m/s}$, $t_{jet} = 10\,\mathrm{ms}$, $v_{follow} = 50\,\mathrm{m/s}$, and $V = 100\,\mathrm{\mu L}$.

of factors, but regardless it was evident that contact force impacts the quality of the injection, which was promising to see.

5.2 Experimental Setup and Procedure

For this set, injections were administered into pieces of abdominal porcine tissue, harvested from animals 6 months old or less, which included the epidermis, dermis, subcutaneous fat, and top muscle layers. The tissue was frozen immediately after harvesting at $-80\,^{\circ}$C. This tissue block, trimmed a width of $\sim$80 mm, length of $\sim$62 mm, and height of $\sim$25 mm, was placed atop a piece of absorbent paper towel on a glass plate and allowed to thaw prior to injections. This was the first and only time the tissue was allowed to thaw. After thawing was complete (2-3 hours at room temperature), the tissue was moved to a clear polymer tray and injections commenced. As with the ejection validation testing, three different ampoules (a, b, c) were fired, and each was exchanged after every injection sequentially (a,b,c,a,b,c. . .) to control for ampoule and piston variability and wear [47]. Normal force was also varied randomly between the injection sites to control for local tissue variation. For these injections, again $v_{jet} = 200$ m/s, $t_{jet} = 10$ ms, $v_{follow} = 50$ m/s, and $V = 100$ μL. Twelve total injections were completed per tissue block with tissue marking dye (to visualize injection path after sectioning) on a grid with a spacing of $\sim$20 mm. The tissue surface was dabbed with a towelette before injection, and any liquid remaining on the surface after injection was carefully absorbed after each injection. The volume remaining on the surface was determined using the mass method described in Section 4.4. An image of the tissue block after injections from a top view is shown in Figure 5-2.

After injections were completed, the tissue was cooled for approximately one-half hour in a $-20\,^{\circ}$C freezer to make the tissue firm for sectioning with a scalpel at the point of jet entry. This allowed for the penetration depth to be measured. Sectioned views are shown in Figure 5-3.

111
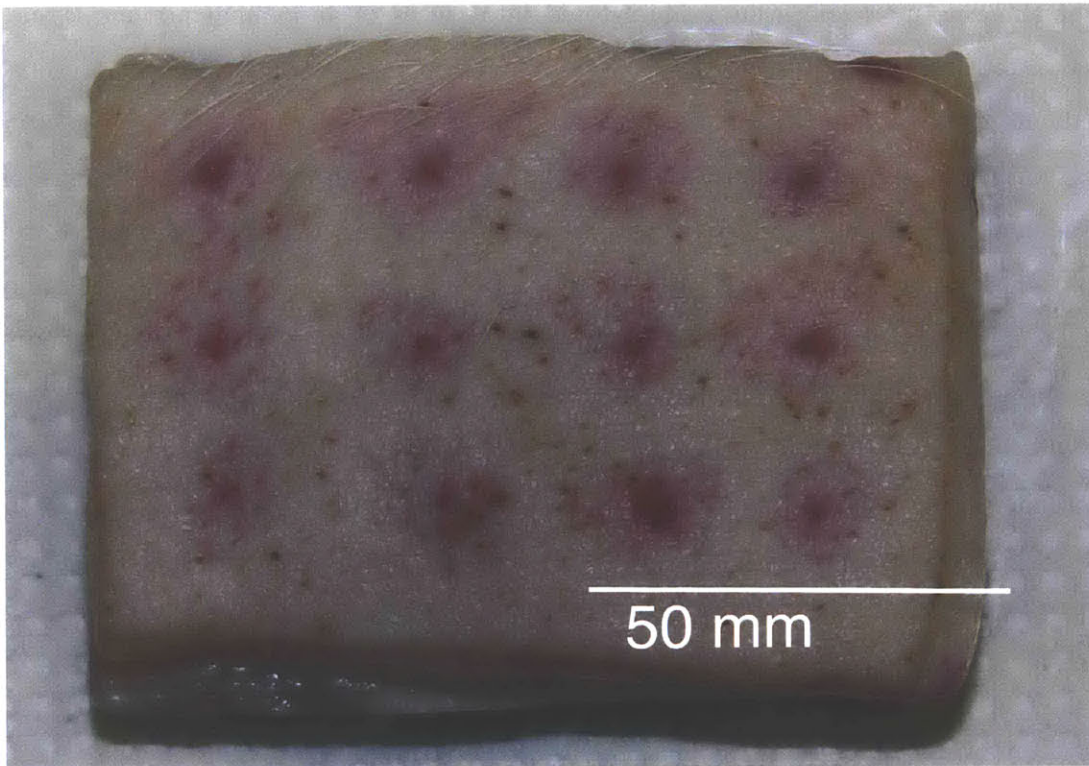
Figure 5-2: This photograph shows the top of the porcine tissue block after being injected with a constant volume of $100\,\mu L$ using a v_{jet} of $200\,m/s$, t_{jet} of $10\,ms$, and v_{follow} of $50\,m/s$. The injection locations are visible as red dots (resulting from the tissue marking dye used to color the water being injected) in a regular grid pattern.

→ *Increasing Contact Force* →

(0.38±0.19 N)

(0.77±0.20 N)　(0.85±0.19 N)

(1.00±0.26 N)　(3.43±0.18 N)

→ *Increasing Contact Force* →

(3.99±0.22 N)　(4.12±0.96 N)　(6.43±0.27 N)(7.15±0.18 N) (7.33±0.20 N)

50 mm
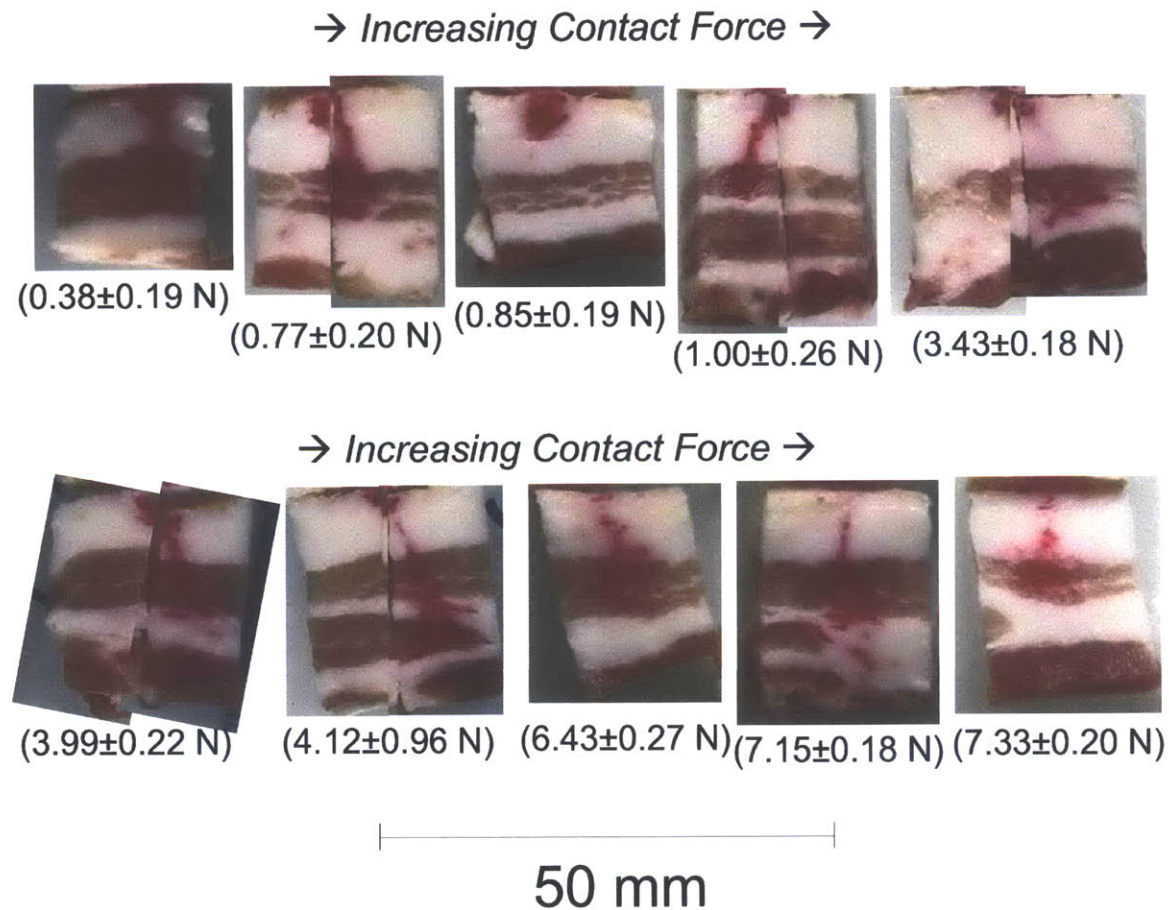
Figure 5-3: This photograph shows cross sections after injection. These views show a perpendicular plane to the tissue's surface, coincident with the point of jet entry. The average normal force applied by the nozzle on the tissue in the 10 ms before injection is indicated below each cross section. Some of the cross sections were halved again to reveal the maximum depth to which the fluid penetrated (if it did not penetrate exactly in the sectioned plane). Standard deviation is given for the contact force indicated below each cross section.

5.3 Results

A positive correlation existed between applied normal force and percent volume delivered in preliminary tests (n = 14). 100 µL injections occurring at low normal force (between 0 to 4 N) had an average percent volume delivered of 68.9 ± 12.7%. However, injections occurring at high normal force (between 4 to 8 N) showed a greater average percent volume delivery with smaller standard deviation at 89.1 ± 5.1%. In comparison, commercial insulin pens achieve mean injection volume percent delivery of 99±0.9% and better for 300 µL injections, which fall within ISO standards for medical pen injectors at ±3.3% for 300 µL injections [55]. While not yet at the percent volume delivery of insulin pen injectors, the percent volume delivery has improved by maintaining a higher contact force during injection with the force sensor.

There did not appear to be a correlation between injection depth and contact force. However, other unaccounted variations may be obscuring a relationship if one exists. In particular, manufacturing defects in the commercial nozzles used in this experiment have been shown to cause jet shape variation from one injection to the next through the same nozzle. Further tests where nozzle geometry (and therefore jet shape) is tightly controlled may shed light on a relationship between normal force and penetration depth.

5.4 Summary

These preliminary tissue injections indicated an elevated normal force improved percent volume delivery. While not as reliable as commercial needle injectors, volume delivered increased by over 25% on average and variation substantially decreased at higher contact forces. While a relationship between delivery depth and normal force was not observed in these tests, controlling for variability in the nozzle geometry (and jet shape produced) may allow for a relationship to be determined.
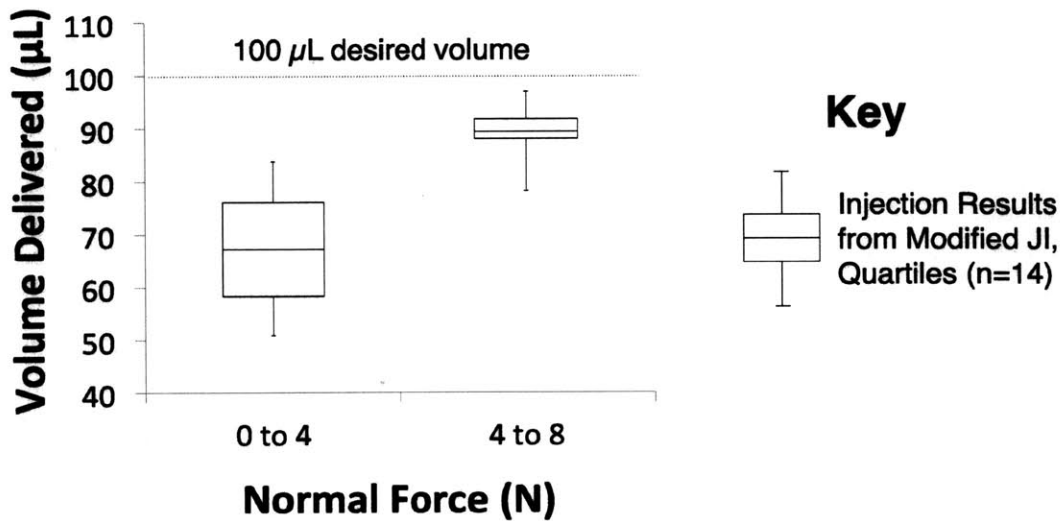
Figure 5-4: This graph shows the relationship between volume delivered and normal force for $100\,\mu\text{L}$ injections using a v_{jet} of $200\,\text{m/s}$, t_{jet} of $10\,\text{ms}$, and v_{follow} of $50\,\text{m/s}$. Injections occurring at high normal force showed a greater average percent volume delivered with a smaller standard deviation at $89.1\pm5.1\%$. Injections occurring at low normal force showed significantly less percent volume delivered and larger standard deviation at $68.9\pm12.7\%$ (p<0.01).
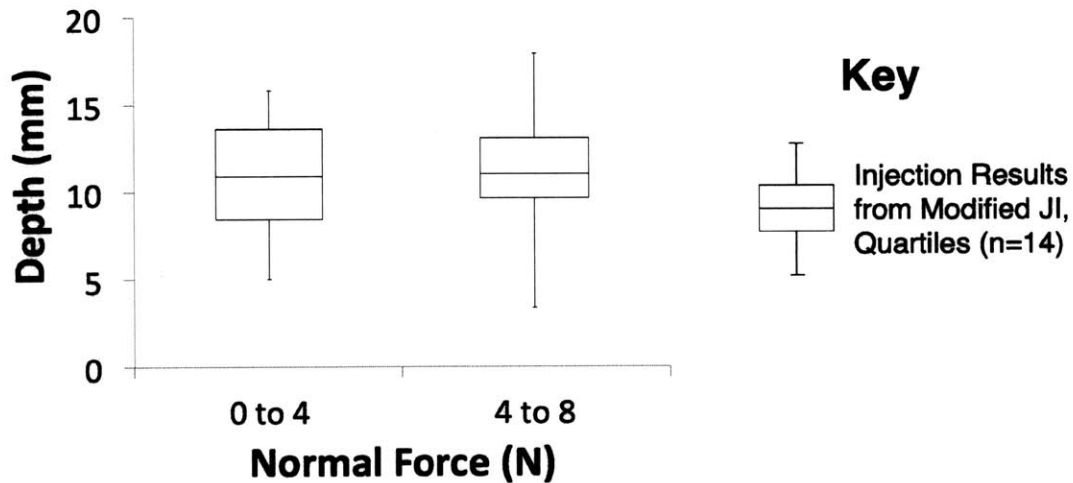

Figure 5-5: This graph shows the relationship between penetration depth and normal force for $100\,\mu\text{L}$ injections. Injections occurring at both high and low normal force showed similar average penetration depth and variability. v_{jet} was set to $200\,\text{m/s}$, t_{jet} was set to $10\,\text{ms}$, and v_{follow} was set to $50\,\text{m/s}$.

Chapter 6

Future Work

"The future cannot be predicted, but futures can be invented"

– Dennis Gabor, Nobel Physics laureate [56]

The revised sensor has been calibrated and validated and been used in some preliminary testing that indicated a relationship between normal force and percent volume delivered. From here, a number of paths exist moving forward. These include opportunities to improve the device and its performance, implement an interlock to decrease the risk of accidental firings, determine the fluid stream velocity in real-time, and to further explore the relationship between contact force and injection quality.

6.1   Design Improvements

While the design of the revised force sensor was an improvement over the initial prototype, a number of subsystems of the revised sensor were identified which, if properly redesigned, could improve usability, make the system more robust, and reduce cost and size. Three main systems on the current hardware were identified as distinct areas of improvement. The proposed changes to the systems are shown in Figure 6-1. These areas included the hardware of the force sensor (in red) currently employing an aluminum substrate flexure system with PCB strain relief, the DAQ system (in

117
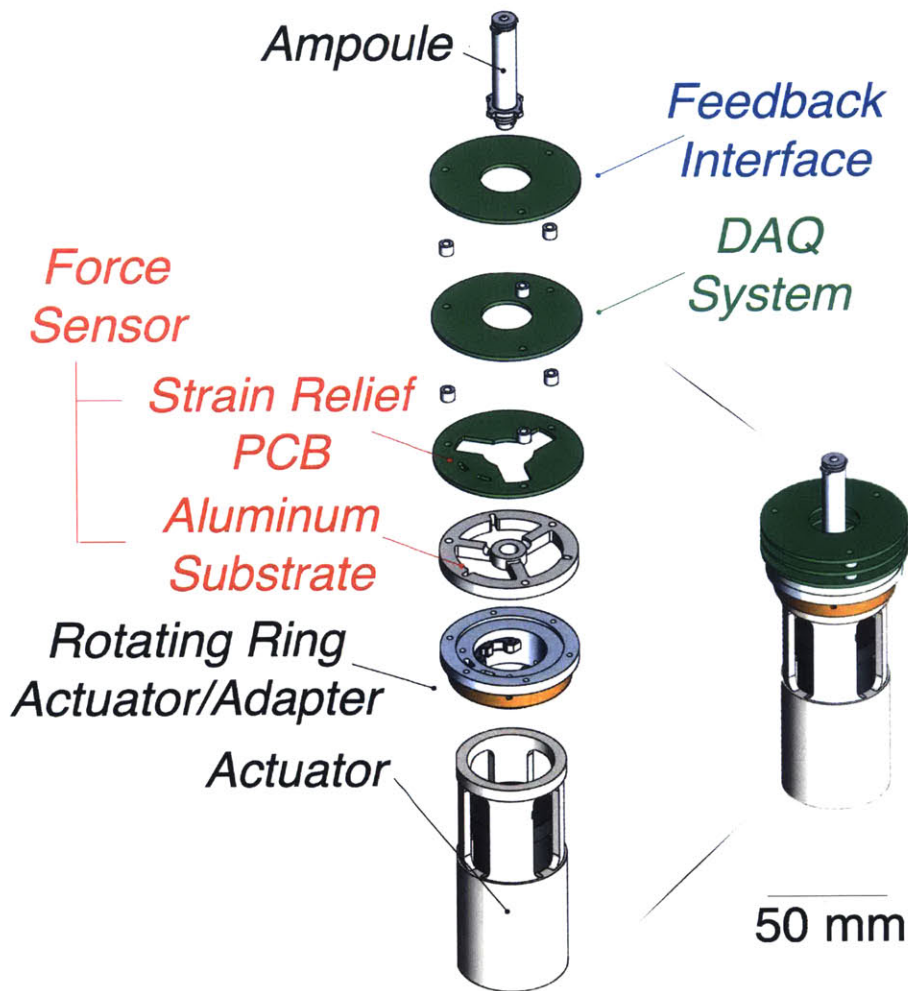
Figure 6-1: The three main systems are shown with proposed updates in this CAD model. The force sensor could stay with the aluminum substrate and PCB strain relief design (shown in this figure) or move into a full PCB design where the flexure system and strain relief were formed together in FR4 (not shown), eliminating much of the assembly cost associated with the current design. The DAQ could be implemented on another PCB layer using chip-based data acquisition systems within the device. Lastly, the feedback interface could be integrated directly into the device and present information to the user much closer to the site of injection.

Figure 6-2: This sketch shows a preliminary integrated PCB force sensor concept with ampoule mounted.

green) utilizing an NI cRIO 9024 with 9237 module [28] on the revised sensor integrated with the Human JI, and the feedback interface (in blue) currently deployed in LabVIEW® and displayed on a monitor.
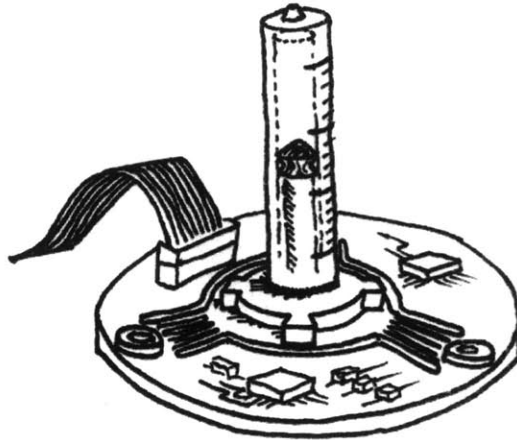
6.1.1 Force Sensor

Starting with improvements to the hardware of the force sensor, a major deficit of the current flexural system layout is the lengthy assembly time and lack of robustness in the electrical connections (which, for the revised sensor design, are shown in Figure 3-16). The pads on the foil strain gauges are very small and delicate, making it difficult to solder and prone to sustaining damage. The reason that these electrical connections must be made in this manner is due to the fact that the design is built around an aluminum flexure system. Signals must be routed first to the strain relief PCB and then routed out to the DAQ system.

One approach to shortening assembly time and improving robustness would be to form the flexure system and strain relief in a single PCB. While the properties of FR4, a candidate composite substrate, are anisotropic, modeling and characterizing may still be possible in an advanced FEA environment.
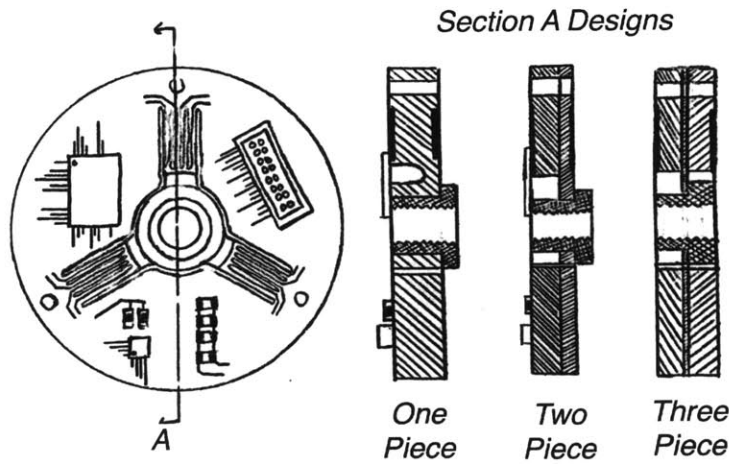
119

Figure 6-3: These sketches show a variety of methods by which the PCB flexure could be formed using one, two, or three layers to achieve the Quasi-Free boundary feature. Adapted from [57].

Another improvement to the sensor would be addition of provisions to correct for "phantom" normal force. "Phantom" normal force occurs when the assumptions used to build the sensor model are broken (for example, if torsion is not completely rejected) and the sensor incorrectly resolves both a lateral force and a false "phantom" normal force in the presence of an applied purely lateral force. This is shown in Figure 6-4. While this could have been an issue, fortunately the way the user is instructed to apply the device helps reduce induced inaccuracies. When the user is instructed to minimize lateral forces, the phantom force will also decrease. Once lateral forces have been minimized, the user will operate very near the normal force axis F_{normal} (as shown in Figure 6-4), where the inclination of the lateral force plane has minimal effect on the resolved normal force measurement accuracy. Additionally, very preliminary experimentation has revealed that the phantom normal force appears on the order of ~0.05 N per 1 N of lateral force application for the revised sensor design.

While the way the device is used helps minimize the effect of "phantom" normal force and its magnitude is relatively small compared to our functional requirement for resolution of ±0.5 N even at moderate lateral forces, it would be beneficial to correct for this error. Whereas angle parameters a and b correct for skew in the lateral plane, additional linear parameters could be added to correct for the "phantom" normal
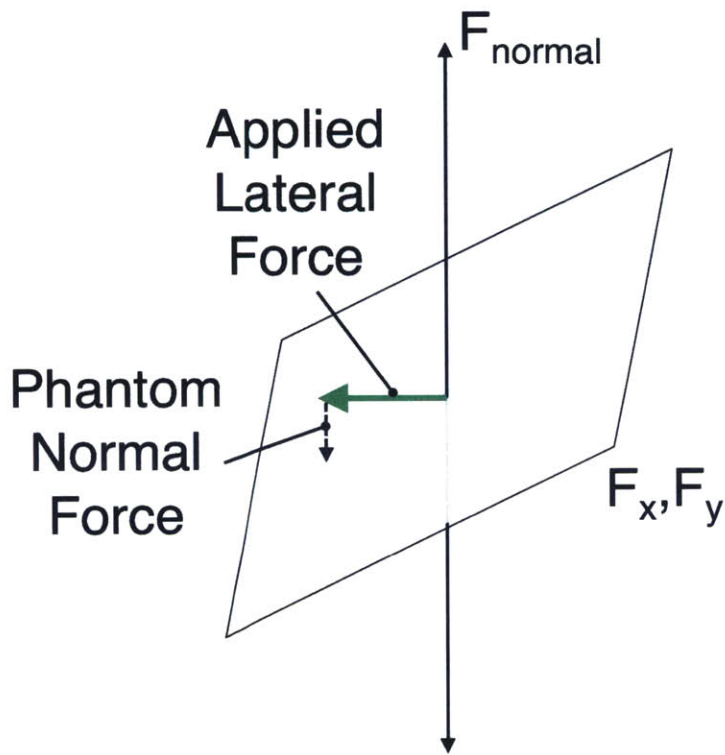
Figure 6-4: With an applied lateral force in green, a "phantom" normal force could also be resolved due to a mismatch between actual behavior and assumed behavior on which the model was built. However, when the user minimizes lateral forces, the phantom force will also decrease.

force. Higher order corrections with more parameters could be made to correct for more complicated distortions affecting the "phantom" normal force. The improvement in accuracy of measured contact forces would be beneficial in further injection studies (as detailed in Section 6.4).

6.1.2 DAQ

While the current DAQ system utilizing an NI cRIO 9024 in the Human JI with module 9237 [28] works quite well, its cost and size make it appropriate only for a research device and not a medical product. In particular, Cypress® Programmable System on a Chip (PSoC) [58] are one chip based data acquisition systems that has been identified to allow both for monitoring forces before and during injection in a
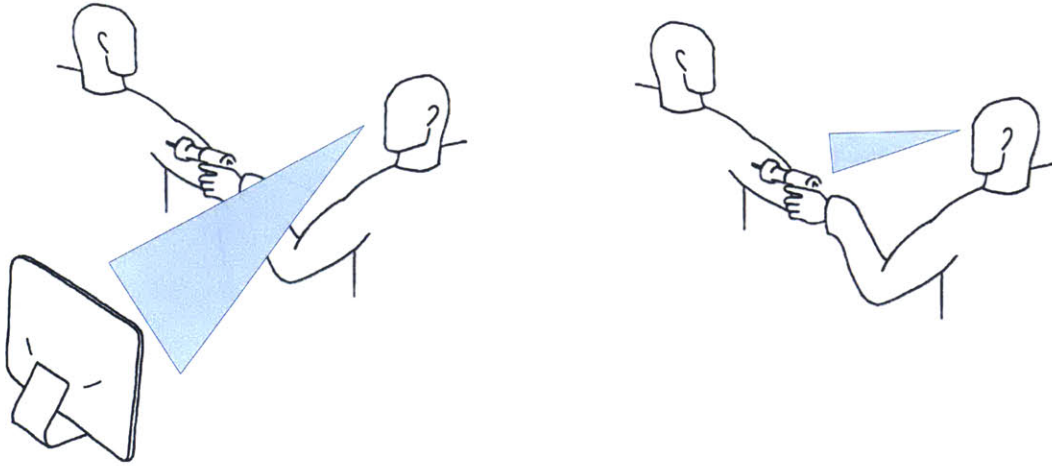
Figure 6-5: (*Left*) Revised sensor display through external monitor. The caregiver's attention is on the monitor rather than on the injection site. (*Right*) Proposed force display near injection site. Here, the caregivers attention could be on the injection site and the force level simultaneously.

small, inexpensive package.

6.1.3   Force Display

The current method by which forces are displayed is through an external monitor, as shown in the left in Figure 6-5. This setup is very different from current hypodermic injections, where the caregivers attention is fully on the injection site at all times. Caregivers may feel uncomfortable with this new paradigm and would likely be reluctant to use the JI device. As such, making the experience of the caregiver as similar to the current standard of care is critical.

A proposal to accomplish this is shown illustrated in Figure 6-5 on the right. Instead of relying on an external monitor, the contact force indicator would be displayed close to the injection site. In this way, the caregivers attention could be on the injection site and the force level simultaneously.

Experimentation is currently underway to determine an ideal display paradigm that is intuitive and can repeatably guide the user to the appropriate contact force.

6.2 Interlock

Implementing a force-sensing interlock so that the device could not fire (even if the trigger was pressed) without applying a contact force in a pre-specified range and duration would decrease the risk of accidental firings. Especially if this device was to be deployed as a treatment self administered by the patient, implementation of safety features such as this would be important.

6.3 Real-time Monitoring of Velocity

Given that the force sensor is actively measuring both before and during an injection, it is possible to model the pressure within the ampoule and obtain an estimate of the exit velocity of the fluid. This has been of interest for some time in the BioInstrumentation Lab. Given the force sensor's completed integration into the device, the sensor may play a role in future studies related to quantifying and controlling velocity of the fluid stream.

First, Figure 6-6 shows the forces exerted on the ampoule during firing. If it is assumed that there is no acceleration of the ampoule, then $\sum F = 0$. This results in the Equation 6.1 below where P_{fluid} is the pressure of the fluid exerted over area A, F_{normal} is the normal contact force exerted by the skin on the nozzle, F_{fr} is a frictional force exerted by the prison sliding through the ampoule, F_{shear} is the shear force of the high velocity fluid on the walls of the nozzle, and $F_{measured}$ is the force exerted and measured by the force sensor,

$$P_{fluid} = \frac{F_{normal} - F_{measured} - F_{fr} - F_{shear}}{A}. \tag{6.1}$$

As a very first-order estimate, it is possible to assume that Bernoulli's equation holds (although the viscous losses will be quite substantial at high jet stream velocities), the velocity of the piston is small in comparison to the jet and the change in height is negligible. As such, it is possible to determine the velocity of the jet, V_{jet}, given the fluid pressure P_{fluid} and density ρ_{fluid}, given by Equation 6.2,
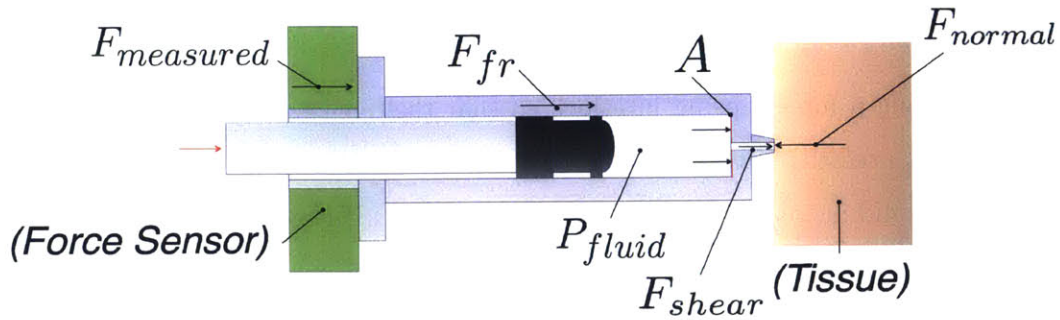
Figure 6-6: This illustration shows the forces applied to the ampoule when the device fires (presuming no lateral forces are applied).

$$V_{jet} = \sqrt{\frac{2}{\rho_{fluid}} P_{fluid}}.$$ (6.2)

With these relationships in hand, analysis of the pre-recorded injection force data was conducted. Figure 6-7 shows the results and compares potentiometer and force sensor derived velocities versus prescribed velocity. It is interesting to note how the potentiometer derived velocity was very oscillatory as compared to the force sensor derived velocity, which matches the prescribed velocity much more closely (with a slight offset, which may be due to F_{shear} being set to zero for this preliminary plot). This lack of oscillation may be due to the fact that the force sensor is closer structurally to the ampoule, since the force sensor interfaces directly with the ampoule which has the nozzle integrated at its tip. This compares to the potentiometer where the linear potentiometer pin first attaches to the bobbin, then to the quick release adapter, then to the polycarbonate piston shaft, then the piston tip before interacting with the fluid in the ampoule. With an increased number of parts and joints, the possibility of oscillations between components also increases.

While this analysis was conducted after the injection took place, it would be possible to calculate the velocity through the force sensor using the method described in real-time. As such, this measurement may have a place in the closed-loop control system for the device. Given contact forces are likely no greater than $\sim 10\,\mathrm{N}$ and forces exerted by the actuator reach $200\,\mathrm{N}$, the error induced by a varying contact force through the injection would have, at most, a small effect on the velocity measurement.
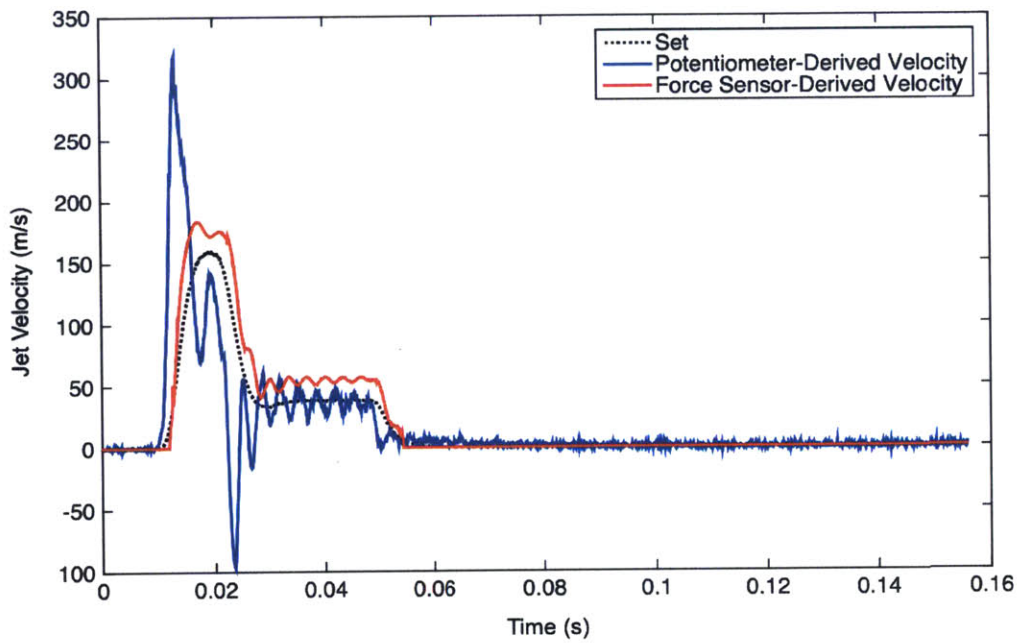
124

Figure 6-7: This plot shows both potentiometer and force sensor derived velocities versus prescribed velocity. Note that F_{shear} has been assumed to be zero in this preliminary model, which may be able to account for the overestimate in force sensor-derived velocity. Further investigation is needed.

6.4   Further Animal Tissue Testing

As mentioned in Chapter 5, the relationship between contact force and penetration depth was not apparent in the preliminary tests conducted. It was hypothesized that variability in jet shape from one firing to the next was hiding the relationship if one existed. Improving the reliability of the jet injector nozzle geometry to produce consistent jet shapes might allow for a relationship between contact force and penetration depth to be observed. Work in this area has already commenced and will appear an accepted manuscript awaiting publication titled "The Effect of Jet Shape on Jet Injection" by Park *et al.* from the BioInstrumetation Lab.

While the preliminary tests on animal tissue sought to minimize the lateral force applied to the tissue, the maximum lateral force where adverse effects occur would be important to quantify. With this information, the device could be programmed to guide the user to adhere to pre-determined loading conditions.

6.5   Human Trials

While *ex-vivo* porcine skin tissue has similar properties and structure to human skin, it certainly has its deficits. First, the tissue is stored frozen and thawed before injection, which potentially may damage the structural integrity of the tissue. Additionally, many qualities present in a living tissue (skin pretension, muscle contraction, etc.), are not easily reproduced in the tissue block. Human testing may indicate a higher or lower desired normal force for attaining a certain percent volume delivered and these percent volume delivery studies could be conducted on a living person. These studies are currently ongoing in the BioInstrumentation Lab. However, to detect the depth to which drug penetrates, non-invasive methods by which the penetration depth could be measured would need to be developed.

The effect of contact force (both normal and lateral) on injection quality is also intimately tied with the outside geometry of the nozzle in contact with the skin. Both the sealing characteristics of the geometry as well as pretensioning will likely effect

the injection. While a force level of approximately 4 N did appear appropriate on the *ex-vivo* porcine tissue with Injex nozzles [11], different loading conditions may be appropriate for modified interior and/or exterior nozzle geometry on human tissue. Gaining a better understanding of how increased contact force improves percent volume delivery with particular nozzle outer geometries would be interesting.

6.6 Summary

This chapter has outlined a number of research thrusts that could be completed with this force sensor. The results of these pursuits would lead to a more robust, cheaper, smaller, user friendly and safer system. With these improvements to the sensor, experiments could be conducted to more fully understand the factors influencing injection quality with respect to contact force.

Chapter 7

Conclusion

"Now this is not the end. It is not even the beginning of the end. But it is, perhaps, the end of the beginning. "

– Winston Churchill, in a speech at the Lord Mayor's Day luncheon, London

November 10, 1942 [59]

Through this thesis, the development and design, fabrication, calibration and validation, preliminary tissue testing and future work for a jet injector contact force sensor has been presented. These efforts were driven by the desire to achieve better quantification and control of the contact force between the nozzle and tissue over methods employed with commercial JIs. The design work resulted in novel flexure design [57] with good overall performance characteristics with respect to the functional requirements. Careful calibration resulted in very good resolved force measurements. Thorough validation procedures confirmed the performance specifications. Preliminary results with tissue indicated that an elevated contact force improves percent volume delivery which has important clinical and cost implications. The future goals following this thesis are to continue development of the next generation of the sensor system and conduct future biological testing following the work outlined in Chapter 6. This work will improve the understanding of how contact force influences the quality of jet injections.

129

Bibliography

[1] LL Marshall. Hypodermic injector, June 1943. US2322244 A, http://www.google.com/patents/US2322244.

[2] A Tinniswood. *His Invention So Fertile : A Life of Christopher Wren.* Oxford University Press, USA, November 2001.

[3] MR Prausnitz, S Mitragotri, and R Langer. Current status and future potential of transdermal drug delivery. *Nature Reviews Drug Discovery*, 3(2):115–124, February 2004.

[4] NusingTimes.net. The Administration of Medicines, November 2007. http://www.nursingtimes.net/nursing-practice/specialisms/prescribing/the-administration-of-medicines/288560.article.

[5] BBC. BBC - History - Sir Christopher Wren, 2014. http://www.bbc.co.uk/history/historic_figures/wren_christopher.shtml.

[6] S Wright, M Yelland, K Heathcote, S Ng, and G Wright. Fear of needles - Nature and prevalence in general practice. *AFP*, 38(3):172–176, March 2009.

[7] ISIPS. Needlesticks, 2015. http://www.isips.org/page/needlesticks.

[8] S Mitragotri. Current status and future prospects of needle-free liquid jet injectors. *Nature Reviews. Drug Discovery*, 5(7):543–548, July 2006.

[9] PN Hoffman, RA Abuknesha, NJ Andrews, D Samuel, and JS Lloyd. A model to assess the infection potential of jet injectors used in mass immunisation. *Vaccine*, 19(28âĂŞ29):4020–4027, July 2001.

[10] WHO. Solutions - Choosing Technologies for Safe Injections, September 2012. https://web.archive.org/web/20120921104456/https://apps.who.int/vaccines-access/injection/injection_safety/safe_injections_choosing_technologies.htm.

[11] Injex. Injex Needle Free Injector, 2013. http://injexuk.com/index.html.

[12] Activa Brand Products Inc. Zoe Needle-free Insulin Jet, 2010. http://www.zoepetjet.com/home.htm.

[13] Endo Pharmaceuticals Inc. Sumavel DosePro, 2014. http://www.sumaveldosepro.com/.

[14] National Medical Products, Inc. J-Tip Needle-Free Injection System, 2015. http://www.jtip.com/.

[15] Crossject needle-free injection systems. Crossject, 2013. http://www.crossject.com/.

[16] NC Hogan, AJ Taberner, LA Jones, and IW Hunter. Needle-free delivery of macromolecules through the skin using controllable jet injectors. *Expert Opinion on Drug Delivery*, pages 1–12, May 2015.

[17] T Burnham. Get Set: A Jet To Replace Needles For Injections, May 2012. http://www.npr.org/sections/health-shots/2012/05/25/153697885/mit-builds-a-needle-free-drug-injector.

[18] AJ Taberner, NC Hogan, and IW Hunter. Needle-free jet injection using real-time controlled linear Lorentz-force actuators. *Medical Engineering & Physics*, 34(9):1228–1235, November 2012.

[19] Bioject. Bioject ZetaJet, 2012. http://www.bioject.com/products/zetajet.

[20] JC Stachowiak, MG von Muhlen, TH Li, L Jalilian, SH Parekh, and DA Fletcher. Piezoelectric control of needle-free transdermal drug delivery. *Journal of Controlled Release*, 124(1åÅ§2):88–97, December 2007.

[21] Drugs.com. Giving An Insulin Injection - Care Guide, 2015. http://www.drugs.com/cg/giving-an-insulin-injection.html.

[22] BD Hemond, A Taberner, NC Hogan, B Crane, and IW Hunter. Development and Performance of a Controllable Autoloading Needle-Free Jet Injector. *Journal of medical devices*, 5(1), 2011.

[23] JE White, JH Chang, NC Hogan, and IW Hunter. Development of a lorentz-force actuated intravitreal jet injector. In *2012 Annual International Conference of the IEEE Engineering in Medicine and Biology Society (EMBC)*, pages 984–987, August 2012.

[24] SJ Gilbert. Method for making a needle-free jet injection drug delivery device, November 2013. U.S. Classification 604/70; International Classification A61M5/30; Cooperative Classification A61M2205/59, A61M2205/587, A61M5/2053, A61M5/19, A61M5/2046, A61M5/31511, A61M5/30, A61M5/3007, A61M2210/0618, A61M2210/0612.

[25] CDC. VFC | Current CDC Vaccine Price List | CDC, July 2015. http://www.cdc.gov/vaccines/programs/vfc/awardees/vaccine-management/price-list/.

[26] UNC Eshelman School of Pharmacy. The Pharmaceutics and Compounding Laboratory, 2015. http://pharmlabs.unc.edu/labs/parenterals/subcutaneous.htm.

[27] Zogenix, Inc. Technology - Zogenix, 2014.
http://www.zogenix.com/content/technology/dosepro.htm.

[28] National Instruments Corporation. NI, 2015. http://www.ni.com/.

[29] BR Rich. Clarence Leonard (Kelly) Johnson, 1910 to 1990, A Biographical
Memoir, 1995. http://www.nasonline.org/publications/biographical-
memoirs/memoir-pdfs/johnson-clarence.pdf.

[30] A Slocum. FUNdaMENTALS of Design, October 2013.
http://web.mit.edu/2.75/fundamentals/FUNdaMENTALS.html.

[31] Bomazi. Interlink Electronics FSR 402 Force-Sensing Resistor., August 2012.

[32] OMEGA Engineering inc. Precision Strain Gages Dual-Grid for Bending
Strains, 2015. http://www.omega.com/pptst/SGD_DUAL-GRID.html.

[33] Sparkfun.com. Piezo Element SEN-10293, 2015.
https://www.sparkfun.com/products/10293.

[34] Weighing and Force Instrument Panel. Guide to the Measurement of Force,
2013. www.npl.co.uk/content/ConMediaFile/7514.

[35] Sensitronics LLC. Sensitronics Website, 2015. http://www.sensitronics.com/.

[36] EW Weisstein. Fourier Transform Spectrometer, 2007.
http://scienceworld.wolfram.com/physics/FourierTransformSpectrometer.html.

[37] National Instruments. Strain Gauge Configuration Types, October 2006.
http://www.ni.com/white-paper/4172/en/.

[38] MakeItFrom.com. 7075-T6 Aluminum Material Properties, 2015.
http://www.makeitfrom.com/material-properties/7075-T6-Aluminum/.

[39] AF Grandt. *Fundamentals of Structural Integrity: Damage Tolerant Design
and Nondestructive Evaluation.* John Wiley & Sons, November 2003.

[40] C Caprani. Structural Analysis III The Moment Area Method, MohrâĂŹs
Theorems, 2008.
http://www.colincaprani.com/files/notes/SAIII/Mohrs%20Theorems.pdf.

[41] The MathWorks, Inc. MATLAB, 2015.
http://www.mathworks.com/products/matlab/?refresh=true.

[42] Siemens Product Lifecycle Management Software Inc. FEA / Finite Element
Analysis: Siemens PLM Software, 2015.
http://www.plm.automation.siemens.com/en_us/plm/fea.shtml.

[43] Dassault Systemes. Solidworks, 2015. http://www.solidworks.com/.

[44] Henkel Corporation. Loctite 498 Super Bonder Instant Adhesive, 2015.
http://www.henkelna.com/product-search-
1554.htm?nodeid=8797892149249&msdsLanguage=EN_US&selectedTab=technical.

[45] K Hoffmann. Practical hints for the installation of strain gauges, 1996.
http://www.hbm.com/en/menu/tips-tricks/experimental-stress-
analysis/practical-hints-for-the-installation-of-strain-gages/.

[46] Haas Automation Inc. HAAS, 2015. https://www.haascnc.com/home.asp.

[47] MT Nawrot. Design of a robust, intuitive piston interface for a needle free
injection system, 2014. http://hdl.handle.net/1721.1/93008.

[48] Digikey. 732-3534-ND CABLE FFC 1mm TYPE 2 10p 200mm, 2015.
http://www.digikey.com/product-detail/en/686710200001/732-3534-
ND/2811256.

[49] TEMCo Industrial Power Supply. 28 AWG Copper Magnet Wire MW0064, 2015.
http://www.temcoindustrialpower.com/products/Magnet_Wire/MW0064.html.

[50] MakerBot Industries, LLC. MakerBot, 2015. http://www.makerbot.com/.

[51] Ensinger-Hyde. Delrin (Aceltal Homopolymer) Data Sheet, 2015.
www.sdplastics.com/delrin/delrin[1].pdf.

[52] Thor Labs. AE0505d16f - Piezoelectric Actuator, 2015.
https://www.thorlabs.com/thorproduct.cfm?partnumber=AE0505D16F.

[53] J Pevney. Star Trek Script, September 1967.
http://www.chakoteya.net/StarTrek/34.htm.

[54] J Schramm-Baxter, J Katrencik, and S Mitragotri. Jet injection into
polyacrylamide gels: investigation of jet injection mechanics. *Journal of
Biomechanics*, 37(8):1181–1188, August 2004.

[55] M Krzywon, T van der Burg, U Fuhr, M Schubert-Zsilavecz, and
M Abdel-Tawab. Study on the dosing accuracy of commonly used disposable
insulin pens. *Diabetes Technology & Therapeutics*, 14(9):804–809, September
2012.

[56] QI. September 2012 Quote Investigator Archives, 2012.
http://quoteinvestigator.com/2012/09/#note-4515-1.

[57] NP Demas, IW Hunter, BD Hemond, and MT Nawrot. Multi-Directional
Low-Displacement Force Sensor. 62/064,543.

[58] Cypress Semiconductor Corporation. Programmable System-on-Chip (PSoC),
2015. http://www.cypress.com/products/programmable-system-chip-psoc.

[59] W Churchill. The Bright Gleam of Victory, 1942.
http://www.winstonchurchill.org/resources/speeches/1941-1945-war-
leader/the-end-of-the-beginning.